Università degli Studi di Modena e Reggio Emilia

DIPARTIMENTO DI INGEGNERIA "ENZO FERRARI"
Corso di Dottorato di Ricerca in Ingegneria Industriale e del Territorio "Enzo Ferrari"
XXXIV Ciclo

Tesi di Dottorato in Fisica Tecnica Industriale

Direct numerical simulation of turbulence: the flow past an irregular grid and the aerodynamics of a rectangular cylinder

Roberto Corsini

Relatore:
Chiar.mo Prof. Enrico Stalio

Coordinatore del Corso:
Chiar.mo Prof. Alberto Muscio

Anno Accademico 2020–2021

Ai miei genitori,
Nadia e Adriano

Acknowledgements

I would like to express my gratitude to my research supervisor, prof. Enrico Stalio, for his dedicated support and valuable guidance throughout my doctoral studies. His constructive feedback and resolute suggestions were crucial in making this work as flawless as possible.

I am also grateful to dr. Andrea Cimarelli, Università degli Studi di Modena e Reggio Emilia, for his unremitting contribution to our work on the aerodynamics of a rectangular cylinder, and for numerous useful discussions on this and other topics.

All the co-authors of the papers published in the framework of this thesis are warmly acknowledged. I take the opportunity for addressing special thanks to dr. Andrea Fregni, Università degli Studi di Modena e Reggio Emilia, for his fruitful collaboration to the work on the turbulence past an open-cell metal foam.

The computing resources to perform the simulations were provided by PRACE and GENCI on Joliot-Curie at the Trés Grand Centre de Calcul (TGCC) of CEA, France, under the PRACE project number 2020225348 and the DARI allocation A0092A12037. Further resources were granted by CINECA on Marconi and Galileo systems, based in Italy, under the ISCRA C initiative. Their support is gratefully acknowledged. The promptness and expertise of the technical support services offered by TGCC and CINECA have also been appreciated in the course of the numerical activity.

I wish to thank my colleagues for the professional conversations as well as the cherished time spent together in and out of the office.

My sincere thanks go to my parents for their endless support and confidence throughout my studies, my sister Laura for the excellent example she sets, my grandmother Rosa and my aunt Ave for the thoughtfulness and sustenance provided. Thanks to the rest of my family for all the encouragement given so far.

A heartfelt thanks to Francesca for the closeness and patience shown over these last years.

Finally, many thanks to my friends who always offered a sympathetic ear and provided joyful distractions to rest my mind outside of my research.

Abstract

Most flows observed in nature and engineering applications are turbulent. Turbulence increases mixing and transfer of mass, momentum, and internal energy (heat). In the study of turbulent flows, the direct numerical simulation (DNS) approach is recognised to be unrivalled in terms of the accuracy and the completeness of the description provided. However, the steeply increasing computational cost and the huge amount of information resulting from the local and instantaneous description, make the DNS method unaffordable for routine engineering studies. In the industrial framework it is more convenient to pursue a modelling approach based on the statistical representation of turbulent flow fields. On the other hand, the elaboration of simple yet accurate turbulence theories and models may only rely on highly detailed data with small spatial and temporal discretization errors. The present work aims at providing high-fidelity results of relevant turbulent flows in the research field. Two turbulent flows are tackled by means of high-order accurate direct numerical simulation and the physical processes involved are investigated.

Firstly, the turbulence generated by a uniform stream passing through an open-cell metal foam layer is analysed. This flow configuration is presented as a novel realization of grid turbulence where, in place of a regular grid, there is a porous matrix which is locally irregular but statistically isotropic. The metal foam geometry is produced synthetically with porosity of $\varepsilon = 0.92$ and streamwise thickness of five times the mean pore diameter d_p. The computation is performed using the high-order finite-difference DNS code *Incompact3d* at a Reynolds number based on the pore diameter of $Re_{d_p} = 4000$. Closer to the foam than two pore diameters, the pressure and turbulent transport of turbulent kinetic energy are non-negligible. At larger distances from the porous layer, the canonical grid turbulence situation is recovered, where dissipation is balanced by the mean advection of turbulent kinetic energy. In this region, the decay of the main turbulent quantities and characteristic length scales is described by power-law functions. The corresponding exponents are calculated and compared with classical theories of homogeneous and isotropic turbulence.

The second case investigated is the aerodynamics of a rectangular cylinder with chord-to-thickness ratio $c/D = 5$. This flow configuration is representative of the aerodynamics of a wide range of bluff bodies of interest in civil engineering, and recently has been set as a benchmark for the study of separating and reattaching external flows. Three DNSs of the flow around the rectangular cylinder are carried out at different values of the Reynolds number

based on the cylinder thickness $Re_D = 3000$, 8000 and 14000.The numerical code employed is *Nek5000*, it is based on a high-order spectral element method. The increase of Re_D leads to the anticipation of the transitional process along the leading-edge shear layer. This slightly affects the vortex shedding frequency. Variations in the mean flow topology mainly concern the upstream shift of the separation bubbles centre. The larger displacements are observed for the secondary bubble because of the reduced propensity to separate shown by the reverse flow with Re_D. Negative production phenomena taking place in the shear layer determine the weak dependence between the mean vertical velocity and the Reynolds number.

In conclusion, the present work provides two fresh sets of highly accurate DNS data representative of turbulence problems of scientific relevance. Such results constitute a base of information that might improve the physical understanding of turbulent flows and the development of turbulence models, both in the LES and RANS context.

Abstract in lingua italiana

La maggior parte dei flussi che si osservano in natura e nel campo dell'ingegneria sono turbolenti. La turbolenza promuove il mixing e il trasporto di massa, quantità di moto ed energia interna (calore). Nello studio della turbolenza l'approccio concettualmente più semplice, nonché il più accurato e dettagliato, è la simulazione numerica diretta (DNS). L'elevato costo computazionale richiesto, tuttavia, rende la DNS inadatta per la risoluzione dei problemi pratici tipici dell'industria. In tale ambito risulta invece più conveniente adottare un approccio modellistico, ma per definire teorie e modelli attendibili occorre disporre in principio di dati che siano precisi e con piccoli errori di discretizzazione. Questo lavoro si propone di fornire risultati con un elevato grado di accuratezza e dettaglio da utilizzare per lo studio e la comprensione di flussi turbolenti di interesse scientifico. A tale scopo, sono qui studiati due casi di turbolenza mediante DNS di ordine elevato.

Il primo caso analizzato riguarda la turbolenza generata a valle di una schiuma metallica a celle aperte. Questa configurazione di flusso rappresenta un nuovo caso di turbolenza di griglia, in cui la griglia regolare è sostituita da uno strato poroso che è localmente irregolare ma statisticamente isotropo. La geometria della schiuma metallica è riprodotta sinteticamente con una porosità di $\varepsilon = 0.92$ e uno spessore longitudinale pari a cinque volte il diametro medio dei pori d_p. La simulazione è effettuata utilizzando il codice DNS alle differenze finite di ordine elevato *Incompact3d* e il numero di Reynolds basato sul diametro dei pori è $Re_{d_p} = 4000$. Ad una distanza dalla schiuma minore di due volte il diametro dei pori, il trasporto dell'energia cinetica turbolenta per effetto della pressione e del termine turbolento non è trascurabile. A distanza maggiore si osserva lo scenario tipico della turbolenza di griglia, in cui la dissipazione dell'energia cinetica turbolenta è bilanciata dal termine convettivo medio. In questa regione le principali grandezze turbolente e le scale caratteristiche decadono con un andamento descritto da una legge di potenza. Gli esponenti di decadimento calcolati sono confrontati con quelli previsti dalle teorie classiche della turbolenza omogenea e isotropa.

Nel secondo caso si studia l'aerodinamica di un corpo tozzo a sezione rettangolare con rapporto lunghezza-altezza $c/D = 5$. Questa configurazione di flusso è rappresentativa di molte applicazioni sia nell'ingegneria civile che nell'aerodinamica dei corpi tozzi e recentemente è stata scelta come caso di riferimento per lo studio della separazione e riattacco di flussi esterni. Ai fini della ricerca sono effettuate tre DNS del flusso attorno al corpo rettangolare per diversi valori del numero di Reynolds basato sullo spessore del rettangolo $Re_D = 3000$,

8000 e 14000. Il codice impiegato è *Nek5000* e si basa sul metodo degli elementi spettrali di ordine elevato. L'aumento del Re_D accelera significativamente il processo di transizione lungo lo *shear layer*, mentre influenza solo debolmente la frequenza del *vortex shedding*. Nel flusso medio si osserva uno spostamento verso monte del centro di rotazione delle bolle di separazione, ed in particolare della bolla secondaria. Fenomeni di produzione negativa presenti nello *shear layer* sono responsabili dell'indipendenza tra il campo di velocità media verticale ed il numero di Reynolds.

In conclusione, in questo lavoro si presentano due nuove serie di dati DNS altamente accurate e rappresentative di flussi turbolenti rilevanti nell'ambito della ricerca. Tali risultati costituiscono una base di informazioni che potrebbero migliorare la comprensione fisica dei flussi turbolenti e lo sviluppo di modelli di turbolenza.

Table of contents

Introduction

Most flows observed in nature and engineering applications are turbulent, whether it be smoke from exhaust ducts of a car, swirls and waves in a flowing river or a blast of wind. Compared with laminar flows, turbulent flows possess greater efficiency in mixing fluids and enhanced rates of mass, momentum, and heat transfer. The occurrence of turbulent flow conditions and their capability to affect system performance are of prime importance for many applications in engineering and, for this reason, turbulence has been object of extensive studies through the years. However, owing to its complex and multiscale nature, the turbulence phenomenon has proven extremely difficult to describe from first principles and some of its aspects remain unexplained.

In this situation, efforts have been made aimed at developing mathematical models able to accurately predict the characteristics of turbulent flows. For fluid flows, the governing equations are derived from the conservation principles of mass and momentum. The direct approach of solving the governing equations, i.e. Direct Numerical Simulation (DNS), provides a detailed description of the time-dependent velocity field for one realization of the turbulent flow. Since all the length scales and time scales need to be resolved, the computational cost required by the DNS is extremely high. In addition, the steep rise of the computational effort with the Reynolds number[1] restricts the use of this approach to simple flows at moderate Reynolds numbers. Hence, the costly computational requirements combined with the huge amount of information to be elaborated prevent DNS to be used as a general-purpose tool in the design process of engineering applications, where high-Reynolds-number flows and complex geometries are prevalent. In such frameworks the only possibility to provide quantitative predictions of turbulent phenomena is via the adoption of a statistical approach in which the turbulent flow is described in terms of some statistical quantities, the simplest being the mean velocity field. The use of these statistics enables the formulation of a set of equations which can be tackled more efficiently, also when dealing with more complex geometries and higher Reynolds numbers. This is the case of Reynolds averaged Navier-Stokes (RANS) approach, which represents the standard in today's industrial practice, in which the Reynolds equations are solved for the average velocity field. In large-eddy simulations (LES), instead, equations

[1] It can be demonstrated that the computational cost scales as the cube of the Reynolds number for the case of homogeneous and isotropic turbulence [31].

are solved for a filtered velocity field which is representative of the energy-containing motions. For a complete review on these methods the reader is referred to the book by Pope [102].

The RANS and LES approaches are associated with different issues, the main of which is the closure problem arising from the nonlinearity of the governing equations. In general, the governing equations expressed in terms of a set of statistics contain supplemental statistics to those in the set considered. Consequently, one has to make assumptions to make the number of equations equal to the number of unknowns (to close the system of equations). Accordingly, these methods rely on modelling assumptions formulated to predict the behaviour of specific quantities in the turbulent flows. RANS models require closures to represent the turbulent stresses resulting from the averaging process, while LES requires models to account for the effects of the unresolved smaller-scale motions. The process of formulating turbulence models and the intrinsic assumptions underlying the RANS approach introduce approximations which undermine the accuracy of the flow representation and, consequently, the predictive ability of the method. With regards to LES methodologies, besides the modelling of unresolved scales, a potential uncertainty arises from their sensitivity on the filter characteristic length. This parameter could be accurately specified with a prior knowledge of the flow.

In the last decades, in addition to experimental observations, DNS approach has constituted an invaluable source of data to gather insights on turbulence phenomenology and its modelling. The development of quantitatively accurate theories and models may only rely on highly accurate data describing every detail of the turbulent flow field, from the largest to the smallest length and time scales. Fundamental in this regard is the use of high-order methods for space and time discretisations, which enable a superior representation of the turbulent motions over the full range of scales.

In the present work, high-fidelity DNS solutions concerning two different flow cases are presented. The first flow case is the turbulent flow generated by a uniform stream passing through an open-cell metal foam layer. This flow configuration represents a novel realization of grid turbulence where, in place of a regular grid or fractal grid, there is an irregular yet statistically isotropic porous matrix. Downstream of the metal foam, to a good approximation, statistically homogeneous and isotropic turbulence is achieved. Despite the model of homogeneous and isotropic turbulence itself is not suitable for describing any real turbulent flows, in principle it proves of great interest for describing the small-scale motions of real turbulent flows. Following Kolmogorov's first similarity hypothesis [68], it can be reasonably assumed that any fully developed turbulent flow with sufficiently high Reynolds number is locally homogeneous and locally isotropic. This permits considerable simplifications in the mathematical investigation. In other words, a better comprehension of grid-generated turbulence is valuable for turbulence theories involving high-Reynolds-number flows.

The second flow case considered is the separating and reattaching flow around an elongated rectangular cylinder with sharp corners. Flow separation represents one of the principal

challenges faced by turbulence predictions in bluff-body aerodynamics [113]. The main difficulties arise from the combined presence of small scales, owing to the occurrence of turbulence, and very large scales, owing to the presence of vortex shedding. Further issues are introduced when the separated flow has the possibility of reattachments, as in the case of rectangular cylinders with aspect ratios greater than 2.5. In these cases, both experiments and simulations based on models appear unable to provide an unequivocal description of the physical mechanisms involved [19]. In addition, as evidenced by Cimarelli et al. [29], the sharp-edge flow separation induces peculiar phenomena, such as backscatter of energy from the fluctuating field to the mean flow, that are not adequately treated by some turbulence modelling assumptions. In summary, the detailed analysis of the turbulent flow around an elongated rectangular cylinder, conducted at sufficiently high Reynolds numbers, could improve the current understanding of separating and reattaching flows and lead to the development of more robust turbulence models for practical flows.

The present work, summarized in the following, consists of three chapters and an appendix. In chapter 1, the governing equations describing the turbulent flows examined are introduced and the numerical techniques used by the simulation codes for their solution are described. The convenience of a representation of turbulence based on high-order spatial discretisations is pointed out. In chapter 2, the DNS of the turbulent flow past an open-cell metal foam is presented. After the assessment of the statistical homogeneity and isotropy of the turbulent flow, the main turbulent quantities evolution downstream of the metal foam is analysed. Among these are turbulent kinetic energy, rate of dissipation of turbulent kinetic energy and principal length scales of turbulent motions, such as the integral, Taylor and Kolmogorov scales. Two-point statistics, i.e. one-dimensional velocity spectra and structure functions of several orders, are used to study small-scale motions, also in relation to Kolmogorov's refined similarity hypotheses [69]. Transport of turbulent kinetic energy and of variances of velocity fluctuations are then investigated through the evaluation of corresponding budget terms. Chapter 3 is concerned with the DNS of the turbulent flow around a rectangular cylinder with chord-to-thickness ratio $c/D = 5$. Results from three simulations at increasing values of the Reynolds number are presented. The analysis is mainly focused on the effects of the Reynolds number, based on the comparison between the three simulations performed. In addition, the influence of the spatial resolution is also examined, based on the comparison between one of the simulations performed and DNSs reported in the literature for the same Reynolds number. Instantaneous visualizations of the vortical structures illustrate the main flow features. The aerodynamic loads and the characteristic time scales of the turbulent flow are then computed. The mean velocity field is analysed to identify the principal separation bubbles and the distribution of turbulent kinetic energy provides details about the transitional process along the leading-edge shear layer. Relevant quantities for engineering applications, such as viscous and pressure stresses on the cylinder side, are also assessed. Velocity autocorrelation coefficients evaluated in different regions of the flow are used to study

the statistically dominant structures, while one-dimensional spectra are used to inspect the energy content across the scales of motions. After the examination of the terms of turbulent kinetic energy budget, transport equations for components of the Reynolds stress tensor are obtained and described. Concluding remarks are drawn in the last section. An appendix is provided which contains a short investigation about the effects of a different metal foam porosity from that considered in the simulation presented in chapter 2.

Finally, it is worth pointing out that the large-scale DNSs presented in this work were carried out availing of HPC (High Performance Computing) resources, also provided through the PRACE (Partnership for Advanced Computing in Europe) research infrastructure. The simulation and post-processing of the turbulence past an open-cell metal foam were performed on the systems Marconi KNL (closed in January 2020) and Galileo operated by CINECA, in Italy. HPC resources for the simulations of the flow around the rectangular cylinder were provided by GENCI (Grand Équipement National de Calcul Intensif) on Joliot-Curie KNL and Rome systems hosted at the CEA's supercomputing centre TGCC (Trés Grand Centre de Calcul), in France.

Chapter 1

Formulation and numerical methods

1.1 Governing equations

The fluid flows examined in the present work are described by the mass conservation equation and the three-dimensional, unsteady Navier-Stokes equations for incompressible flows:

$$\begin{cases} \dfrac{\partial U_i}{\partial x_i} = 0, \\ \dfrac{\partial U_i}{\partial t} + \dfrac{\partial U_i U_j}{\partial x_j} = -\dfrac{\partial P}{\partial x_i} + \dfrac{1}{Re}\dfrac{\partial^2 U_i}{\partial x_j \partial x_j}, \end{cases} \tag{1.1}$$

complemented with appropriate initial and boundary conditions. The subscripts i and j take the values of 1, 2 and 3 to denote the streamwise direction, x, and the two cross-flow directions, y and z, respectively. U_i are the instantaneous velocity components (U, V, W), t represents time and P is the pressure. The fluctuating components of the flow quantities will be designated by the corresponding lower-case letters. All the variables are made non-dimensional by the velocity at the inlet U_∞ and a reference length scale L_{ref} which depends on the flow case:

$$U_i = \frac{U_i^*}{U_\infty}, \quad x_i = \frac{x_i^*}{L_{ref}}, \quad P = \frac{P^*}{\rho U_\infty^2}, \quad \text{and} \quad t = \frac{t^* U_\infty}{L_{ref}}, \tag{1.2}$$

where the superscript * denotes quantities expressed in dimensional form and ρ is density. The reference length scales are the mean pore diameter of the open-cell metal foam d_p for the grid turbulence case and the thickness of the rectangular cylinder D for the bluff body aerodynamics. The Reynolds numbers are defined accordingly:

$$Re_{d_p} = \frac{U_\infty d_p}{\nu}, \quad \text{and} \quad Re_D = \frac{U_\infty D}{\nu}. \tag{1.3}$$

1.2 High-order spatial discretisations

Central to the success of any direct numerical simulation of turbulence is the capability of the numerical model to properly represent all the relevant length scales. These requirements have led to the development of spectral methods [51, 22], which provide exponential convergence rate for infinitely smooth solutions. However, this fast convergence is limited to very simple flow configurations with simple boundary conditions. When the domain is irregular and more general boundary conditions need to be enforced, a satisfactory representation of the whole range of scales may be obtained using high-order finite difference schemes or spectral (finite) element schemes.

In the last decades, high-order discretisation procedures have been mostly used in the direct numerical simulation of turbulent flows because of the excellent properties shown in terms of accuracy of the solution and computational efficiency. More recently, high-order schemes have received increasing attention in the CFD (Computational Fluid Dynamics) community also in view of tackling more practical turbulence problems requiring an 'engineering accuracy', owing to their potential in delivering higher accuracy with lower computational cost than low-order discretisations [124]. Despite the classification between high- and low-order methods depends on the level of accuracy required in each context, in the CFD community are commonly designated as low-order the first and second order methods, while high-order schemes start at third order. Before discussing the main advantages of high-order discretisations, it is stressed the prime role of the resolution characteristics of the numerical approximations rather than their formal order of accuracy in direct simulations. Resolution characteristics refers to the ability of a numerical model to represent the exact result over the full range of length scales on a given mesh. The formal order of accuracy corresponds to the leading-order term in the truncation error of the scheme.

The main advantages of high-order discretisations with respect to low-order discretisations for direct numerical simulation are:

- Fast convergence. The rate of convergence of the numerical approximation to the exact solution is given by the formal accuracy of the method. In practice, the faster convergence achieved by high-order methods implies that the error in the numerical solutions decreases with much higher rate (orders of magnitude) when the grid is refined than for low-order methods.

- Small dispersion and dissipation errors. The resolution characteristics of finite-difference and finite element approximations can be effectively quantified by Fourier analysis[1] [121]. Figure 1.1 reports the results by Lele [78] about the modified wavenumbers for first-derivative approximations obtained for a variety of finite-difference schemes.

[1] Fourier analysis is rigorously applicable only to linear differential equations with constant coefficients, on uniform mesh and for periodic solutions.

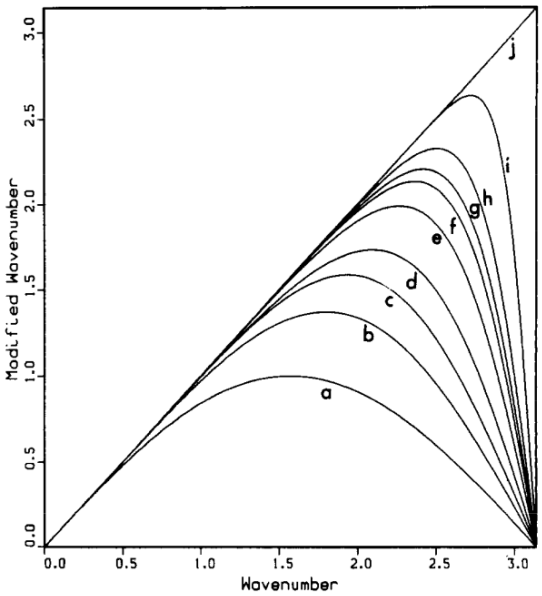

Figure 1.1. Modified wavenumbers for first-derivative finite-difference approximations: (*a*) second-order central differences; (*b*) fourth-order central differences; (*c*) sixth-order central differences; (*d*) standard Padé scheme; (*e*) sixth-order tridiagonal scheme; (*f*) eighth-order tridiagonal scheme; (*g*) eighth-order pentadiagonal scheme; (*h*) tenth-order pentadiagonal scheme; (*i*) spectral-like pentadiagonal scheme; and (*j*) exact differentiation. Reprinted from Lele [78].

The figure emphasises the ability of schemes of different order of accuracy to correctly represent the range of scales. Exact differentiation corresponds to the straight line and is provided only by spectral methods. Finite-difference schemes introduce dispersion error (and dissipation error) due to deviations from the exact differentiation at larger wavenumbers. The fraction of poorly resolved modes is significant for second-order scheme, but it is progressively reduced and limited to highest wavenumbers for high-order schemes. The deviations from the exact representation are enhanced for higher order derivatives.

- More efficient for time-dependent flow simulations with long-time integration. For the simulation of non-stationary problems, supposing that errors related with time discretisation can be neglected (for example by using a sufficiently small time-step), the computational cost required to reduce the solution error under a certain level is affected by the formal order of accuracy of the scheme and the time periods of integration. This is shown by the analysis of Kreiss and Oliger [70], who examined the dispersion errors of second, fourth and sixth order centred schemes when used to compute approximate solutions to linear first order hyperbolic equations. Despite higher-order schemes are characterized by wider stencils and thus a higher operation count, they appear superior

when the computations are extended over long time intervals. Their superiority is even much more marked when smaller errors are forced.

- Good performance for large-scale parallel computing. Algorithm efficiency can be achieved thanks to better data volume-over-surface ratio and better input/output handling due to the smaller volume of data.

1.3 Numerical methods

The governing equations (1.1) are solved numerically using high-order discretisations in space and time. To this aim, two high-order, state-of-the-art codes designed for direct numerical simulations of turbulent flows are used. Their numerical strategies are here briefly reported. For a detailed description of the numerical methods, the reader is referred to Laizet and Lamballais [74] and Deville et al. [40] for the grid turbulence and the bluff body aerodynamics cases, respectively.

1.3.1 Grid turbulence simulation

The numerical study of turbulence generated by an open-cell metal foam is based on the high-order finite-difference method applied by the open-source DNS code *Incompact3d* [75]. Sixth-order compact schemes are used for spatial discretisation [78], and time integration is done by the third-order Adams-Bashforth scheme. The velocity field is evaluated on a Cartesian grid with uniform spacing along the three directions, and pressure is defined on a staggered grid. Pressure-velocity decoupling is accomplished by a fractional-step method, which determines the divergence-free velocity field by solving a Poisson equation. The Poisson problem is tackled in the spectral space by using a modified wavenumber formalism, which allows for any kind of boundary conditions for the velocity field in the physical space.

Inflow/outflow boundary conditions are enforced along the streamwise direction and periodic boundary conditions are set along the cross-flow directions to represent statistical homogeneity. A uniform velocity field is prescribed at the inlet $(U_\infty, 0, 0)$, while at the outlet the velocity is determined by a convection equation:

$$\frac{\partial U_i}{\partial t} + c\frac{\partial U_i}{\partial x} = 0, \tag{1.4}$$

The convection velocity c is calculated at each time-step as the mean between the maximum and minimum values of the streamwise velocity component at the outlet.

Incompact3d is combined with an immersed boundary method (IBM) based on direct forcing to include relatively complex solid regions inside the flow domain. The use of an IBM allows for a detailed description of the intricate metal foam geometry on the Cartesian grid avoiding the computational cost increase associated with the use of a boundary fitted mesh.

Two direct forcing algorithms are implemented in the code. The first strategy consists in the explicit imposition of a zero-velocity field inside the solid body region. This approach is the simplest but can be problematic because of the discontinuity of spatial derivatives at the interface between fluid and solid regions which could give rise to spurious oscillations. The second method preserves the regularity of the solution across the immersed boundaries (while ensuring the no-slip condition at the walls) by means of a polynomial reconstruction of the velocity field inside the solid region based on the solution in the fluid region [74, 45]. Despite the latter strategy is preferable to achieve smooth solutions, it requires the metal foam ligaments to be thick enough and the fluid region in the interstices to be large enough to perform the polynomial reconstruction using the number of grid points required by the computational stencil. This condition is not always accomplished by the complex metal foam structure where sharp edges and thin walls are often observed. To avoid alterations of the metal foam geometry and since no spurious oscillations propagating from the solid surfaces have been noted, in the present work it was opted for the first IBM method reported.

1.3.2 Flow around rectangular cylinder simulations

The simulations of the turbulent flow around the rectangular cylinder with chord-to-thickness ratio $c/D = 5$ are carried out using the open source code *Nek5000* developed by Fischer et al. [42] and based on the spectral element method proposed by Patera [98]. The main advantage of spectral elements as compared to the Finite Difference and Finite Volume approaches is the expansion of the Finite Elements in terms of polynomials of generic degree p within the single element. The p-refinement strategy [62] ensures the exponential decay of the numerical error for increasing order of the interpolating polynomials (in the following text the order of polynomial will be indicated by N).

In each element, the governing equations are cast in a weak form and discretised by a Galerkin approximation, where the basis functions span polynomial spaces of maximum order N and $N-2$ for velocity and pressure respectively, following the $P_N - P_{N-2}$ approach. Velocity is represented by tensor products of Nth-order Lagrange polynomials on the Gauss-Lobatto-Legendre (GLL) quadrature points. Pressure is represented by polynomials of degree $N-2$ based upon the Gauss-Legendre (GL) quadrature points. In the simulations carried out the polynomial order is $N = 7$. Time advancement is performed by means of an implicit scheme consisting of a third-order backward differentiation scheme (BDF3) used in combination with a third-order extrapolation scheme (EXT3), for the explicit treatment of the convective term. The resulting method is third-order accurate in time.

The discretized equations are solved decoupling velocity and pressure into independent sub problems which are then solved iteratively. In particular, the Helmholtz equation is solved using the conjugate gradient method for velocity, whereas the Poisson equation for the pressure is solved with a generalized minimum residual (GMRES) method. For the pressure

equation, an efficient preconditioning strategy based on the overlapping additive Schwarz method [41] is adopted in which the associated coarse grid problem can be tackled by a highly-tuned algebraic multigrid (AMG) solver. For stabilisation of the spectral element method, de-aliasing is performed by over-integration of the convective term by a factor of 3/2 in each direction. For additional stabilisation, a filtering procedure based on a low-pass explicit filter built in modal space with a cut-off mode of $N-1$ and a weight of 0.02 is applied [43].

The inlet condition is of imposed free stream velocity U_∞. The outlet boundary condition is the traction-free condition. The same boundary condition is imposed in the vertical direction. Finally, periodicity is enforced along the spanwise direction, and a no-slip condition is imposed at the cylinder surface.

Chapter 2

Turbulent flow downstream of an open-cell metal foam

2.1 Introduction

Grid turbulence has been investigated for a long time owing to its good approximation to homogeneous and isotropic turbulence. In the classic flow configuration, a planar grid or screen with uniform mesh size and definite rod thickness is held in a uniform fluid stream. Downstream of the grid, homogeneity is achieved on cross-flow planes and a degree of isotropy is exhibited. This canonical flow has assumed an essential role in understanding turbulence and has allowed the formulation and testing of theories and models since the early wind tunnel experiments [112, 114].

The search for self-preserving or self-similar forms of correlation or spectral functions has led to the theories of homogeneous isotropic turbulence proposed over the past decades and the common prediction that turbulence decays according to a power law [122, 68, 9, 108, 46]. Even though these theories agree on the form, the value of the decay exponent n is still debated. The theoretical analyses by von Kármán and Howarth [122], Batchelor [9] and Saffman [108] resulted in values for n of 1, 10/7 and 6/5, respectively. A large collection of experimental measurements involving classical grids of various geometries and at different flow regimes has grown up over the years. While the earliest works supported the prediction that $n = 1$ [10], later experiments by Comte-Bellot and Corrsin [32] and Mohamed and Larue [86] corrected the decay exponent, with values falling between 1.1 and 1.4 [77, 73, 64, and references therein]. George [46] argued that the apparent discrepancies in the measurements are related to an undefined dependence of the flow on the initial conditions. This precludes the existence of a single universal state, at least at finite Reynolds number. Lavoie et al. [77] investigated the effects of the initial conditions on the characteristics of decaying turbulence and showed that this impact is more marked as the anisotropy and the strength of large-scale periodic motions increase. On the other hand, the improvement of isotropy and of large-

scale periodic character reduces the influence of initial conditions. This suggested that the dependence on initial conditions is associated with departures from the ideal homogeneity and isotropy conditions.

Recent research has attempted to reconcile many of the experimental data with Saffman turbulence. According to these analyses, the value $n = 6/5$ represents a minimum decay rate valid for (strictly) homogeneous turbulence and which could also have deviations because of an inhomogeneous decay. The large-scale turbulent structures are proven to be regulated by the invariance of the Saffman integral. This is physically interpreted as the conservation of linear momentum and is opposed to the invariance of the Loitsyansky integral, on which Batchelor turbulence is based. It is concluded in the work by Krogstad and Davidson [71] that "it seems very likely" that the turbulence observed is Saffman turbulence, and that it is also possible that different grid geometries, or other ranges of Re, could produce different results. Also Kitamura et al. [64] report that grid turbulence is of Saffman type for the Reynolds-number range examined in their work, when grid turbulence is generated by a square or a cylindrical grid.

Aside from the existence of a self-preserving solution, Mohamed and Larue [86] attributed the difficulty in finding a single decay exponent also to inconsistencies in the data analysis method. In particular, the inaccuracy is related to the uncertainty in the virtual origin and the inclusion of data pertaining to the inhomogeneous and anisotropic region in the developed range. For grid turbulence, the turbulence decay is to be evaluated starting from $x/M > 40$–60, where x is the distance from the grid and M is the mesh width.

A class of turbulence-generating grid consisting of fractal geometries has been introduced starting from the work by Hurst and Vassilicos [56]. Since then, fractal grids have attracted a lot of interest because of the specific type of turbulence generated. A remarkable increase in the Reynolds number based on the Taylor scale with respect to usual passive grids was noticed by Seoud and Vassilicos [110]. Further studies investigating the decaying turbulence downstream a set of multiscale grids [72] and a square-element fractal grid [53] have revealed that, while the region close to the grids can be characterised by residual inhomogeneity and is grid-dependent, in the far field –where development is accomplished– flow characteristics are in accordance with classical grid turbulence measurements.

The in-depth study of turbulence generated by fractal grids has revealed a peculiar behaviour of the dissipation coefficient $C_\epsilon = \langle\epsilon\rangle L/u^3$ (here $\langle\langle\epsilon\rangle\rangle$ is the rate of dissipation) in a region close to the turbulence-generating grid but in conjunction with energy spectra which follow the $-5/3$ slope for a wide range of wavenumbers. This behaviour has been described as a breakdown of the classical dissipation scaling and is observed in wind tunnel experiments of grid-generated turbulence of different geometries [85, 120, 57, 92] and in direct numerical simulation (DNS) data of decaying turbulence in a periodic box [49]. The breakdown consists in a behaviour of C_ϵ at the initial stages of the decay that depends upon the inlet Reynolds

number Re_M and the local Reynolds number Re_λ as follows: $C_\epsilon \sim Re_M^{1/2}/Re_\lambda$. This implies that $L/\lambda \sim Re_M^{1/2}$ along the direction of Re_λ decay [119].

The turbulent flow behind an open-cell metal foam has never been investigated before. Similar to regular grids, the open-cell metal foam geometry is characterised by two main length scales, i.e. the mean pore diameter d_p and the mean ligament thickness d_f. In contrast to regular grids, open cells are arranged randomly in space and their morphology, based on a polyhedral frame, is never exactly repeated. This generates a structure that is highly irregular and anisotropic at the pore scale but statistically isotropic at the macro-scale. In addition, the metal foam layer investigated here has a thickness larger than a single ligament or a pore. Moreover, the solidity of metal foams, measured as $1-\varepsilon$ where ε represents grid porosity, is very different from solidities typical of grids employed for grid turbulence, which generally range between 0.30 and 0.45. In high-porosity metal foams, this value is typically lower than 0.10 [20].

By means of the high-fidelity data and the high level of detail provided by the direct simulation method, this numerical study intends to analyse the nearly homogeneous and isotropic turbulence in the lee of a porous layer which, differently to previously investigated grids, is irregular and thicker in the mean-flow direction. In this context, the recognition of deviations from canonical grid turbulence that could be reasonably attributed to the distinctive geometry of the metal foam, could shed some light on the effects of boundary conditions on grid-generated turbulence, which are still undetermined.

2.2 Numerical procedure

2.2.1 Computational domain and simulation parameters

The DNS of the flow past the open-cell metal foam is performed at $Re_{d_p} = 4000$. The solution domain is a rectangular box with dimensions $L_x = 45\,d_p$ along the streamwise direction and $L_y = L_z = 11.25\,d_p$ along the two cross-flow directions, as sketched in figure 2.1. The origin of the coordinate system is located at the centre of the downstream face of the porous matrix, so that $x = 0$ describes the most upstream cross-flow plane where the fluid is not in contact with the solid phase. The thickness of the metal foam layer in the streamwise direction is $5\,d_p$ and it spans the whole domain in the cross-flow directions. It is placed at a $5\,d_p$ distance from the inlet section; this avoids interference between the upstream boundary and the solid matrix.

Spatial discretisation of the domain consists of about 1.8 billion grid nodes uniformly distributed in space, namely $n_x = 3073$ grid nodes in the streamwise direction and $n_y = n_z = 768$ in the cross-flow directions. The spatial resolution is sufficiently fine to ensure that $\Delta x = \Delta y = \Delta z \leq 2\,\eta$ for $x \geq 5$. Close to the porous layer ($0 < x < 5$), where dissipation is larger, $\Delta x = \Delta y = \Delta z \leq 5\,\eta$. In the above comparisons, the Kolmogorov microscale η is

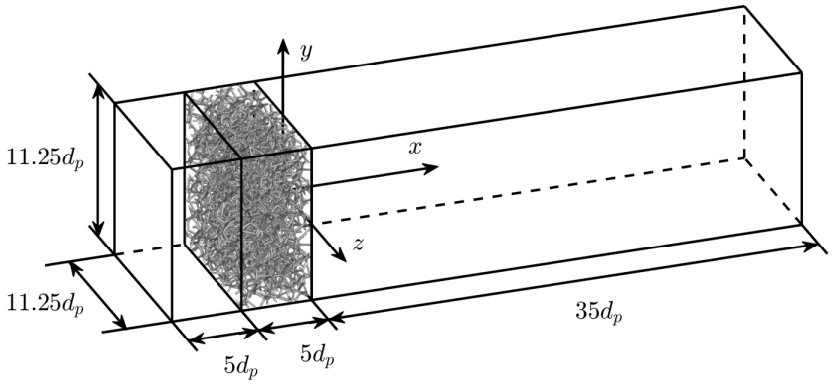

Figure 2.1. Schematic representation of the solution domain used for grid turbulence.

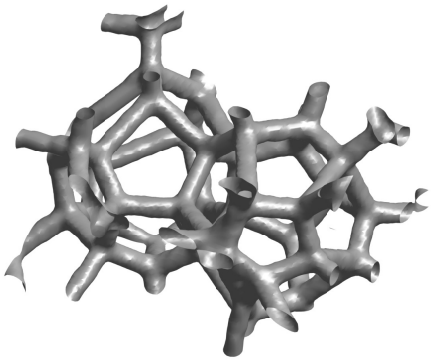

Figure 2.2. Cells of the aluminium foam generated algorithmically [7].

calculated *a posteriori* from its definition. The time-step is kept at $\Delta t = 0.001\, d_p/U_\infty$ during the simulation, which in terms of the Kolmogorov time scale τ_η yields $\Delta t \leq 0.033\tau_\eta$. This corresponds to a Courant-Friedrichs-Lewy number $CFL < 0.3$.

Statistical quantities are computed by averaging in time and along the homogeneous y and z directions. Gathering of statistics begins after one flow-through time from the start of the simulation. To obtain well-converged statistics, the time interval of collection is $T = 225\, d_p/U_\infty$, and the three-dimensional snapshots of the velocity and pressure field are sampled at equal time intervals of $\Delta T = 4.5\, d_p/U_\infty$.

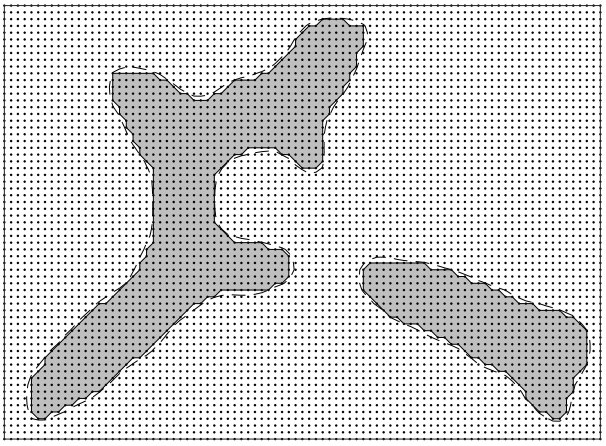

Figure 2.3. Subdivision of grid nodes into solid and fluid regions in a sample metal foam section. Dots indicate nodes of the Cartesian grid used, solid regions are depicted in grey while the fluid region is in white. Dashed lines outline the original ligaments shape.

2.2.2 Metal foam geometry

The problem of the computer modelling of an intricate metal foam porous structure has been tackled in different ways. Pore-scale morphology can be reconstructed through X-ray tomography [101] or generated mathematically assuming an ideal cell geometry based on a virtual sample of regular polyhedra [15]. In this study, where geometric periodicity is a key feature of the numerical representation and irregularity of the foam is a requirement, a third approach is adopted: the open-pore cellular structure is generated synthetically through a numerical algorithm, developed by August et al. [7]. Besides the excellent realism and periodicity, one further favourable feature of synthetic metal foams is the possibility to tune their porosity and permeability. Thanks to a diffuse interface representation of the phase-field approach [7], the thickness of ligaments can be easily adjusted. Figure 2.2 shows the details of a couple of cells of the synthetic structure.

The synthetic metal foam structure used in the simulation is characterised by the geometrical features listed in table 2.1. Both d_p and d_f are calculated by spatial averages and thus represent the mean pore diameter and the mean ligament thickness of the metal foam sample. The value of grid porosity set, $\varepsilon = 0.92$, is representative of high-porosity metal foams ($\varepsilon > 0.90$) [20]. Based on typical sizes of open-cell aluminium foams, an inflow velocity of $U_\infty = 15\,\mathrm{m\,s^{-1}}$ is obtained at $Re_{d_p} = 4000$, assuming air at standard conditions as the working fluid. Table 2.1 reports experimental conditions from previous wind tunnel studies on regular planar grids.

A sample of the metal foam geometry with superimposed computational points is displayed in figure 2.3. Staircase patterns of the immersed boundaries approximate the rounded borders

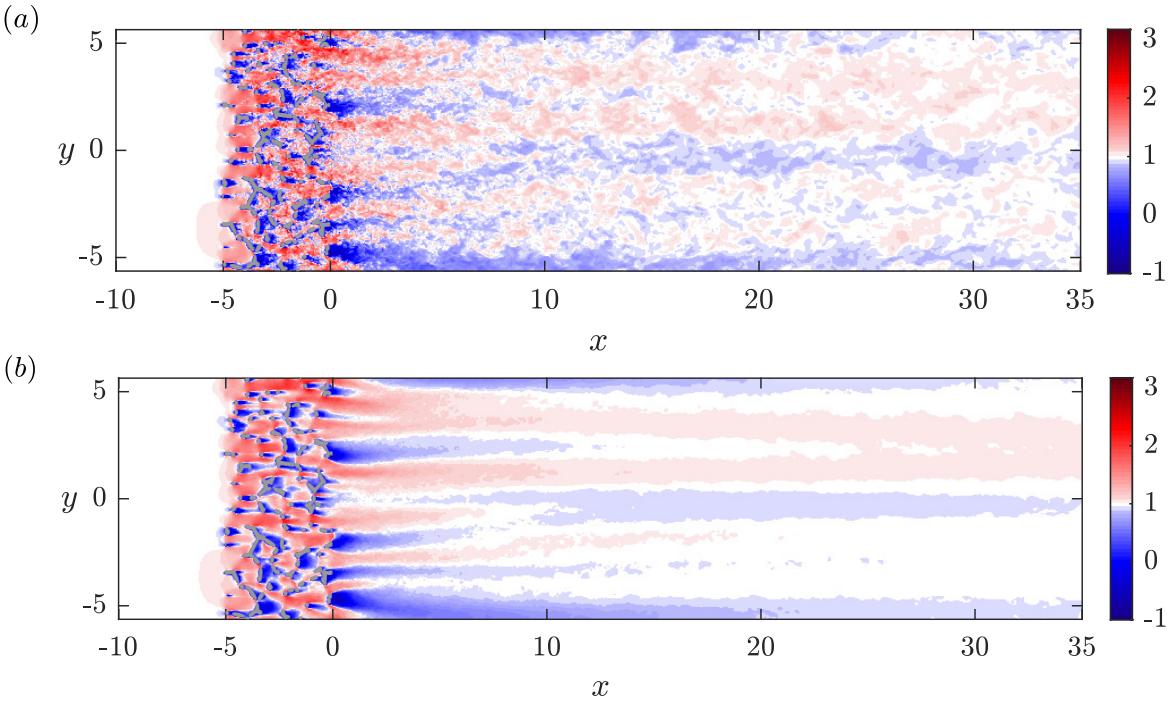

Figure 2.4. Instantaneous velocity field of the streamwise velocity component (a) and its temporal mean in the x–y plane (b).

of the solid region. The picture and the computed ratio between average ligament diameter and grid spacing $d_f/\Delta x \approx 10$ suggest that the ligaments are discretised by an adequate number of grid points.

2.3 Results

2.3.1 Instantaneous and mean flows

The mechanism by which turbulent motions are triggered in the flow domain is typical of grid turbulence, with the main difference that the turbulent flow passes through the intricate structure of the porous layer before to develop free of constraints in the region downstream. Figure 2.4(a) shows the streamwise component of the instantaneous velocity field in one of the snapshots collected. The uniform free stream of the inflow is disrupted by the irregularly arranged ligaments of the solid structure and velocity fluctuations arise within the porous matrix. Vortices of different orientations are shed from the ligaments and a wake is formed. The largest perturbations are observed close to the downstream edge of the porous matrix, where the streamwise velocity component can become as large as twice the free-stream and also become negative. The wakes originated by the ligaments develop in a non-uniform fashion and interact at variable lengths. The smaller wakes are seen to disappear after a couple of pore diameters, whereas larger wakes stemming from ligament clumps meet at a

Table 2.1. Outline of flow parameters, decay exponent n and length scales of turbulence generated by the open-cell metal foam. The experimental results of Comte-Bellot and Corrsin [33], Kurian and Fransson [73], Krogstad and Davidson [71] and Kitamura et al. [64] about turbulence generated by regular grids are also included. M, d and σ denote the mesh width, the rod thickness and the solidity of the grid, respectively. The superscript $*$ denotes quantities expressed in dimensional form. Round brackets indicate values that have been deduced from other quantities provided in the same work.

Present work	d_p^* (mm)	d_f^* (mm)	$1-\varepsilon$	U_∞^* ($\mathrm{m\,s^{-1}}$)	Re_{d_p}	Re_λ	n	η	λ	$L_\parallel$
Metal foam	4.00	0.56	0.08	15.0	4000	79–88	1.12	0.009–0.019	0.17–0.34	0.27–0.54
Reference	M^* (mm)	d^* (mm)	σ	U_∞^* ($\mathrm{m\,s^{-1}}$)	Re_M	Re_λ	n	η^*/M^*	λ^*/M^*	$L_\parallel^*/M^*$
Comte-Bellot and Corrsin [33]										
1 inch grid	25.4	4.8	0.34	10.0	17000	37–49	1.29	0.010–0.036	0.14–0.43	–
2 inches grid	50.8	9.5	0.34	10.0	34000	61–72	1.25	0.006–0.013	0.10–0.20	0.47–0.96
Kurian and Fransson [73]										
LT_1	0.96	0.24	0.44	12.0	760	(10–20)	1.59	0.067–0.385	0.58–2.28	0.95–2.34
LT_2	1.65	0.40	0.43	12.0	1310	(10–30)	1.52	0.034–0.260	0.47–1.85	0.78–2.03
LT_3	1.80	0.45	0.44	12.0	1420	(10–35)	1.50	0.031–0.244	0.41–1.88	0.56–1.96
LT_4	2.56	0.56	0.39	12.0	2030	(10–35)	1.50	0.029–0.197	0.41–1.54	0.61–1.61
LT_5	4.20	0.90	0.38	12.0	3320	(20–60)	1.45	0.022–0.123	0.43–1.33	0.75–1.47
A	36.0	6.0	0.31	8.0	19000	(85–180)	1.27	0.006–0.020	0.40	0.36–0.71
E	50.0	10.0	0.36	8.0	26400	(165–170)	1.53	0.004–0.009	0.25–0.34	0.52–0.79
Krogstad and Davidson [71]										
40 mm grid	40	10	0.44	13.5	36000	71–82	1.13	(0.006–0.014)	(0.11-0.29)	0.60–1.13
Kitamura et al. [64]										
$Cy10a$	10	2	0.36	10.6	6700	27–29	1.18	0.021–0.045	0.24–0.52	0.98–2.03
$Sq15a$	15	3	0.36	10.4	9600	47–50	1.15	0.012–0.021	0.22–0.37	0.72–1.25
$Sq15b$	15	3	0.36	17.2	16000	61–67	1.12	0.009–0.018	0.17–0.28	0.78–1.39
$Cy25a$	25	5	0.36	10.4	16000	59–65	1.12	0.006–0.014	0.15–0.23	0.40–0.67
$Cy25b$	25	5	0.36	20.0	33000	67–72	1.10	0.004–0.010	0.11–0.16	0.44–0.75
$Sq25a$	25	5	0.36	10.4	16000	58–64	1.16	0.005–0.010	0.15–0.22	0.46–0.80
$Sq25b$	25	5	0.36	20.0	33000	88–91	1.12	0.003–0.008	0.10–0.16	0.51–1.01
$Sq50a$	50	10	0.36	10.5	33000	99–112	–	0.002–0.005	–	0.29–0.48

further distance from the foam. The larger wakes also last in time, as revealed by the streaks in the time-averaged velocity field $\langle U \rangle_t$ shown in figure 2.4(b).

2.3.2 Homogeneity and isotropy

The approximation to statistical homogeneity in the cross-flow directions in grid turbulence is known to depend on the grid geometry and the Reynolds number. While, for regular grids, experiments suggest that the flow becomes nearly homogeneous for $x/M > 40$ [32, 86], for fractal grids, homogeneity is usually retrieved further downstream [53] and, for example, Valente and Vassilicos [118] report $x/M_{eff} > 80$, where M_{eff} is the effective mesh size.

The distribution of $\langle U \rangle_t$ in cross-flow planes is shown in figure 2.5 for six streamwise positions at increasing distance from the metal foam. Solid lines mark regions where the percentage of variation of $\langle U \rangle_t$ relative to U_∞ has magnitude greater than 10%, while dashed lines encompass regions of magnitude greater than 5%. These are seen to gradually shrink along x. While inhomogeneity is in part to be ascribed to the limited size of the sample composed only by the collection of snapshots in time, for $x > 20$ their extent is still appreciable. In the $x = 30$ station, the time-averaged velocity $\langle U \rangle_t$ varies between 0.86 and 1.12.

The most obvious measure of the large-scale isotropy in turbulence behinds grids is the equality between the root-mean-square (rms) values of the streamwise velocity fluctuation and any transverse velocity component fluctuation. Accordingly, a deviation from unity in the ratio between streamwise and transverse fluctuations states a certain degree of anisotropy of the flow. The x-distribution of anisotropy us represented in figure 2.6. In the present case, the fluctuations of the x-component of velocity are the largest: in the developed region, indicators $u_{\rm rms}/w_{\rm rms}$ and $u_{\rm rms}/v_{\rm rms}$ oscillate within the interval (1.5, 1.6) about a mean of 1.55 for $u_{\rm rms}/v_{\rm rms}$ and 1.56 for $u_{\rm rms}/w_{\rm rms}$, where the difference is finally due to the size of the sample employed in the simulations. In previous grid turbulence measurements [73, 71, 64], the observed isotropy indicators are in general smaller than those measured here. Kitamura et al. [64], who also collected experimental results by other authors, report $u_{\rm rms}/w_{\rm rms} < 1.2$ in all cases. Similar values are also reported in the lee of fractal grids [56, 48].

2.3.3 Skewness and flatness

Figure 2.7 shows the distribution along the x-axis of skewness and flatness of the streamwise fluctuating component u:

$$S_u = \frac{\langle u^3 \rangle}{\langle u^2 \rangle^{3/2}}, \qquad F_u = \frac{\langle u^4 \rangle}{\langle u^2 \rangle^2} \tag{2.1}$$

In the first region downstream the porous layer, $x \leq 5$, the velocity fluctuations demonstrate a non-Gaussian distribution. In particular, it is noted that S_u assumes also negative values which suggests the presence of decelerating flow events in the earlier stages of the flow. In the downstream region, $x \geq 15$, both S_u and F_u are close to the values corresponding

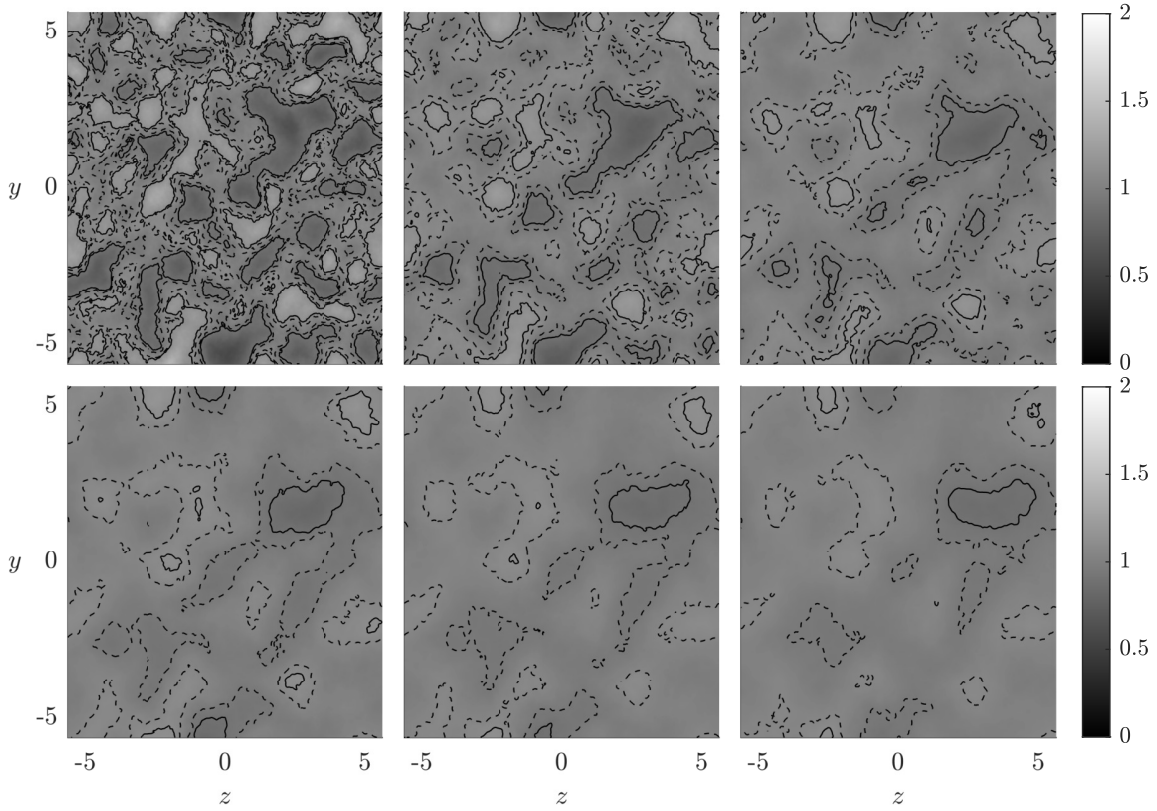

Figure 2.5. Streamwise mean flow field $\langle U \rangle_t$ in the y–z plane extracted at $x = 5$, 10, 15, 20, 25 and 30 (left to right then top to bottom): ——, isolines $\langle U \rangle_t - U_\infty = \pm 0.1$; and - - - -, isolines $\langle U \rangle_t - U_\infty = \pm 0.05$.

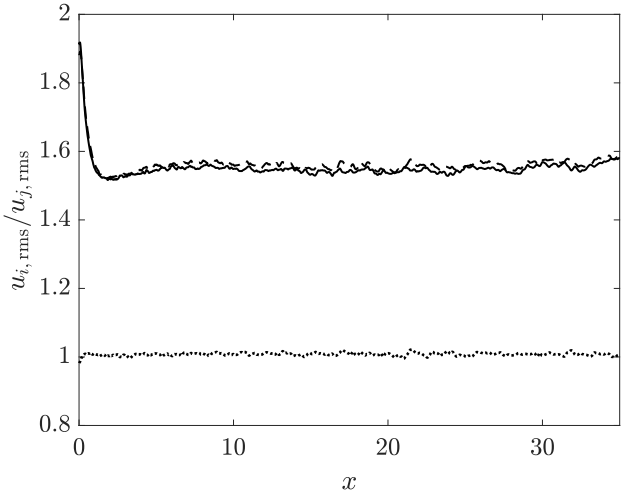

Figure 2.6. Streamwise evolution of the large-scale isotropy indicators: ——, $u_{\mathrm{rms}}/v_{\mathrm{rms}}$; - - - -, $u_{\mathrm{rms}}/w_{\mathrm{rms}}$; and ·····, $v_{\mathrm{rms}}/w_{\mathrm{rms}}$.

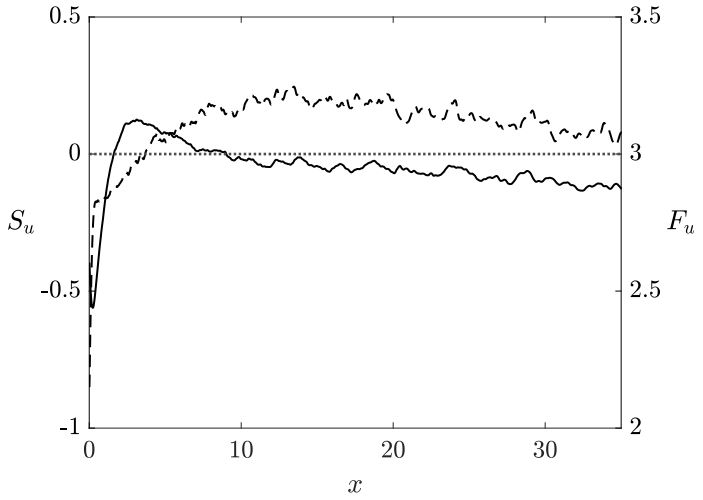

Figure 2.7. Streamwise evolution of the skewness and flatness of the streamwise fluctuating velocity: ——, S_u; and - - - -, F_u. The horizontal dotted line indicates the values $S_u = 0$ and $F_u = 3$.

to Gaussian distribution. In fact, skewness oscillates close to zero, as is typical in grid turbulence, but a slight decrease is noticed as the flow develops downstream. Flatness is somewhat above the Gaussian value $F_{u,G} = 3$. Skewness and flatness results are in fair agreement with previous wind tunnel experiments by Mohamed and Larue [86], Kitamura et al. [64], and Isaza et al. [57].

2.3.4 Decay of velocity fluctuations

Figure 2.8 displays the streamwise evolution of the variance of the three components of velocity $\langle u_i u_i \rangle$ as well as the turbulent kinetic energy $\langle k \rangle$. Very close to the foam and for $x < 1$, velocity fluctuations are observed to remain constant. The negative slope increases gradually in x until fluctuations exhibit a power-law decay that persists until the end of the computational domain. As demonstrated, for example, in Tennekes and Lumley [115], this is expected in the region where advection and dissipation of the turbulent kinetic energy become the only non-negligible terms in the transport equation of $\langle k \rangle$, see § 2.3.11.

Power-law parameters are sought in the form

$$\frac{u^2_{\text{rms}}}{U^2_\infty} = A \left(\frac{x - x_0}{d_p} \right)^{-n} \tag{2.2}$$

through a numerical procedure. In equation (2.2), A is the multiplicative coefficient, x_0 is the virtual origin and n is the decay exponent. As n is positive, the power law has a vertical asymptote (and a singularity) at the virtual origin $x = x_0$. As the parameters in equation (2.2) depend greatly upon the interval of sampling data considered, also the interval

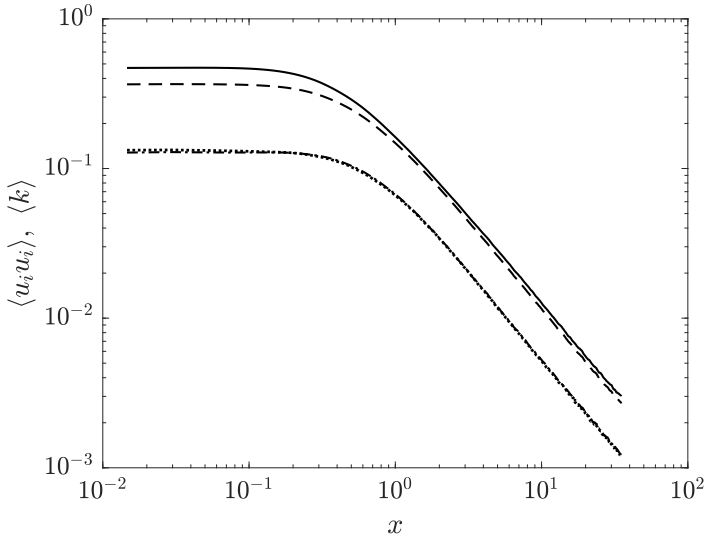

Figure 2.8. Decay of velocity fluctuations: ——, $\langle uu \rangle$; — · —, $\langle vv \rangle$; · · · · · ·, $\langle ww \rangle$; and - - - -, $\langle k \rangle$.

limits are determined inside the fitting procedure. A similar approach has been applied in Hearst and Lavoie [53].

In the present work, a developed region $I_d = [x_{\min}, x_{\max}]$ is employed, where the right border of the interval is kept fixed to $x_{\max} = 30.0$, clear of possible –yet not evident– outflow condition effects, while $x_{\min}$ is discretely varied in the interval $[0.015, 24.7]$ to seek for an $x_{\min}$ coordinate that ensures the best fit. The coordinate $x_{\min}$ will be taken as the start of the developed region. For each selection of a value for $x_{\min}$, the virtual origin x_0 is discretely varied within $I_0 = [0.015, x_{\min}]$, as the singularity is not supposed to belong to I_d. The intervals of variation of both $x_{\min}$ and x_0 are discretised by the same subdivision as the computational mesh. Parameters A and n are determined through a least-square fit. Deviations between computed data and fitting laws are then calculated as the Euclidean norm of the error divided by the number of data points:

$$e(x_0, x_{\min}) = \frac{\left(\sum_{j=1}^{N_d} \delta_j^2 \right)^{\frac{1}{2}}}{N_d}. \tag{2.3}$$

In equation (2.3), δ_j represents the difference between computed statistics and the least-square fitted power-law approximation of u^2_{rms} at the jth point of I_d; and N_d is the number of uniformly spaced points in the data fit region I_d. The $(x_0, x_{\min})$ couple which ensures the smallest deviation from computed data provides the final A and n coefficients. This procedure leads to the results given in table 2.2 with error distribution as in figure 2.9. In

Table 2.2. Left boundary of the fitting interval I_d, virtual origin, multiplicative coefficient, and decay exponent of the power-laws in the form of equation (2.2) fitting u^2_{rms} and $\langle k \rangle$.

	$x_{\min}$	$x_{\max}$	x_0	A	n
u^2_{rms}	7.98	30.0	0.648	0.155	1.12
$\langle k \rangle$	6.83	30.0	0.310	0.155	1.14

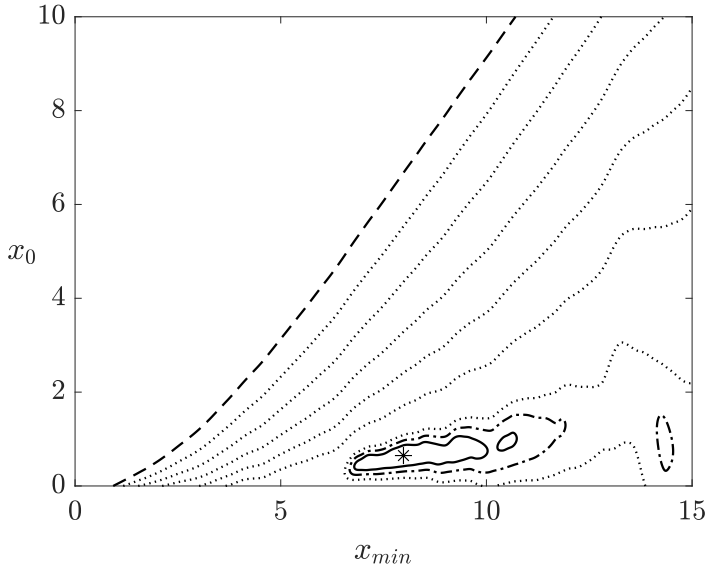

Figure 2.9. Contour lines of $\log_{10}(e)$, where e is the normalised Euclidean norm of the error in equation (2.3): - - - -, $\log_{10}(e) = -4.8$; — · —, $\log_{10}(e) = -6.03$; ——, $\log_{10}(e) = -6.05$; and ·····, $\log_{10}(e) \in [-6.00 - 5.00]$, with lines separated by $\delta = 0.2$. A single minimum is found in the field, as indicated by the $*$ symbol, which corresponds to $x_0 = 0.648$ and $x_{min} = 7.98$. The singularity is not included in the domain, and thus $x_{\min} > x_0$.

the region of parameters investigated, only one minimum is found, which is located far from the boundaries of the region investigated.

In order to check the dependence of the results from the fitting method employed, a procedure from the literature is also applied to the same set of data; this alternative technique is that utilised by Hearst and Lavoie [53]. In the application of the method to the present case, the virtual origin x_0 and lower bound $x_{\min}$ are varied within $I_0 = [0, 4]$ and $[4, 14.7]$, respectively. For both u^2_{rms} and $\langle k \rangle$, the process converges after three iterations. Applied to u^2_{rms}, this fitting procedure provides $x_0 = 0.610$ and $x_{\min} = 6.78$, which yield the estimate for $\widetilde{n}_u = 1.12$. In the case of $\langle k \rangle$, the values obtained are $x_0 = 0.360$, $x_{\min} = 5.02$ and $\widetilde{n}_k = 1.14$. The results obtained by the method proposed by Hearst and Lavoie [53] are only marginally different from those obtained as described above and reported in table 2.2.

Comte-Bellot and Corrsin [32] found $1.15 \leq n \leq 1.29$ for regular grids, while according to Mohamed and Larue [86] $n \approx 1.3$. More recently, Krogstad and Davidson [71] found $n = 1.13 \pm 0.02$.

Besides the parameters x_0, A and n in equation (2.2), the procedure provides the coordinate $x_{\min}$ of the start of the developed region as the left boundary of the interval I_d. All the subsequent fittings in this work will be carried out on $I_d = [7.98, 30.0]$.

2.3.5 Length scales

The length scales examined for the characterisation of the turbulence generated by a metal foam are the Kolmogorov scale η, the Taylor microscale λ and the integral scales. All the length scales are computed directly from their definitions. Their distribution within the developed region is approximated by a power law of the distance x. The range of variation of each length scale along I_d is reported in table 2.1 together with data from the literature on classical grid turbulence.

Kolmogorov scale

The Kolmogorov scale is representative of the smallest dissipative scales of turbulence and is defined through dissipation as follows,

$$\eta \equiv (Re_{d_p}^3 \langle \epsilon \rangle)^{-1/4}. \tag{2.4}$$

In grid turbulence, η can be represented by a function of the form $\eta \sim a_\eta x^s$ by assuming a power-law distribution of $\langle \epsilon \rangle$ in the developed region and by considering that in the same region the decay of $\langle k \rangle$ is regulated only by viscous dissipation, i.e. $\langle \epsilon \rangle \sim -\frac{\mathrm{d}k}{\mathrm{d}x}$. These assumptions hold true for the present case, as demonstrated in § 2.3.6 and 2.3.11. After a simple calculation it follows that $s = (n_k + 1)/4$. The decay exponent for $\langle k \rangle$ computed here, $n_k = 1.14$, gives $s = 0.54$. The power-law approximation is displayed in figure 2.10 together with the Kolmogorov scale, as computed from its definition: the fitting coefficients are $a_\eta = 0.00291$ and $s = 0.55$. Very similar power-law parameters are obtained in this same flow configuration for a porosity $\varepsilon = 0.97$; see appendix A. Comte-Bellot and Corrsin [33] provide Kolmogorov-scale measurements in their table 4, which grow like a power law of exponent $\hat{s} = 0.58$.

Taylor microscale

Figure 2.11 displays the streamwise distribution of the Taylor microscale, defined by

$$u_{\mathrm{rms}}^2 = \lambda^2 \left\langle \left(\frac{\partial u}{\partial x} \right)^2 \right\rangle. \tag{2.5}$$

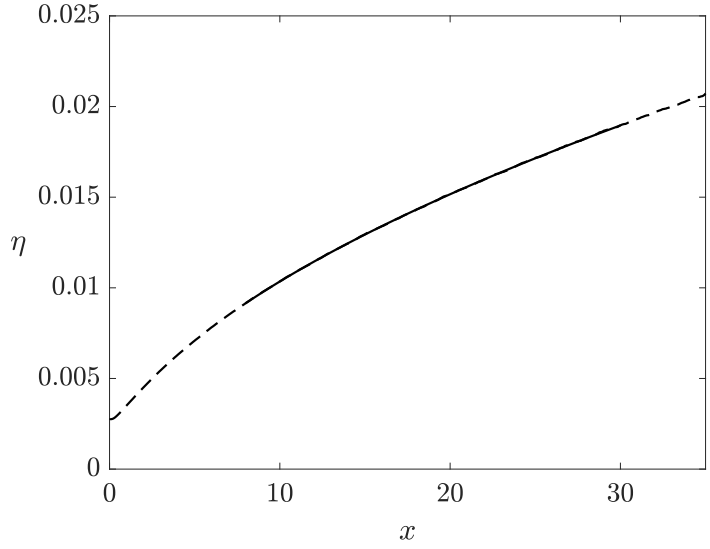

Figure 2.10. Streamwise distribution of the Kolmogorov scale: - - - -, η as calculated from its definition; and ——, $a_\eta x^s$, where $a_\eta = 0.00291$, $s = 0.55$. The uniform grid spacing adopted in all directions is $\Delta x_i = 0.0146$, which suggests that spatial resolution is high enough to represent the smallest scales of the turbulence.

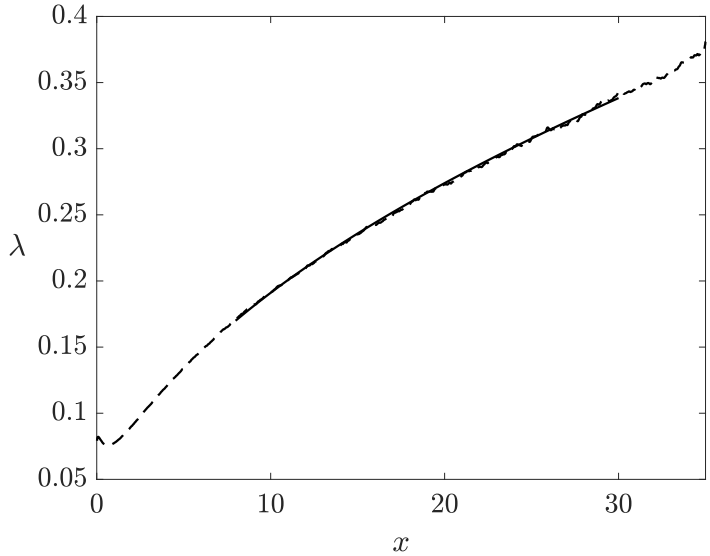

Figure 2.11. Streamwise distribution of the Taylor microscale: - - - -, λ as calculated from its definition; and ——, $a_\lambda x^c$, where $a_\lambda = 0.0577$ and $c = 0.52$.

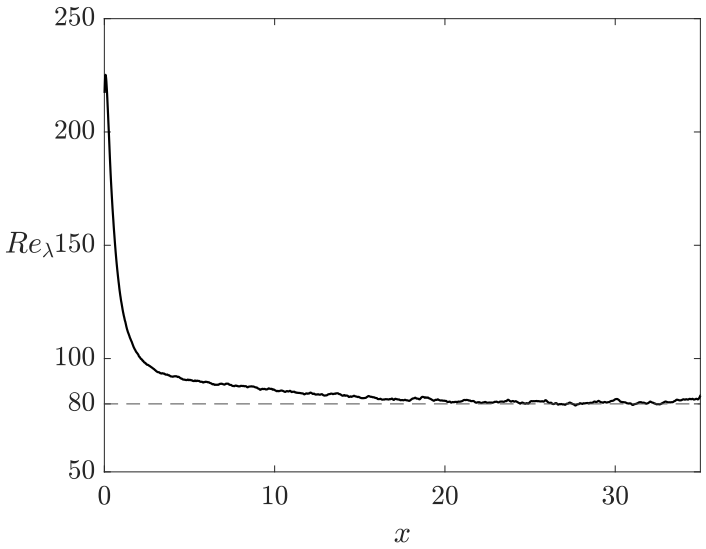

Figure 2.12. Streamwise distribution of Re_λ. The horizontal dashed line specifies the value $Re_\lambda = 80$.

Comte-Bellot and Corrsin [33] report Taylor-scale values in a few measurement points (see their table 4); their data fit a power law of exponent $c = 0.53$. It is predicted in the study by George [46] that the Taylor scale of homogeneous isotropic turbulence increases in time with $t^{1/2}$ and, for grid turbulence, λ grows as $x^{1/2}$ in the laboratory frame. More recently, Kurian and Fransson [73] reported that λ increases approximately like the square-root of the streamwise coordinate. In the present study, fitting a power-law approximation of the form $\lambda \sim a_\lambda x^c$ over I_d gives $a_\lambda = 0.0577$ and $c = 0.52$.

Figure 2.12 shows the behaviour of the turbulent Reynolds number. After a steep decrease in the vicinity of the metal foam, Re_λ reaches a plateau where $Re_\lambda \approx 80$. An expression relating the Taylor and the Kolmogorov scales can be obtained for isotropic turbulence through equation (2.11):

$$\frac{\lambda}{\eta} = 15^{1/4} Re_\lambda^{1/2}. \tag{2.6}$$

Results from the present investigation, and not reported for brevity, show that the difference between $(\lambda/\eta)^2/\sqrt{15}$ and Re_λ is less than 3% over the whole computational domain.

Integral scales

The autocorrelation coefficient is defined as the ratio between the autocorrelation function of separation $\boldsymbol{r} = r\boldsymbol{e}_j$ and the autocorrelation function for $r = 0$,

$$\rho_{ii}(x, \boldsymbol{r}) = \frac{R_{ii}(x, \boldsymbol{r})}{R_{ii}(x, 0)} = \frac{\langle u_i(\boldsymbol{x}) u_i(\boldsymbol{x} + \boldsymbol{r}) \rangle}{\langle u_i(\boldsymbol{x}) u_i(\boldsymbol{x}) \rangle}. \tag{2.7}$$

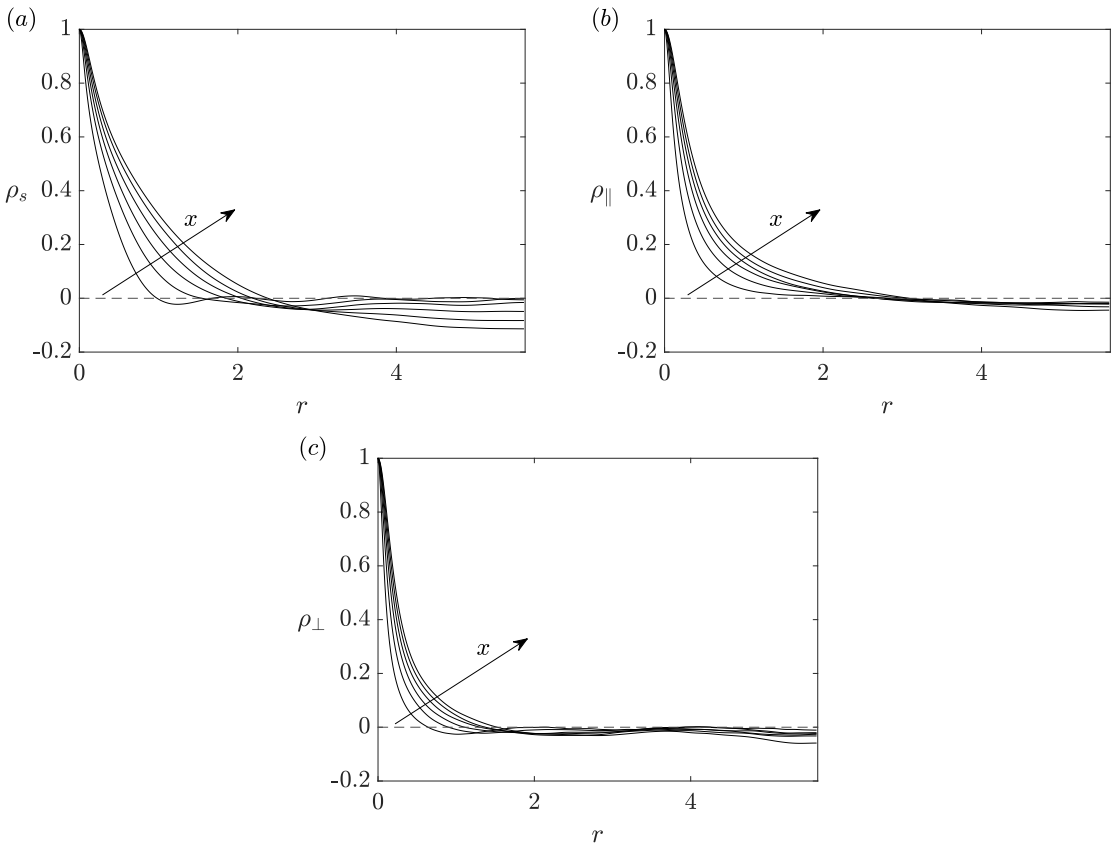

Figure 2.13. Streamwise, longitudinal and transverse autocorrelation coefficients of velocity fluctuations ρ_s (a), $\rho_\parallel$ (b) and $\rho_\perp$ (c) at six uniformly spaced locations from the metal foam, starting from $x = 5$ and ending at $x = 30$. A horizontal dashed line is used to distinguish between positive and negative correlation.

Given the inhomogeneity of the streamwise direction, separation is set in the cross-flow directions $\boldsymbol{e}_2$ and $\boldsymbol{e}_3$. A distinction is made between the transverse and longitudinal correlations depending on the *relative direction* of velocity components and separation vector. Thus, the autocorrelation coefficient based on the streamwise velocity is always transverse and will be denoted by ρ_s. The autocorrelation coefficients based on cross-flow velocity components can be either longitudinal or transverse and are denoted by $\rho_\parallel$ and $\rho_\perp$, respectively. As statistically $\rho_{11}(x, r\boldsymbol{e}_2) = \rho_{11}(x, r\boldsymbol{e}_3) = \rho_s(x)$, $\rho_{22}(x, r\boldsymbol{e}_2) = \rho_{33}(x, r\boldsymbol{e}_3) = \rho_\parallel(x)$ and $\rho_{33}(x, r\boldsymbol{e}_2) = \rho_{22}(x, r\boldsymbol{e}_3) = \rho_\perp(x)$, these equalities have been exploited in the calculation of autocorrelation coefficients.

The three types of autocorrelation coefficients computed are reported in figure 2.13. Transverse correlations built with streamwise velocity fluctuations have longer tails with respect to longitudinal correlations built with spanwise fluctuations. Furthermore, transverse coefficients have negative peaks which occur at increasing values of separation r with the distance x. These peaks of anticorrelation result from the presence of streamwise velocity

Table 2.3. Parameters of the power-law functions of the form $f(x) \sim ax^b$ fitting the turbulent quantities analysed.

	Power-law	Coefficient	Exponent
$\eta(x)$	$a_\eta x^s$	0.00291	0.55
$\lambda(x)$	$a_\lambda x^c$	0.0577	0.52
$L(x)$	$a_L x^q$	0.143	0.52
$L_\parallel(x)$		0.0946	0.51
$L_\perp(x)$		0.0555	0.51
$\langle\epsilon\rangle(x)$	$a_\epsilon x^h$	0.217	-2.20

streaks downstream of the metal foam, visible in figure 2.4(b). The separation length at which the peak is observed is a measure of the mean spanwise spacing between high and low streamwise velocity streaks and is found to increase up to $3.3\,d_p$ at $x = 30$.

Integral scales are defined as integrals over r of autocorrelation coefficients:

$$L_{ii}(x, \boldsymbol{e}_j) = \frac{1}{R_{ii}(x,0)} \int_0^\infty R_{ii}(x, r\boldsymbol{e}_j)\,\mathrm{d}r. \tag{2.8}$$

These depend upon the coordinates along non-homogeneous directions as well as on the direction of separation $\boldsymbol{e}_j$. In practice, since the computational domain has finite boundaries, the integral scales are calculated here as the distance over which the autocorrelation function decreases from 1 to 1/e, where e is Euler's number. For the calculation of integral scales, correlations are assumed to decay exponentially.

Integral scales for the present case are based on the streamwise or the cross-flow velocity components. By applying the same distinction and averaging procedure used for the autocorrelation coefficients, three types of integral length scales can be defined: the transverse length scale based on streamwise velocity L, the longitudinal length scale $L_\parallel$ and the transverse length scale based on cross-flow velocity $L_\perp$.

Figure 2.14 displays the integral scales. The power-law approximations $L \sim a_L x^q$ have the coefficients reported in table 2.3; the exponents computed are very close to the $L \sim x^{1/2}$ behaviour predicted by Wang and George [123]. Also, in the case of higher porosity presented in appendix A, the power-law exponent is close to 1/2.

Notice that L is one order of magnitude smaller than the domain size, the transverse length of which is of $11.25\,d_p$: this suggests that the imposed lateral periodic boundary conditions can satisfactorily represent cross-flow homogeneity in the present case. The evolution of the Reynolds number based on the integral scale, defined as $Re_L \equiv Lu_{\mathrm{rms}}/\nu$, along the x-axis is displayed in figure 2.15.

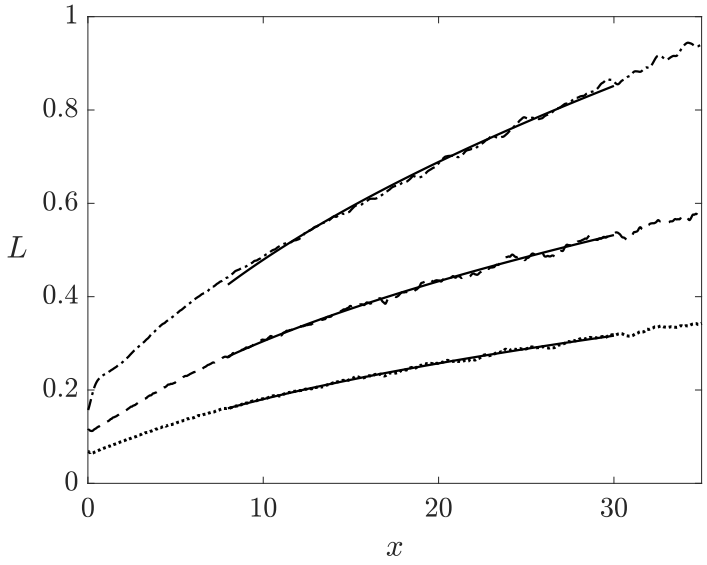

Figure 2.14. Streamwise distribution of the integral scales: — · —, streamwise integral scale L; - - - -, longitudinal integral scale $L_{\parallel}$; ·····, transverse integral scale $L_{\perp}$; and ——, power-law approximations of the different scales.

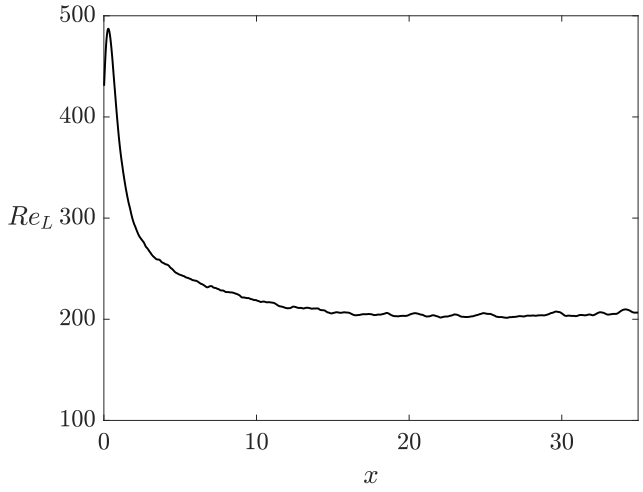

Figure 2.15. Streamwise evolution of Re_L.

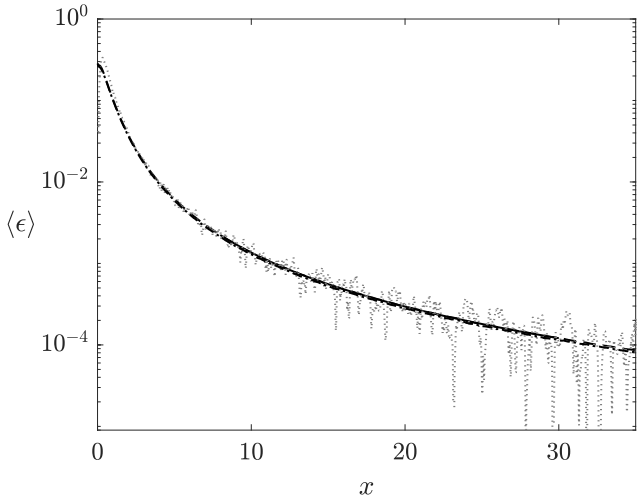

Figure 2.16. Streamwise evolution of the rate of dissipation of turbulent kinetic energy and its estimates: - - - -, $\langle\epsilon\rangle$ as defined in equation (2.9); ——, $a_\epsilon x^h$ where $a_\epsilon = 0.217$, $h = -2.20$; $\cdots\cdots$, $\langle\epsilon\rangle_{\text{tke}}$; and — $\cdot$ —, $\langle\epsilon\rangle_{\text{iso}}$. Line indicating $\langle\epsilon\rangle_{\text{spc}}$ falls almost exactly on the dashed line indicating $\langle\epsilon\rangle$ but is omitted from the figure for clarity.

2.3.6 Turbulence decay rate

The rate of dissipation of turbulent kinetic energy $\langle\epsilon\rangle$ is one of the important quantities to be accurately evaluated in grid-generated turbulence studies as it rules the Richardson-Kolmogorov cascade, it determines the budget in the fully developed region, it is related to the power-law decay of turbulent fluctuations along the streamwise direction, it provides the smallest scales of the flow and is the cornerstone of most turbulence models. As opposed to experimental studies, where rate of dissipation needs to be evaluated using the frozen turbulence assumption or isotropy, in DNS studies $\langle\epsilon\rangle$ can be computed directly from its definition,

$$\langle\epsilon\rangle \equiv \frac{2}{Re_{d_p}} \langle s_{ij} s_{ij} \rangle \,, \tag{2.9}$$

where $s_{ij} = \frac{1}{2}\left(\partial u_i/\partial x_j + \partial u_j/\partial x_i\right)$ is the fluctuating rate of strain.

Figure 2.16 displays the spatial evolution of $\langle\epsilon\rangle$, together with the least-squares fitted power law in the form $\langle\epsilon\rangle \sim a_\epsilon x^h$. The coefficients that fit the data over $I_d = [7.98, 30.0]$ are $a_\epsilon = 0.217$ and $h = -2.20$.

Approximation methods for dissipation in grid turbulence

As apparent form its definition, equation (2.9), the determination of $\langle\epsilon\rangle$ in experimental works is not an easy task and in most cases experimentalists resort to simplified expressions based on theoretical assumptions or models. In grid turbulence there are three commonly used methods to predict the dissipation rate; they are shortly described in the following.

The scaling of dissipation $\langle\epsilon\rangle$ can be set in relation to the scaling of $\langle k\rangle$. As also shown quantitatively in § 2.3.11, in the developed region of a statistically steady high-Reynolds-number flow, turbulence production is zero and the decay of turbulent kinetic energy is balanced by advection, then a first possible approximation to $\langle\epsilon\rangle$ is given by

$$\langle\epsilon\rangle_{\mathrm{tke}} = -\langle U\rangle \frac{\mathrm{d}k}{\mathrm{d}x}. \tag{2.10}$$

Equation (2.10) suggests that the decay exponent in this case should equal $h = -(n_k + 1)$. In the present study, $h = -2.20$ and $n_k = 1.14$ are calculated. The percentage difference between $-(n_k + 1)$ and h is below 3%.

A second possible approximation to the rate of dissipation of k is the simplified expression formulated by Taylor [114] under the hypothesis of statistically isotropic turbulence,

$$\langle\epsilon\rangle_{\mathrm{iso}} = \frac{15}{Re_{d_p}} \left\langle \left(\frac{\partial u}{\partial x}\right)^2 \right\rangle. \tag{2.11}$$

The third independent method is based on the universal form of the one-dimensional spectra in the inertial subrange. When the Reynolds number is high enough to set a clear scale separation, the longitudinal one-dimensional spectrum, defined in § 2.3.9, in the inertial subrange of isotropic turbulence is modelled by

$$E_{ii}(\kappa_i) = C_1 \langle\epsilon\rangle^{2/3} \kappa_i^{-5/3}, \tag{2.12}$$

where the value reported by Pearson et al. [99] and by Pope [102] for the free coefficient is $C_1 \approx 0.5$, and $i = 2$ or 3 for the present case. The approximated rate of dissipation, denoted by $\langle\epsilon\rangle_{\mathrm{spc}}$, is thus computed by finding the peak in the spectrum multiplied by $\kappa_i^{5/3}$ and assuming $C_1 = 0.5$. The limited wavenumber range for which equation (2.12) holds true for the present Reynolds number is best examined with the compensated spectra $\langle\epsilon\rangle^{-2/3} \kappa_i^{5/3} E_{ii}(\kappa_i)$ shown in figure 2.17 for $i = 2$.

The different approximations to $\langle\epsilon\rangle$ and the value computed directly from the definition are shown in figure 2.16. The approximation which relies on the balance between advection and dissipation of k and provides $\langle\epsilon\rangle_{\mathrm{tke}}$ is in general fair agreement. The irregular behaviour and discrepancies shown by $\langle\epsilon\rangle_{\mathrm{tke}}$ are due to the calculation involving the derivative of statistics, which can be irregular.

The level of anisotropy of the flow behind the metal foam is non negligible and higher than several canonical grid turbulence measurements, as shown quantitatively in § 2.3.2. In this context the very accurate prediction to ϵ ensured by $\langle\epsilon\rangle_{\mathrm{iso}}$ requires justification, which can be found in the circumstance that hypotheses commonly required for equation (2.11) to hold are more restrictive than strictly needed. The equivalence $\langle\epsilon\rangle_{\mathrm{iso}} = \langle\epsilon\rangle$ due to Taylor [114] indeed does not require the flow to be isotropic, instead it relies upon the equalities

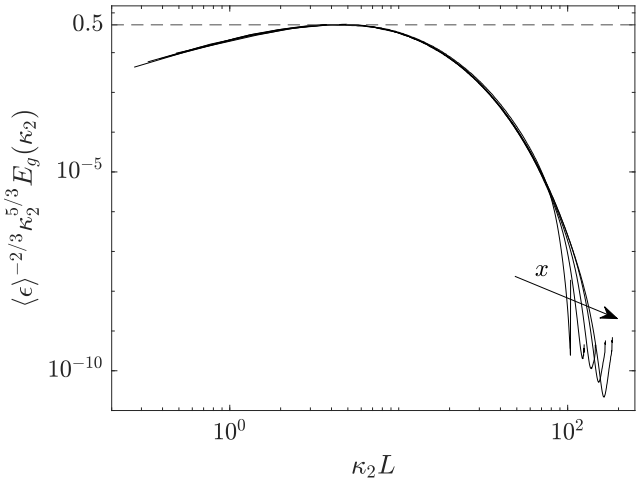

Figure 2.17. Compensated longitudinal spectra evaluated at regular intervals of $5\,d_p$ along the streamwise direction, from $x = 10$ to $x = 30$. The horizontal dashed line indicates $C_1 = 0.5$.

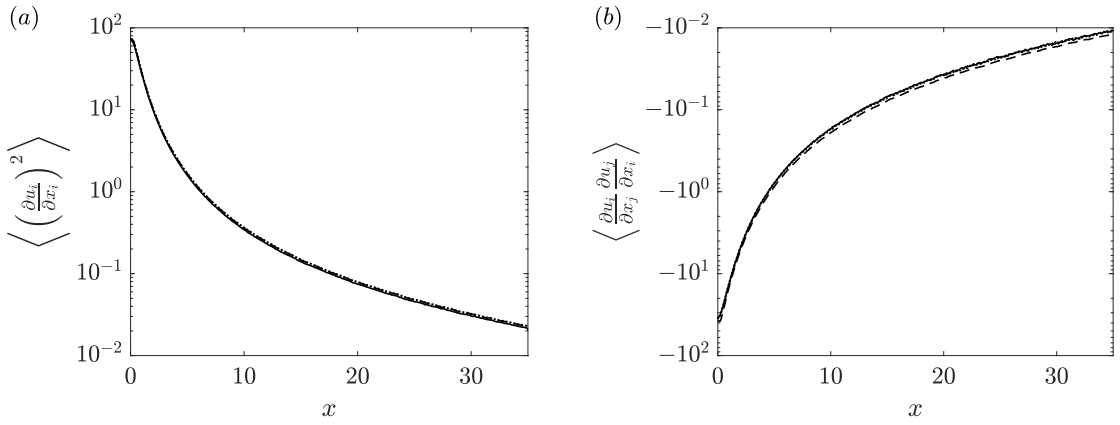

Figure 2.18. Streamwise evolution of squares and products of derivatives of velocity fluctuations. In panel (a) square terms are reported: ——, $\langle(\partial u/\partial x)^2\rangle$; - - - -, $\langle(\partial v/\partial y)^2\rangle$; and $\cdots\cdots$, $\langle(\partial w/\partial z)^2\rangle$. In panel ($b$) mixed product terms are reported: ——, $\langle(\partial v/\partial x)(\partial u/\partial y)\rangle$; - - - -, $\langle(\partial w/\partial y)(\partial v/\partial z)\rangle$; and $\cdots\cdots$, $\langle(\partial u/\partial z)(\partial w/\partial x)\rangle$.

between the mean values of mixed products and squares of the spatial derivatives of the velocity components,

$$\left\langle \left(\frac{\partial u_i}{\partial x_i} \right)^2 \right\rangle = \left\langle \left(\frac{\partial u_j}{\partial x_j} \right)^2 \right\rangle \tag{2.13}$$

and

$$\left\langle \frac{\partial u_i}{\partial x_j} \frac{\partial u_j}{\partial x_i} \right\rangle = \left\langle \frac{\partial u_k}{\partial x_i} \frac{\partial u_i}{\partial x_k} \right\rangle, \tag{2.14}$$

where the summation rule of repeated indexes does not apply. Equations (2.13) and (2.14) hold true in the isotropic case but are found to hold also in less strict conditions like the present grid turbulence results, see figure 2.18.

Also for equation (2.12) to hold, isotropy is required and again the accuracy of prediction is well beyond the fulfilment of hypotheses. This behaviour is ascribed to the flow displaying local isotropy despite the large scales being to some extent anisotropic, similar observation are reported by Krogstad and Davidson [71]. According to Kolmogorov's hypothesis of local isotropy, all the anisotropy is confined at the large scales, affected by the mean flow and boundary conditions, while the small-scale turbulent motions ($\ell \ll L$) are statistically isotropic. Local isotropy exists only under the hypothesis of a sufficiently high Reynolds number. For example, Tennekes and Lumley [115] suggest that Re_L should be at least $Re_L > 100$. In the whole region behind the metal foam the condition on the Reynolds number is well satisfied, as shown in figure 2.15. Further evidence of local isotropy is provided in § 2.3.9 and by the vertices of the compensated spectra converging to the same value assumed for C_1, see figure 2.17, which is acknowledged in the literature as typical for homogeneous and isotropic turbulence.

2.3.7 Dissipation rate coefficient

In high-Reynolds-number turbulent flows away from solid walls, the dissipation rate can be scaled on the integral length scale and velocity fluctuations through an order-one constant:

$$C_\epsilon = \frac{\langle \epsilon \rangle \, L}{u_{\mathrm{rms}}^3}. \tag{2.15}$$

Figure 2.19 shows that, in the present case, after an initial steep increase for $x < 2$, the dissipation rate coefficient C_ϵ based on L fluctuates over I_d between 0.45 and 0.50, where its spatial average is $\overline{C}_\epsilon = 0.483$. This value is very close to values reported in Pearson et al. [99] for shear turbulence at different Re_λ numbers.

Regarding the initial steep increase, in recent years Vassilicos and co-workers have observed that, close to the turbulence-generating grid, there is a region characterised by spectra that closely match the $-5/3$ power law, in conjunction with an increase in C_ϵ. In the hypothesis

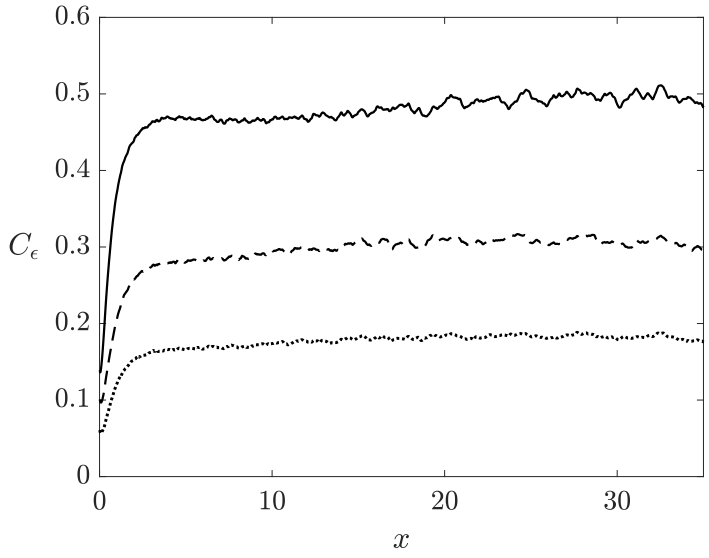

Figure 2.19. Streamwise distribution of $C_\epsilon = \langle\epsilon\rangle\, L/u_{\rm rms}^3$: ——, based on the streamwise integral scale L; - - - -, based on the longitudinal integral scale $L_\parallel$; and $\cdots\cdots$, based on the transverse integral scale $L_\perp$.

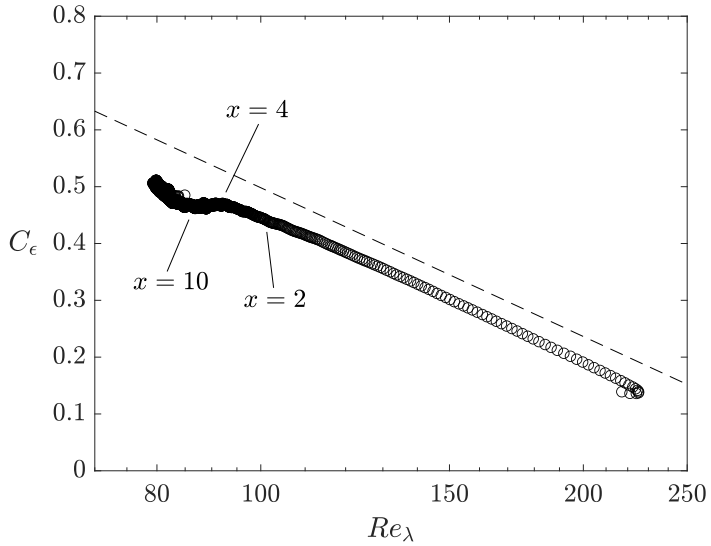

Figure 2.20. C_ϵ as a function of Re_λ. The dashed line follows Re_λ^{-1}.

of $\langle\epsilon\rangle = \langle\epsilon\rangle_{\text{iso}}$, combining the definition (2.15) with equation (2.11) leads to

$$C_\epsilon = 15\,\frac{L}{\lambda}\,\frac{1}{Re_\lambda}. \tag{2.16}$$

As only small variations of the ratio between length scales L/λ are observed for given Reynolds number of the mesh size, C_ϵ is seen to increase like Re_λ^{-1}. This behaviour is reported for both fractal and regular grids [119].

Equation (2.16) is studied for the present case in figure 2.20, where the logarithmic plot emphasises the $C_\epsilon(Re_\lambda)$ behaviour close to the metal foam. Corresponding to the initial steep decrease in Re_λ shown in figure 2.12, C_ϵ is seen to increase like Re_λ^{-1}. In the same region, a well-defined $-5/3$ energy spectra behaviour is observed over a broader wavenumber range than the fully developed region; see the inset of figure 2.22 in § 2.3.9. The situation described in Valente and Vassilicos [119] is thus observed in the present case.

The streamwise evolution of C_ϵ experiences a transition between the Re_λ^{-1} behaviour and a region where the variations in C_ϵ are much smaller; see figures 2.19 and 2.20. This transition is about $x = 2$. The turbulent kinetic energy budgets reported in § 2.3.11 indicate that, downstream of this location, the turbulent transport terms become negligible and the mean advection of $\langle k\rangle$ equals dissipation. On the contrary, for $x < 2$, this equality does not hold, and the variations of C_ϵ suggest a non-equilibrium condition between energy at the large scales and dissipation. It should be noted that the present results confirm the predictions reported by Tennekes and Lumley [115] in their (3.2.29) and (3.2.30), where transition is expected at streamwise distances from the grid that are much larger than the integral scale. In the present configuration, $x = 2$ corresponds to $x \approx 6L$.

In the theory by Richardson and Kolmogorov, the constancy of C_ϵ requires that turbulence is at a high Reynolds number and far from solid walls. While the small variations of C_ϵ in the fully developed region can be attributed to the Reynolds number, which is not very high, the steep increase in C_ϵ in the vicinity of the porous matrix ($x < 2$) is to be ascribed to the vicinity of the solid filaments and ultimately to non-negligible turbulent transport terms in the budget equation of $\langle k\rangle$.

2.3.8 Is grid turbulence Saffman turbulence?

In recent articles it was discussed [71, 64] whether grid turbulence can be considered to be of the Saffman type. Both Krogstad and Davidson [71] and Kitamura et al. [64] conclude that grid turbulence is Saffman turbulence.

The theory by Saffman [108] describes the decay of homogeneous turbulence as

$$u_{\text{rms}}^2 = K\,C^{2/5}\,t^{-6/5} \qquad L = K'\,C^{1/5}\,t^{2/5} \tag{2.17}$$

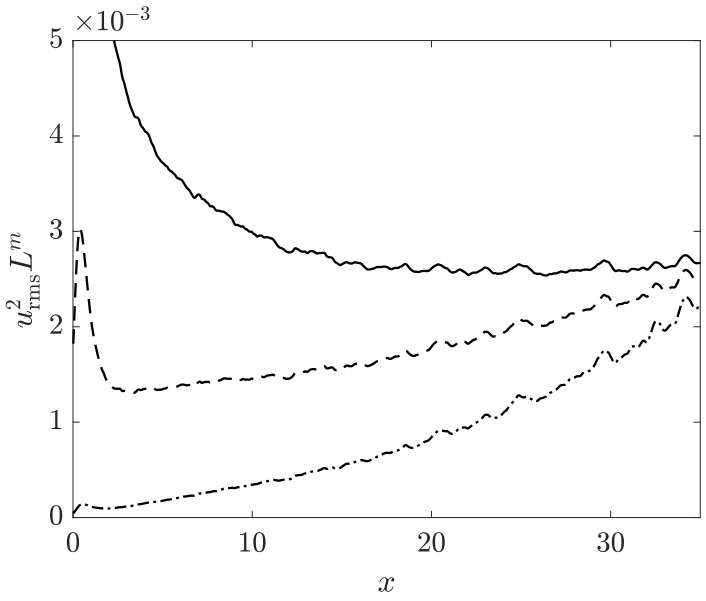

Figure 2.21. Streamwise evolution of the product of powers of the integral scale times powers of velocity fluctuations: ——, $u_{\mathrm{rms}}^2 L^2$; - - - -, $u_{\mathrm{rms}}^2 L^3$; and — · —, $u_{\mathrm{rms}}^2 L^5$. Saffman turbulence requires the constancy of $u_{\mathrm{rms}}^2 L^3 = \mathrm{const}$, not observed here.

where K and K' are constants and C is expressed by an invariant integral. Both equations in (2.17) have to hold for turbulence to be of the Saffman type. This is sometimes expressed by the requirement that $u_{\mathrm{rms}}^2 L^3 = \mathrm{const.}$ during decay, but the latter is a necessary, not sufficient, condition for Saffman turbulence.

The exponents reported in table 2.2 and 2.3 suggest that turbulence investigated in the present study is not of the Saffman type. Figure 2.21 provides graphical confirmation for this conclusion.

In the fully developed region of grid turbulence, as well as in the case investigated here, the advection of turbulent kinetic energy is almost perfectly balanced by dissipation:

$$\langle \epsilon \rangle \sim x^{-(n_k+1)}, \tag{2.18}$$

(see § 2.3.6). Setting $n_k = n_u = n$, equation (2.18) combined with the definition of C_ϵ in (2.15) and the hypotheses $L \sim x^q$ and $C_\epsilon \sim x^f$ leads to the following relation:

$$q = 1 - \frac{n}{2} + f. \tag{2.19}$$

As is apparent from (2.17) and (2.19), grid turbulence generated at $n = 6/5$ is not of the Saffman type unless C_ϵ stays constant during kinetic energy decay ($f = 0$).

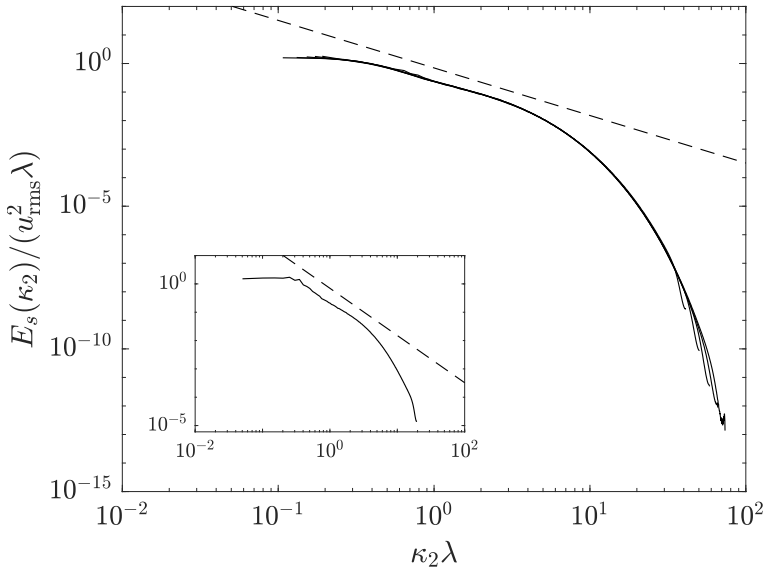

Figure 2.22. Streamwise one-dimensional spectra normalised in Taylor variables at increasing distance from the metal foam, $x = 10$, 15, 20, 25 and 30. The inset displays the power-law scaling exhibited by the spectrum at $x = 2$, as indicated by the dashed line with slope $-5/3$.

2.3.9 Spectral scaling and energy transfer

One-dimensional velocity spectra $E_{ii}(\kappa_j, x)$ are defined as

$$E_{ii}(\kappa_j, x) = \langle \hat{u}_i(\kappa_j, x)\hat{u}_i^*(\kappa_j, x)\rangle \,, \tag{2.20}$$

where κ_j are wavenumber components, the hat symbol denotes the one-dimensional Fourier transform, and the superscript * here indicates the complex conjugate. Again, only $j = 2$ and $j = 3$ are used because the streamwise direction is not homogeneous. Depending upon the pairing between velocity and wavenumber components, three distinct spectra can be calculated: streamwise spectrum $E_s = E_{11}(\kappa_j, x)$, longitudinal spectrum $E_\parallel = E_{jj}(\kappa_j, x)$, and transverse spectrum $E_\perp = E_{ii}(\kappa_j, x)$, where $i = 2$, $j = 3$ or $i = 3$, $j = 2$.

While, in general, spectra at different stages of the decay could be expected to scale with different reference quantities, it is observed here that, as factors $\eta\, u_\eta^2$, $\lambda\, u_{\mathrm{rms}}^2$ and $L\, u_{\mathrm{rms}}^2$ evolve at very similar rates in the streamwise direction (see table 2.3), any of those can be used equivalently. Spectra scaled by $\lambda\, u_{\mathrm{rms}}^2$ and evaluated at increasing distance along the x-axis are displayed in figure 2.22.

Figure 2.23 compares the three types of spectra, E_s, $E_\parallel$, and $E_\perp$, at a coordinate $x = 20$. For $\kappa_2\eta > 0.2$, the streamwise and transverse spectra almost coincide, which is a confirmation that anisotropy is at large scales only; see Mohamed and Larue [86] and Corsini and Stalio [38]. Only a narrow range in the wavenumber space ($0.025 < \kappa_2\eta < 0.1$) is noticed where E_s exhibits a $-5/3$ behaviour. Figure 2.23 includes the longitudinal spectra $E_{11}(\kappa_1)$ of

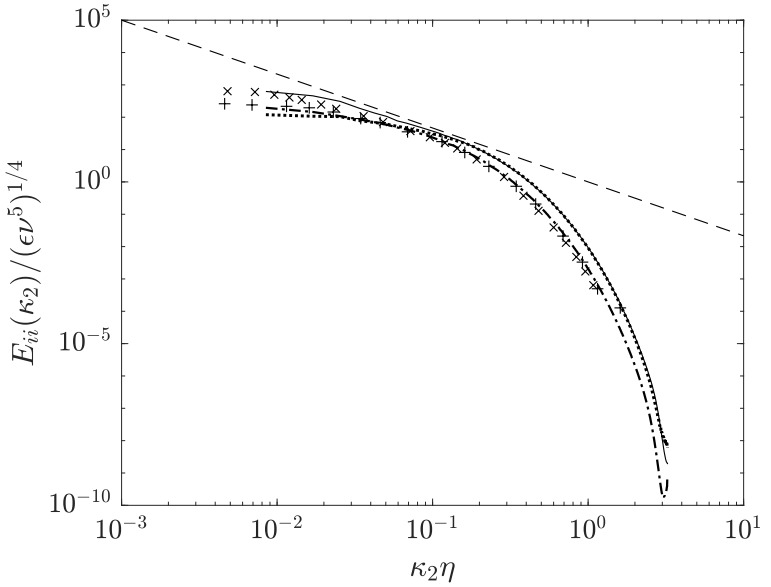

Figure 2.23. Comparison of streamwise, longitudinal and transverse spectra with Kolmogorov scaling at $x = 20$ ($Re_\lambda = 81$): ——, E_s; — · —, $E_\parallel$; ·····, $E_\perp$; and - - - -, $(\kappa_2\eta)^{-5/3}$. Symbols are longitudinal spectra of grid turbulence experiments from Comte-Bellot and Corrsin [33]: ×, $M^* = 50.8$ mm ($x^*/M^* = 98$, $Re_\lambda = 65$); and +, $M^* = 25.4$ mm ($x^*/M^* = 120$, $Re_\lambda = 41$). Asterisk * denotes quantities expressed in dimensional form.

Comte-Bellot and Corrsin [33] for two regular grids of different mesh size and Re_λ values in the same range as the present case ($Re_\lambda = 65$ and 41, compared to the present $Re_\lambda = 81$). Close agreement is observed between measurements in turbulence generated by classical grids and turbulence simulated in the high-porosity metal foam for $\kappa_2\eta > 0.1$.

The present results match canonical grid turbulence spectra for $\kappa_2\eta > 0.1$, the $-5/3$ law is not observed for wavenumbers $\kappa_2\eta > 0.1$, and local isotropy is observed for $\kappa_2\eta > 0.2$. That is the range of scales where dissipation becomes non-negligible. The distinction between scales containing the bulk of the energy from those responsible for dissipation is done by considering the energy spectrum $E(\kappa)$ and the dissipative spectrum $D(\kappa) = 2\nu\kappa^2 E(\kappa)$.

The turbulence spectrum $E(\kappa)$ is thus obtained by

$$E(\kappa) = -\kappa \frac{d}{d\kappa} \frac{1}{2} E_{ii}(\kappa), \tag{2.21}$$

where the summation convention is applied. The spectrum in equation (2.21) removes the directional information from both the velocities and the Fourier modes, as $E(\kappa)$ is given as a function of the wavenumber magnitude $\kappa = \mid \boldsymbol{\kappa} \mid$.

The kinetic energy cumulated at wavenumbers lower than κ is

$$k_{(0,\kappa)} = \int_0^\kappa E(\kappa')\mathrm{d}\kappa' \tag{2.22}$$

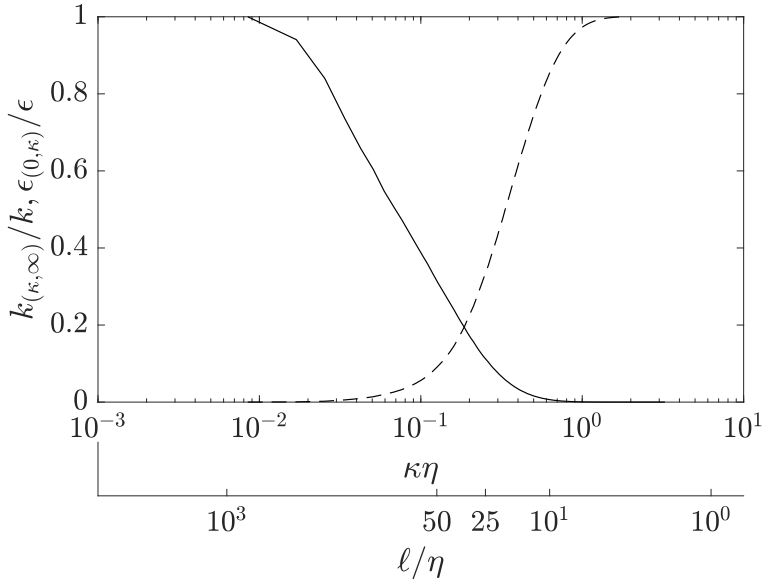

Figure 2.24. Normalised complement of the cumulative kinetic energy and normalised cumulative dissipation against wavenumber $\kappa\eta$ and wavelength ℓ/η at $x = 20$: ——, $k_{(\kappa,\infty)}/k$; and - - - -, $\langle\epsilon\rangle_{(0,\kappa)}/\langle\epsilon\rangle$.

the complement to $k_{(0,\kappa)}$ is indicated by $k_{(\kappa,\infty)}$. The corresponding quantities for the dissipation are obtained in the same fashion using $D(\kappa)$ and are indicated by $\langle\epsilon\rangle_{(0,\kappa)}$ and $\langle\epsilon\rangle_{(\kappa,\infty)}$. In figure 2.24 the fraction of cumulative turbulent kinetic energy at wavenumbers higher than κ and the fraction of cumulative dissipation at wavenumbers lower than κ at a distance from the foam $x = 20$ are depicted as functions of $\kappa\eta$ and of the corresponding wavelength $\ell/\eta = 2\pi/\kappa\eta$. The peak of the energy spectrum occurs at $\kappa\eta \approx 0.02$ (see figure 2.23) but it may be observed that the main fraction of the kinetic energy ($k_{(\kappa,\infty)} = 0.1\,k$) is contained in the range of wavenumbers up to $\kappa\eta \approx 0.25$, one decade further. The peak of dissipation is roughly at $\kappa\eta \approx 0.25$ (which corresponds to the maximum derivative in $\langle\epsilon\rangle_{(0,\kappa)}/\langle\epsilon\rangle$). The contribution to dissipation reaches $\langle\epsilon\rangle_{(0,\kappa)} = 0.9\,\langle\epsilon\rangle$ at $\kappa\eta \approx 0.7$. The bulk of turbulent kinetic energy is contained in motions of length scales $\ell > 25\,\eta \approx \frac{1}{2}L$; this range could be viewed as the energy-containing range. On the other hand, the dissipation is effective at the length scales $10\,\eta < \ell < 50\,\eta$. The overlap between $k_{(\kappa,\infty)}$ and $\langle\epsilon\rangle_{(0,\kappa)}$ reveals that energy starts to be dissipated at a length scale where the energy content is non-negligible.

2.3.10 Structure functions

In this section, the local structure of turbulence is investigated at $x = 25$ by analysing the scaling properties of the structure functions with separation r. The general definition of the pth-order velocity structure function is given by

$$\langle[\delta u_i(\boldsymbol{x},\boldsymbol{r})]^p\rangle = \langle[u_i(\boldsymbol{x}+\boldsymbol{r},t) - u_i(\boldsymbol{x},t)]^p\rangle. \tag{2.23}$$

Because of turbulence decay along x, two different structure functions are identified in this work: longitudinal structure functions $\langle(\delta u_\parallel)^p\rangle = \langle[\delta u_j(x, r\boldsymbol{e}_j)]^p\rangle$ and transverse structure functions $\langle(\delta u_\perp)^p\rangle = \langle[\delta u_i(x, r\boldsymbol{e}_j)]^p\rangle$, where $i = 2$, $j = 3$ or $i = 3$, $j = 2$.

According to the first, original theory by Kolmogorov [68], for high Reynolds numbers when the separation lies in the inertial subrange $\eta \ll r \ll L$, the moments of velocity difference $\langle(\delta u_\parallel)^p\rangle$ take a universal form that depends only on $\langle\epsilon\rangle$ through the following scaling property:

$$\langle(\delta u_\parallel)^p\rangle \sim (\langle\epsilon\rangle r)^{\zeta_\parallel^p} \quad \text{with} \quad \zeta_\parallel^p = p/3. \tag{2.24}$$

However, in both numerical and experimental results are found substantial deviations of $\zeta_\parallel^p$ from the linear behaviour, especially with increasing order p. The only exception regards the third order structure functions, which obey the so-called 4/5 law derived by Kolmogorov [67] from the Navier-Stokes equation under the assumption of homogeneous and isotropic turbulence, and given by

$$\langle(\delta u_\parallel)^3\rangle = -\frac{4}{5}\langle\epsilon\rangle r + \frac{6}{Re}\frac{\mathrm{d}}{\mathrm{d}r}\langle(\delta u_\parallel)^2\rangle, \tag{2.25}$$

where the second term of the right hand side is usually neglected for $r \gg \eta$. This law represents the only exact and non-trivial result in fully developed turbulence and yields $\zeta_\parallel^3 = 1$. In the refined similarity theory [69], the intermittency effects are considered by rewriting expression (2.24) in terms of ϵ_r, the dissipation averaged over a volume of linear dimension r, and assuming that ϵ_r has a log-normal distribution

$$\langle(\delta u_\parallel)^p\rangle \sim \langle\epsilon_r^{p/3}\rangle r^{p/3} \sim r^{\zeta_\parallel^p} \quad \text{with} \quad \zeta_\parallel^p = \frac{1}{3}p - \frac{1}{18}\mu p(p-3), \tag{2.26}$$

where μ is the exponent of the dissipation autocorrelation function,

$$\langle\epsilon(\boldsymbol{x}+\boldsymbol{r})\epsilon(\boldsymbol{x})\rangle \sim \left(\frac{L}{r}\right)^\mu, \tag{2.27}$$

again for inertial range separations [89].

Given the Reynolds number $Re_\lambda \approx 80$ of the present case, the study is conducted using the extended self-similarity (ESS) observation by Benzi et al. [11]. The pth moments of velocity differences $\langle(\delta u_\parallel)^p\rangle$ calculated at moderate Reynolds number are characterised by the same scaling exponents as in the high-Reynolds-number case when $\langle(\delta u_\parallel)^p\rangle$ are treated as functions of $\langle|\delta u_\parallel|^3\rangle$. The resulting exponents are indicated by $\xi_\parallel^p = \zeta_\parallel^p/\zeta_\parallel^3$ to discriminate them from those evaluated directly, $\zeta_\parallel^p$. The quality of the ESS scaling is displayed in figure 2.25 and in table 2.4. Errors are calculated by summing the uncertainty obtained from the estimate of scaling in the two spatial directions y and z and by modifying the scaling range over which $\xi_\parallel^p$ is evaluated in the interval $[3, 30]\eta$. Data from the literature reported for comparison in table 2.4 are at Re_λ comparable to the present, i.e. of order $\sim 10^2$, except for those by Iyer

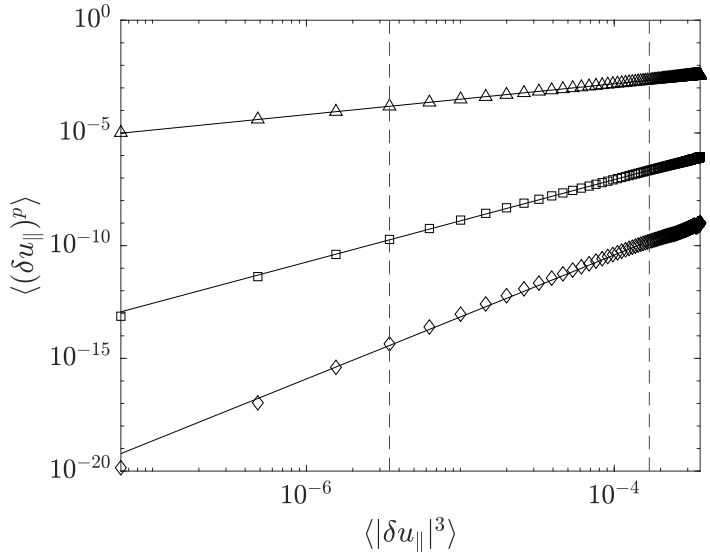

Figure 2.25. Log-log plot of second-, sixth- and tenth-order longitudinal structure functions versus $\langle|\delta u_{\parallel}|^3\rangle$ at the position $x = 25$: $\triangle$, $p = 2$; $\square$, $p = 6$; and $\Diamond$, $p = 10$. The straight lines superimposed onto the curves are the power laws resulting from the fitting procedure in the extended inertial range indicated by the dashed vertical lines. This range starts at 3η and ends at 30η.

et al. [58], which are obtained at $Re_\lambda \approx 1300$ and a high degree of isotropy. Results for the transverse structure functions are listed in table 2.5. There are no evidences relating the transverse to longitudinal structure functions of generic order, except for the second order moments which should scale the same way in the large Reynolds number limits given that for incompressible isotropic flows holds the exact relation derived from the Kármán-Howart equation [89]

$$\langle(\delta u_{\perp})^2\rangle = \langle(\delta u_{\parallel})^2\rangle + \frac{r}{2}\frac{\mathrm{d}}{\mathrm{d}r}\langle(\delta u_{\parallel})^2\rangle. \tag{2.28}$$

In the present work, the percentage difference between $\xi_{\parallel}^{p}$ and $\xi_{\perp}^{p}$ is 2% for $p = 2$.

Figure 2.26(a) shows scaling exponents $\xi_{\parallel}^{p}$ and $\xi_{\perp}^{p}$ computed using the ESS method, compared to the original predictions by Kolmogorov [68] extended to $p > 3$, the refined similarity hypotheses of [69], the intermittency β model by Frisch et al. [44] and the model by She and Leveque [111]. The transverse scaling exponents $\xi_{\perp}^{p}$ in figure 2.26 are obtained by making $\langle(\delta u_{\perp})^p\rangle$ depend on the magnitude of transverse velocity differences for $p = 3$ rather than the longitudinal, thus following the ESS method [21, 52]. The refined similarity hypotheses are found to hold, but there is a visible tendency of $\xi_{\perp}^{p}$ to deviate from the longitudinal scaling for $p \geq 4$. This is to be ascribed to the Reynolds number and the residual anisotropy of the flow, as argued by Iyer et al. [58].

Figure 2.26(b) displays the evolution of the intermittency exponent μ along the streamwise direction; the quantity defined in equation (2.27) is also employed in the β-model by Frisch

Table 2.4. Scaling exponents for the longitudinal structure functions $\langle(\delta u_{\parallel})^p\rangle$ of even orders up to $p = 12$ calculated using the direct and the ESS methods. Comparison of the present work with the results from Zhou and Antonia [129], Boratav and Pelz [16] and Iyer et al. [58].

	Present work $Re_\lambda \approx 80$		Zhou *et al.* $Re_\lambda \approx 75$	Boratav *et al.* $Re_\lambda \approx 100$	Iyer *et al.* $Re_\lambda \approx 1300$
Order p	Direct	ESS	ESS	ESS	Direct
2	0.722 ± 0.027	0.684 ± 0.005	0.70	0.6931	0.72 ± 0.002
4	1.343 ± 0.052	1.296 ± 0.008	1.32	1.2818	1.30 ± 0.005
6	1.852 ± 0.076	1.829 ± 0.032	1.86	1.7804	1.78 ± 0.010
8	2.241 ± 0.128	2.303 ± 0.068	2.34	2.2123	2.18 ± 0.021
10	2.507 ± 0.272	2.748 ± 0.126	-	2.6000	-
12	2.679 ± 0.509	3.187 ± 0.208	-	2.9614	-

Table 2.5. Scaling exponents for the transverse structure functions $\langle(\delta u_{\perp})^p\rangle$ of even orders up to $p = 12$ calculated using the ESS method. Comparison of the present work with the results from Zhou and Antonia [129], Gotoh et al. [50] and Iyer et al. [58].

	Present work $Re_\lambda \approx 80$		Zhou *et al.* $Re_\lambda \approx 75$	Gotoh *et al.* $Re_\lambda = 381$	Iyer *et al.* $Re_\lambda \approx 1300$
Order p	Direct	ESS	ESS	Direct	Direct
2	-	0.699 ± 0.011	0.72	0.701 ± 0.01	0.72 ± 0.003
4	-	1.268 ± 0.020	1.22	1.26 ± 0.03	1.30 ± 0.010
6	-	1.712 ± 0.082	1.59	1.69 ± 0.05	1.76 ± 0.015
8	-	2.057 ± 0.170	1.87	2.00 ± 0.04	2.12 ± 0.020
10	-	2.343 ± 0.270	-	2.20 ± 0.06	-
12	-	2.598 ± 0.372	-	-	-

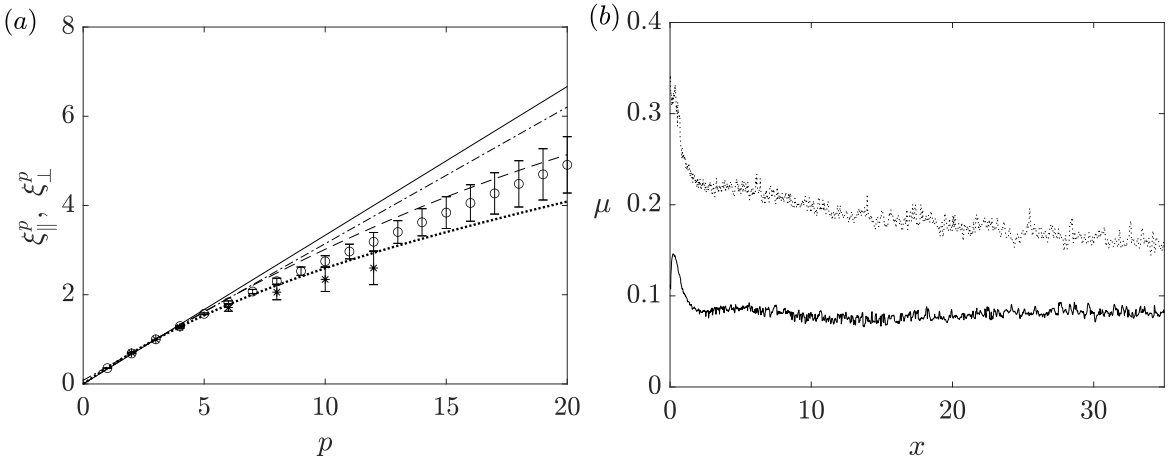

Figure 2.26. (a) Scaling exponents $\xi_\parallel^p$ and $\xi_\perp^p$ computed with the ESS method versus p for orders up to 20 ($x = 25$). In the same plot there are the results from different intermittency models assuming $\mu = 0.08$: ◯, $\xi_\parallel^p$; ∗, $\xi_\perp^p$; ——, KM41 model; - - - -, KM62 model; — · —, β model; and ·····, She-Leveque model. (b) Behaviours of the intermittency exponent along x computed according to two different methods: ——, based on $\langle \epsilon(\boldsymbol{x}+\boldsymbol{r})\epsilon(\boldsymbol{x})\rangle/\langle\epsilon\rangle^2 \sim (L/r)^\mu$; and ·····, $\mu = 2 - \xi_\parallel^6$.

et al. [44]. The μ exponent is calculated directly from the slope of the correlation coefficient obtained by dividing the autocorrelation of dissipation by $\langle\epsilon\rangle^2$ for separations in the inertial range; see figure 2.27. A second possible way to obtain μ is by using the expression relating the longitudinal sixth-order moment to the autocorrelation of dissipation [44]:

$$\frac{\langle(\delta u_\parallel)^6\rangle}{r^2} \sim \langle \epsilon(\boldsymbol{x}+\boldsymbol{r})\epsilon(\boldsymbol{x})\rangle. \tag{2.29}$$

The two quantities are reported in figure 2.26(b). As the reference value reported in many studies for the intermittency exponent is $\mu = 0.25 \pm 0.05$, which is deemed to be valid for high-Reynolds-number flows [102], the values calculated here suggest that the effect generated by intermittent structures on small-scale turbulence in the moderate-Reynolds-number range is less intense than at high Reynolds numbers. It is noticed that the method based on sixth-order structure functions, equation (2.29), displays a decay in the x-direction that is not expected nor recovered in the calculation of μ directly from the definition (2.27).

The decorrelation scale $\widetilde{r}$ is defined as the length of decorrelation of the instantaneous dissipation ϵ, i.e. the separation scale r where $\langle \epsilon(\boldsymbol{x}+\boldsymbol{r})\epsilon(\boldsymbol{x})\rangle/\langle\epsilon\rangle^2$ becomes unitary with a 1% error. In figure 2.28 the development of $\widetilde{r}$ along x is compared to that of the integral scale L. The decorrelation scale can be considered as a very large length scale, which in homogeneous isotropic turbulence depends on the Reynolds number and the intermittency characteristics of the flow.

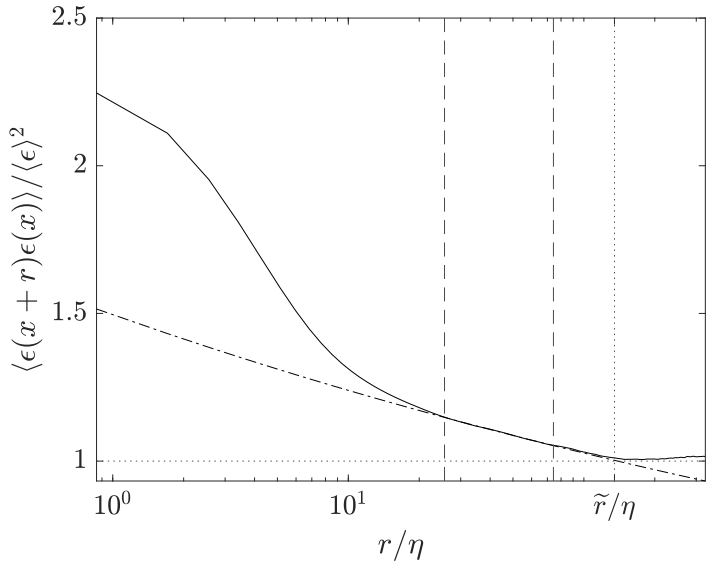

Figure 2.27. Dissipation correlation coefficient at $x = 25$: ——, $\langle\epsilon(\boldsymbol{x}+\boldsymbol{r})\epsilon(\boldsymbol{x})\rangle/\langle\epsilon\rangle^2$ as calculated from its definition; and — · —, $a_d(r/\eta)^d$, where $a_d = 1.07$ and $d = -0.082$. The dashed lines delimit the interval used for the power-law fitting procedure, $25\eta < r < 75\eta$, and the dotted lines demarcate the decorrelation scale $\widetilde{r}$.

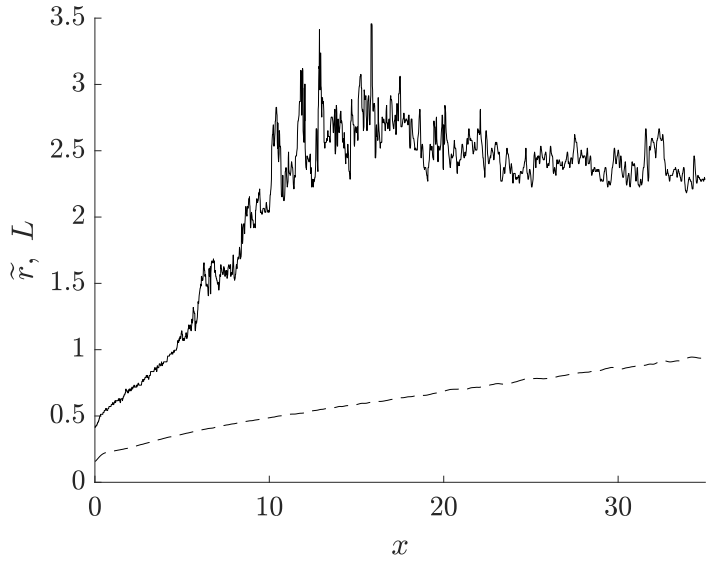

Figure 2.28. Streamwise evolution of the decorrelation scale in comparison with the integral scale: ——, $\widetilde{r}$; and - - - -, L. For $x = 25$, $\widetilde{r}/\eta = 135$ and $L/\eta = 45$.

2.3.11 Turbulent energy budgets

The equation governing the transport of $\langle k \rangle$ in a statistically steady case can be written in symbols as

$$-\mathcal{A}^k = \mathcal{T}_p^k + \mathcal{T}_t^k + \mathcal{D}_v^k + \mathcal{P}^k - \langle \widetilde{\epsilon} \rangle^k, \tag{2.30}$$

where $\mathcal{A}^k$ is the contribution by mean advection and $\mathcal{T}_p^k$, $\mathcal{T}_t^k$ and $\mathcal{D}_v^k$ represent pressure, turbulent and diffusive transports; $\mathcal{P}^k$ and $\langle \widetilde{\epsilon} \rangle$ stand for the production and pseudo-dissipation rate of turbulent kinetic energy. These terms are defined as follows,

$$\mathcal{A}^k = -\langle U_j \rangle \frac{\partial \langle k \rangle}{\partial x_j}, \tag{2.31}$$

$$\mathcal{T}_p^k = -\frac{1}{\rho} \frac{\partial \langle u_j p \rangle}{\partial x_j}, \tag{2.32}$$

$$\mathcal{T}_t^k = -\frac{1}{2} \frac{\partial \langle u_i u_i u_j \rangle}{\partial x_j}, \tag{2.33}$$

$$\mathcal{D}_v^k = \frac{1}{Re_{d_p}} \frac{\partial^2 \langle k \rangle}{\partial x_j \partial x_j}, \tag{2.34}$$

$$\mathcal{P}^k = -\langle u_i u_j \rangle \frac{\partial \langle U_i \rangle}{\partial x_j}, \tag{2.35}$$

$$\langle \widetilde{\epsilon} \rangle^k = \frac{1}{Re_{d_p}} \left\langle \frac{\partial u_i}{\partial x_j} \frac{\partial u_i}{\partial x_j} \right\rangle. \tag{2.36}$$

In grid-generated turbulence, where mean velocity gradients are zero and cross-flow directions y and z are homogeneous, the production term vanishes. In addition, for the Reynolds number computed here, the molecular contribution to transport is negligible. The resulting expression for the budget equation (2.30) thus becomes

$$\underbrace{\langle U \rangle \frac{d\langle k \rangle}{dx}}_{-\mathcal{A}^k} = \underbrace{-\frac{d\ \langle up \rangle}{dx}}_{\mathcal{T}_p^k} \underbrace{-\frac{d\ \langle uk \rangle}{dx}}_{\mathcal{T}_p^t} - \langle\, \widetilde{\epsilon}\, \rangle, \tag{2.37}$$

where the single terms are distributed along the x-axis as depicted in figure 2.29.

Two regions can be identified in figure 2.29: a near-field region where the three conservative terms redistribute the kinetic energy along x, and a far-field region where pressure and turbulent transports become negligible. Thus dissipation is solely balanced by turbulent kinetic energy advection; see figure 2.29(a) and its inset. A possible downstream boundary

for the near-field region can be set at $x = 2$, where the turbulent and pressure transports become 100 times smaller than advection and dissipation.

The near-field region can be subdivided into two subregions. By considering the ligament diameter d_f as the length scale, a region very close to the metal foam is identified for $x^*/d_f < 0.5$, where turbulent transport is larger than the advective one. This region is characterised by the sustainment of turbulence by means of fluctuations, which is counterbalanced by dissipation, as pressure and advective transports account for negligible shares. The second subregion extends for $0.5 < x^*/d_f < 14$, where turbulent kinetic energy is provided through pressure and advective mechanisms while dissipation and turbulent transport drain $\langle k \rangle$; see figure 2.29(a).

Data gathered by Norberg [95] indicate that the vortex formation length ℓ_f for the present Reynolds number based on the mean diameter of the filaments, $Re_{d_f} = 560$, lies in the range $1.5d_f < \ell_f < 2d_f$; see Bloor et al. [13] for other possible definitions of the vortex formation length. Figure 2.29(a) displays that this range matches the streamwise location where all the transport terms in equation (2.37) peak. Therefore, the present data suggest that kinetic energy is originated in the second part of the near-field region, where transport mechanisms show local peaks. Turbulent kinetic energy $\langle k \rangle$ is drained from here by the turbulent transport, which transfers turbulent fluctuations upstream, as indicated by the negative sign of the turbulent flux (see figure 2.29b) feeding the region very close to the metal foam. On the other hand, pressure and advective mechanisms are found to provide turbulent kinetic energy in the entire region $0.5 < x^*/d_f < 14$, and the signs of the relative fluxes indicate that turbulent kinetic energy is transferred downstream. At the coordinate $x^*/d_f = 14$ ($x = 2$), fluxes $\langle up \rangle$ and $\langle uk \rangle$ become constant in the streamwise direction, leading to the budget reported in equation (2.10) for $x > 2$, which is typical in developed decaying flows; see figure 2.29(a) and its inset, which reports the budget terms in the I_d region.

In order to separately assess the behaviour of streamwise and cross-flow velocity fluctuations, the transport equations for velocity variances are analysed. The budget of streamwise velocity variance reads

$$\underbrace{\langle U \rangle \frac{d\langle u^2 \rangle}{dx}}_{-\mathcal{A}^u} = \underbrace{-\frac{d\langle u^3 \rangle}{dx}}_{\mathcal{T}_t^u} \underbrace{-2\frac{d\langle u\,p \rangle}{dx}}_{\mathcal{T}_p^u} \underbrace{+2\left\langle p\frac{\partial u}{\partial x}\right\rangle}_{\mathcal{S}^u} - \langle \widetilde{\epsilon_u} \rangle, \tag{2.38}$$

where, from left to right, the first three terms, respectively, represent the advective, turbulent and pressure transports of $\langle u^2 \rangle$, $\langle p\,\partial u/\partial x \rangle$ is the pressure strain term and $\widetilde{\epsilon_u}$ stands for the u-variance pseudo-dissipation rate, $\widetilde{\epsilon_u} = 2\left((\partial u/\partial x_j)(\partial u/\partial x_j)\right)/Re_{d_p}$. The diffusive transport is again neglected with respect to the other terms. An equation similar to (2.38) can be

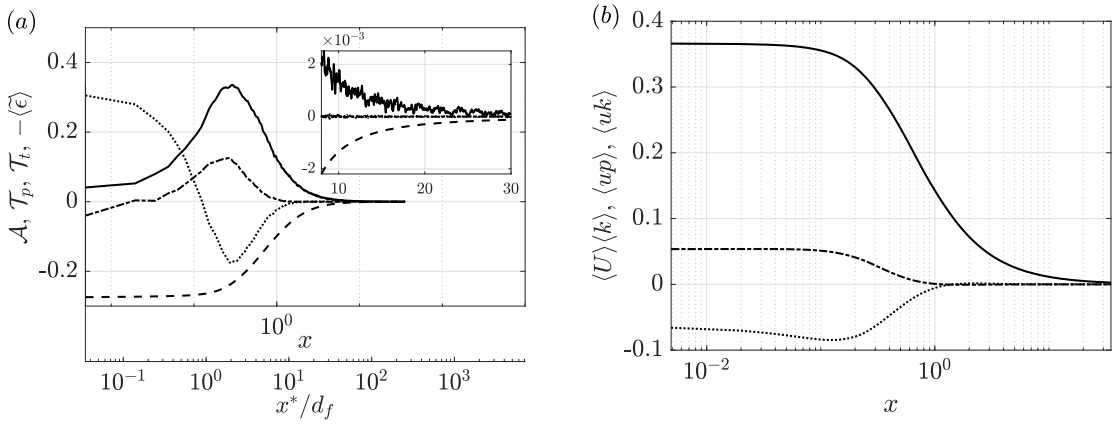

Figure 2.29. Turbulent kinetic energy along the streamwise direction in logarithmic plots. In panel (a) budget terms are reported: ——, $\mathcal{A}$; — · —, $\mathcal{T}_p$; · · · · · ·, $\mathcal{T}_t$; and - - - -, $-\langle\widetilde{\epsilon}\rangle$. Panel ($b$) presents turbulent kinetic energy fluxes: ——, $\langle U\rangle\langle k\rangle$; — · —, $\langle u\,p\rangle$; and · · · · · ·, $\langle u\,k\rangle$. The inset in (a) displays an enlargement of the budget terms in the range I_d in linear scale.

derived for the transverse velocity components, v and w, and becomes

$$\underbrace{\langle U\rangle\,\frac{d\langle v^2\rangle}{dx}}_{-\mathcal{A}^v} = \underbrace{-\frac{d\,\langle u\,v^2\rangle}{dx}}_{\mathcal{T}_t^v} \underbrace{+2\,\left\langle p\,\frac{\partial v}{\partial y}\right\rangle}_{\mathcal{S}^v} - \langle\widetilde{\epsilon_v}\rangle, \tag{2.39}$$

where the terms have the same interpretation as in equation (2.38), and the pseudo-dissipation rate of the v-variance is computed as $\widetilde{\epsilon_v} = 2\left((\partial v/\partial x_j)(\partial v/\partial x_j)\right)/Re_{d_p}$. Note that, with respect to equation (2.37), budgets of velocity component variances include the pressure strain terms. As it will be shown in the following, the role of these terms is to redistribute kinetic energy among the velocity components and thus it is responsible for the "return to isotropy" in homogeneous turbulence. Such a phenomenon has been studied for several decades as it is involved in second-order turbulence models; see, for example, the works by Rotta [107] and Lumley and Newman [79]. Pressure strain terms are not included in equation (2.37) as their sum $\mathcal{S}^u + 2\mathcal{S}^v$ vanishes because of incompressibility.

Figures 2.30 and 2.31 show the velocity variance budgets and fluxes along the streamwise coordinate. It appears that transport mechanisms are more intense in the $\langle u^2\rangle$ budget with respect to $\langle v^2\rangle$, while dissipations $\langle\,\widetilde{\epsilon_u}\,\rangle$ and $\langle\widetilde{\epsilon_v}\rangle$ are almost equal. The behaviour of the pressure strain terms reveals that turbulent energy is drained from the streamwise velocity fluctuations, as $\mathcal{S}^u$ represents a sink term in the $\langle u^2\rangle$ budget, and provided to cross-flow velocity fluctuations, where $\mathcal{S}^v$ acts as a source; see figures 2.30(a) and 2.31(a). The role of $\mathcal{S}^u$ and $\mathcal{S}^v$ does not change along the whole streamwise extension of the domain, as shown by the insets in figures 2.30(a) and 2.31(a). This occurs because, as reported in section § 2.3.2, flow anisotropy is conserved in the flow domain considered. In the decaying region I_d, the pressure strain terms maintain an intensity comparable to the advective and dissipation

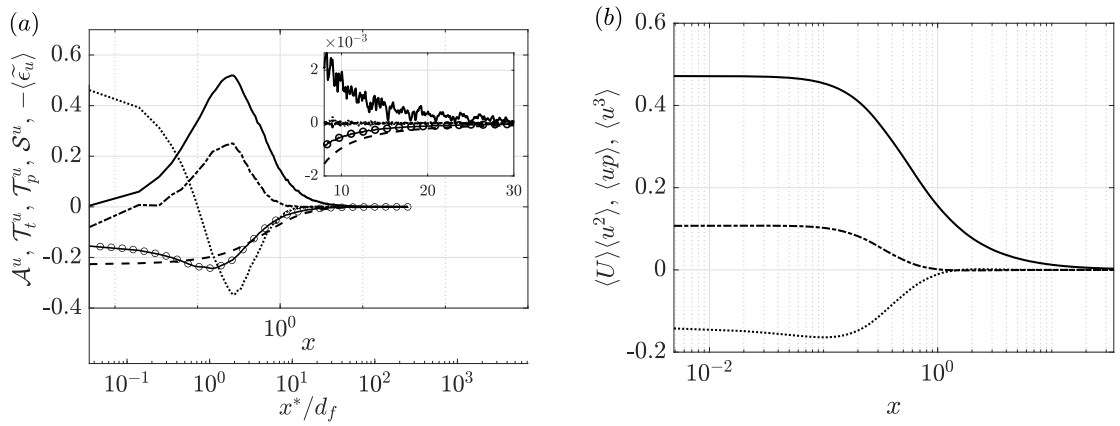

Figure 2.30. Variance of streamwise velocity component along the streamwise direction in logarithmic plots. In panel (a) budget terms are reported: ——, $\mathcal{A}^u$; · · · · · ·, $\mathcal{T}_t^u$; — · —, $\mathcal{T}_p^u$; —o—, $\mathcal{S}^u$; and - - - -, $-\langle\widetilde{\epsilon_u}\rangle$. Panel ($b$) presents $\langle u^2\rangle$ fluxes: ——, $\langle U\rangle\langle u^2\rangle$; — · —, $\langle u\,p\rangle$; and · · · · · ·, $\langle u^3\rangle$. The inset in (a) displays an enlargement of the budget terms in the range I_d in linear scale.

terms, suggesting that the isotropic condition, if any, would have been reached in a longer computational domain.

The profiles in figures 2.30 and 2.31 show that the u-variance terms behave very similarly to the budgets and fluxes of turbulent kinetic energy reported in figure 2.29. In particular, the peaks of turbulent, advective and pressure transports are located at the same distance from the metal foam, comparable to the vortex formation length. This suggests that velocity fluctuations are more intensely triggered along the streamwise direction with respect to the transverse ones. On the other hand, the v-variance terms peak slightly downstream with respect to terms in the $\langle u^2\rangle$ and $\langle k\rangle$ budgets, and the negative peak of turbulent transport is not very intense (see figure 2.31a), but it drains enough energy to sustain cross-flow fluctuations in the region just downstream of the metal foam. Another difference with respect to the $\langle u^2\rangle$ terms is the positive - yet not that intense - turbulent flux very close to the metal foam, indicating that cross-flow fluctuations are more correlated with positive u-fluctuations in this region (see figure 2.31b).

2.4 Conclusions

An analysis is presented of the turbulent flow behind a synthetic metal foam layer of thickness equal to five times the mean pore diameter. Unlike classical grid turbulence geometries, the metal foam ligaments are variably oriented, unevenly spaced and in general less ordered. Similar to classical grids, metal foams are mainly characterised by two length scales i.e. the pore diameter and the ligament thickness. The analysis encompasses one single Reynolds

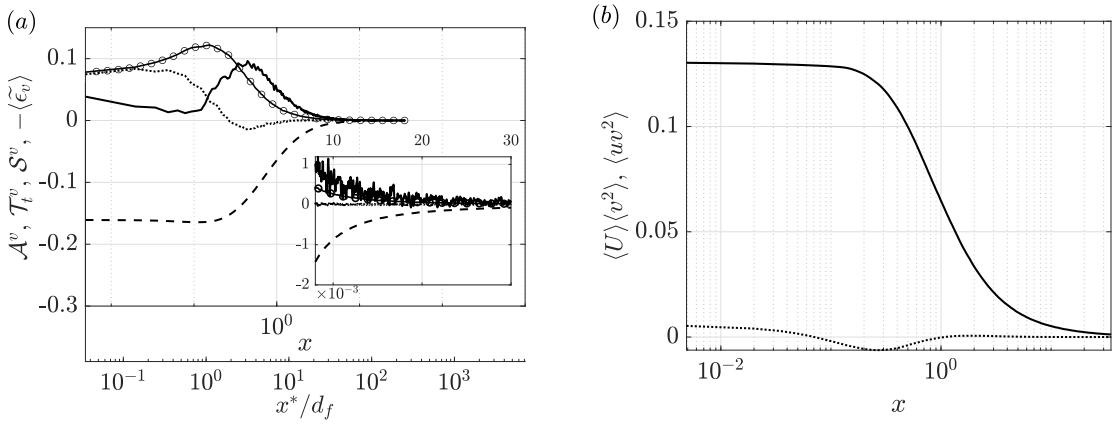

Figure 2.31. Variance of cross-flow velocity component along the streamwise direction in logarithmic plots. In panel (a) budget terms are reported: ——, $\mathcal{A}^v$; · · · · · ·, $\mathcal{T}_t^v$; —o—, $\mathcal{S}^v$; and - - - -, $-\langle\widetilde{\epsilon_v}\rangle$. Panel ($b$) presents $\langle v^2\rangle$ fluxes: ——, $\langle U\rangle\langle v^2\rangle$; and · · · · · ·, $\langle u\, v^2\rangle$. The inset in (a) displays an enlargement of the budget terms in the range I_d in linear scale.

number $Re_{d_p} = 4000$ and $\varepsilon = 0.92$ but the effect of a different porosity ($\varepsilon = 0.97$) on selected quantities is addressed in appendix A.

The analysis of the turbulent kinetic energy budget suggests that turbulence is triggered in the region close to the metal foam, approximately at a distance equal to the vortex formation length indicated by Norberg [95], $x^*/d_f \approx 2$. In the near-field region, $x < 2$, turbulent kinetic energy is distributed by transport mechanisms; the turbulent transport moves $\langle k\rangle$ upstream, sustaining fluctuations in close proximity to the metal foam, while pressure and advective transports provide velocity fluctuations to larger x-coordinates. At $x = 2$, pressure and turbulent transports are found to be negligible with respect to the other terms, entailing for $x > 2$ the expected behaviour of grid turbulence, where viscous dissipation is balanced by the mean advection of $\langle k\rangle$. Budgets of streamwise and cross-flow velocity variances indicate that fluctuations along x are the most intensely triggered and pressure strain terms act to redistribute turbulent energy towards the isotropic condition, which however is not observed due to the limited domain extension.

In that same near-field region, Re_λ decreases steeply and the dissipation rate coefficient C_ϵ approximates $C_\epsilon \propto Re_\lambda^{-1}$ while L/λ remains almost constant. These observations, in conjunction with the typical $-5/3$ slope in the turbulent power spectra, represent a typical behaviour already observed in the literature [119]. Given that this occurs very close to the porous matrix, where the hypotheses for the Richardson cascade are not verified, a considerable variation in C_ϵ is not interpreted here as an anomalous behaviour.

The developed region is defined here as the region where u_{rms} decays following a power law and starts at $x_{\min} = 7.98$. Besides $\langle k\rangle$, a number of relevant quantities, like the integral length scale, the Taylor microscale and the Kolmogorov scale of the flow, are observed to follow a power-law behaviour. The exponents obtained from a least-square fit are in many

cases very close to values predicted and measured in classical grid turbulence experiments. Given $n_k = 1.14$ and $q = 0.52$ (where n_k and q are the exponents of the power laws for $\langle k \rangle$ and L), the constancy of $u_{\mathrm{rms}}^2 L^3$ does not hold in the developed region simulated here, and thus the turbulence does not follow the theory by Saffman.

Structure functions of different orders are calculated at a fixed position $x = 25$ in the fully developed region. The extended self-similarity is used to calculate the scaling exponents. The results are interpreted in the light of the refined similarity hypothesis. The intermittency exponent μ computed directly from its definition is seen to behave uniformly within the computational domain. It reveals that intermittency is not very intense at the moderate Reynolds number of this study. The decorrelation length of dissipation $\widetilde{r}$ is larger than the integral scale. It depends on the Reynolds number as well as the intermittency characteristics of the flow.

Chapter 3

The aerodynamics of a rectangular cylinder

3.1 Introduction

The turbulent flow over elongated bluff bodies with sharp corners is of practical interest both in civil engineering [84], for the case of tall buildings and suspended bridge decks and in the aerodynamics of some ground vehicles [14], such as trucks and freight trains. A peculiarity of the aerodynamics of elongated bluff bodies lies in the fact that the flow exhibits large-scale separation at the leading edge and a subsequent reattachment before the final separation at the trailing edge. While a shedding instability in the wake characterizes all bluff bodies, only bluff bodies with a moderate chord-to-thickness ratio ($3 < c/D < 7$) display second order instabilities to be ascribed to the reattachment of the leading-edge shear layer, which in turn lead to the formation of an additional shedding of large-scale vortices from the recirculating region. The interaction mechanisms between this large-scale unsteadiness and turbulence are at the basis of very complex phenomena which both experiments and numerical simulations appear to be unable to tackle in an unequivocal way [19].

Aiming at establishing reliable standards for the simulation and measurements of separating and reattaching flows, an important collaborative activity on the aerodynamics of rectangular bodies with chord-to-thickness ratio $c/D = 5$ has been launched in 2008 by the Italian National Association for Wind Engineering (ANIV) in collaboration with the European Research Community On Flow, Turbulence And Combustion (ERCOFTAC). The benchmark is known by the acronym BARC (Benchmark on the Aerodynamics of a Rectangular 5:1 Cylinder)[8]. Within this framework, a numerous series of experiments and simulations have been conducted [18, 80, 109, 83, 104, 28, 90]. An exhaustive collection of the main results achieved after the first four years of activity is presented in Bruno et al. [19]. In this review a good agreement is found between wind tunnel measurements and numerical predictions of near wake flow, base pressure and drag coefficient. Conversely, a significant dispersion of the

results emerges with regard to the flow features along the cylinder lateral surfaces, such as lift and pressure distribution.

Among the many issues raised in the study of the aerodynamics of BARC geometry there is the dependence on the Reynolds number [80, 109, 91]. It is well known that the Reynolds number could strongly affect the flow topology and the vortex shedding instability of bluff bodies. In the case of circular cylinder, the Reynolds number has a key role because of changes of the separation point position along the rounded continuous surface [106, 12]. This does not hold true for rectangular cylinders, where the location of flow separation is fixed at the sharp edges. For these geometries the sensitivity to the Reynolds number is primarily related to variations in the formation and shape of the separation bubble [96]. With regards to the rectangular cylinder with $c/D = 5$, an important contribution is provided by the wind tunnel measurements by Schewe [109], who investigated the Reynolds-number range between 4000 and 400 000. Schewe [109] found that the main global aerodynamic parameters slightly change as a function of the Reynolds number for null flow incidence, with the only exception of the Strouhal number which shows a quick change for values below about 10 000. If non-zero angles of attack are considered (angles up to 6° were tested), also the mean lift coefficient exhibits a clear Reynolds-number dependence. The Reynolds-number effects observed by Schewe [109] can be interpreted by the numerical simulations of Mannini et al. [80], based on a two-dimensional Unsteady Reynolds-Averaged Navier-Stokes (URANS) approach. The simulations reveal the dominant role played by the extent of the separation bubble on the side of the cylinder.

For the present flow configuration, an upstream trend of the time-averaged reattachment location is observed with increasing Reynolds number ($Re_D \gtrsim 10^4$). However, the nature of this dependence is still unclear. According to simulations by Mannini et al. [80] the Reynolds number induces significant variations of mean reattachment length, whereas a much weaker dependence emerges from the work by Moore et al. [91]. The effects of the Reynolds number on the reattachment of a free shear layer have also been documented for the backward-facing step flow [47, 5, 2] and the flow over a bluff flat plate [97]. In these flow cases, experimental investigations carried out for values of Reynolds numbers (based on the step height or half the plate thickness) ranging from the order 10^2 to 10^4 revealed the existence of various flow regimes characterized by different variations of the reattachment length with the Reynolds number. In the laminar regime of the flow ($Re \lesssim 10^3$), the reattachment length increases quite sharply and reaches a maximum; in the transitional regime ($10^3 \lesssim Re \lesssim 10^4$), the reattachment length by first decreases irregularly, then shows a sudden increase up to a constant level that characterizes the turbulent flow regime ($Re \gtrsim 10^4$).

In numerical studies about BARC flow configuration, the statistics of the flow exhibit a high sensitivity to the mesh resolution [17, 128], to the turbulence modelling approach [83, 30], to the boundary conditions such as free-stream velocity and turbulence level [80, 82, 81, 104] and to the sharpness of the leading-edge corner [105]. To mitigate the many sources of

uncertainty in these simulations, the obvious approach is to account for one source of error at the time. In this view, the Direct Numerical Simulation method can be considered a convenient starting point, as it is not affected by uncertainties from turbulence modelling but is still affected by the spatial resolution, the domain dimensions and the numerical method employed.

In the present work, results from DNSs of the flow around the rectangular cylinder with $c/D = 5$ over the range of Reynolds numbers between $Re_D = 3000$ and 14000 are presented. Besides representing further sets of data suitable for validation and comparisons, one of the main purposes of this study is to provide a better understanding of the sensitivity of the BARC geometry to variations of the Reynolds number. To the best of the author knowledge, within the benchmark activity, this represents the first work addressing the Reynolds-number issue for values of the order 10^4 and by using a numerical approach clear of turbulence models.

The results obtained for the lower Reynolds number, i.e. $Re_D = 3000$, are compared against two previous DNSs [27, 24], carried out at the same Reynolds number but with different numerical approaches and computational mesh. This offers the opportunity to also provide a contribution to the discussion on the numerical representation of the BARC case. As opposed to more classical flows (turbulent boundary layers, channels, pipes and Rayleigh-Bénard convection to mention a few), where well-established settings for DNS are widely accepted, numerical guidelines for DNS of the flow around rectangular cylinders are lacking and this is also a first attempt to tackle this question.

3.2 Numerical procedure

3.2.1 Computational domain and simulation parameters

Three DNSs of the flow around the rectangular cylinder with $c/D = 5$ are performed at three different Reynolds numbers, i.e. $Re_D = 3000$, 8000 and 14000. The flow configuration used in the simulations is outlined in figure 3.1. The Cartesian coordinate system has origin at the centre of the leading edge of the cylinder top surface, y and z are the vertical and spanwise directions, respectively. The computational domain dimensions are $(L_x, L_y, L_z) = (80, 31, 5)$ and the streamwise position of the rectangular cylinder is at 20 from the inlet, see again the sketch in figure 3.1. Spatial discretisation is performed on hexahedral structured grids composed by spectral elements of order $N = 7$. The total degrees of freedom per time-step and per unknown for the flow case at $Re_D = 3000$ are almost 178 million, and increase up to over 3 billion for the flow case at $Re_D = 14000$. While the spectral elements are uniformly distributed along the homogeneous spanwise direction z, the mesh is refined at solid walls making use of geometric progressions along the streamwise and vertical directions. The number of elements on the horizontal surface of the rectangular cylinder is $E_x = 50$ and $E_z = 45$ for the flow case at $Re_D = 3000$, $E_x = 115$ and $E_z = 100$ at $Re_D = 8000$ and

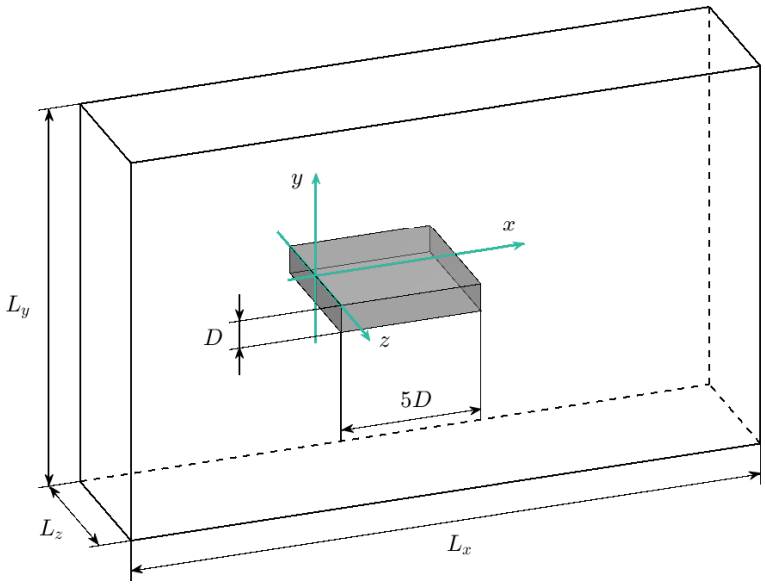

Figure 3.1. Scheme of the computational domain used in the simulations.

$E_x = 140$ and $E_z = 100$ at $Re_D = 14000$. More details about the distribution of elements are given in the next section 3.3.5. The time-step is kept fixed during the simulation to ensure that condition $CFL < 0.5$ is achieved everywhere. This condition is satisfied by setting $\Delta t = 5.5 \times 10^{-4}$, 3×10^{-4} and 2.6×10^{-4} for the flow cases at $Re_D = 3000$, 8000 and 14000, respectively. These values of Δt are found to be significantly smaller than the smallest Kolmogorov time scale, as an example $\tau_\eta \geq 0.007$ for $Re_D = 14000$. The computation of statistics is performed over a collection of at least 51 three-dimensional fields gathered after the statistically steady conditions are reached at equal time intervals $\Delta T = 5$. For the flow case at $Re_D = 3000$, statistics are computed over a period of 290 time units. To obtain well-converged statistics, averages are also taken by availing of spatial homogeneity along the spanwise direction and statistical symmetry of the flow along the vertical direction [27]. The statistical convergence of the databases is then verified by comparing the obtained flow statistics with those obtained using a portion of the total samples. A good agreement is found. Similar numerical settings are employed in Trias et al. [117], Alves Portela et al. [3], and Cao et al. [23], where the configuration of a square cylinder is considered.

3.2.2 Previous DNS studies

As far as the author knows, the only numerical investigations about the BARC flow case using an approach clear of turbulence models are the DNSs by Cimarelli et al. [27] and Chiarini and Quadrio [24], at a Reynolds number of $Re_D = 3000$. These simulations will

be taken as principal references in the comparison with the present results obtained at the same Reynolds number. With regards to the simulations at higher Reynolds numbers, since comparable DNS data are missing in the literature, results will be analysed in the light of available experimental measurements and numerical data based on RANS, DES, and LES approaches. In the simulation by Cimarelli et al. [27], the governing equations are discretized using the cell-centred finite volume method implemented in the OpenFOAM open-source code [125]. Time integration is performed by means of a second-order backward Euler implicit scheme while convective and diffusive fluxes at the volume faces are evaluated through a second-order central difference scheme. Further details on the numerical procedure can be found in Cimarelli et al. [27, 28]. In the recent work by Chiarini and Quadrio [24], an in-house code based on second-order Finite Differences for spatial discretisation and third-order Runge-Kutta scheme for temporal discretisation is used. In this case, an implicit second-order accurate immersed-boundary method is used to account for solid boundaries in the flow. Details of the numerical meshes employed in the present simulations are compared to Cimarelli et al. [27] and Chiarini and Quadrio [24] in table 3.1.

The present simulation at $Re_D = 3000$ and simulations by Cimarelli et al. [27] and Chiarini and Quadrio [24] differ because of domain size, time-step size, time-integration period, order of accuracy of the numerical schemes, spatial resolution of the schemes and grid spacings. As shown by Mariotti et al. [82], the blockage of the computational domain has a negligible effect on the flow statistics for ratios $D/L_y < 0.0375$. On the other hand, as suggested by Bruno et al. [19], the distance between the inlet boundary and the leading edge should be larger than 20. Both these criteria are satisfied by all the simulations. It is then assumed that the main differences in the solutions are not to be ascribed to the different computational domains. The smallest Kolmogorov time scale is of the order of $\tau_\eta \approx 0.02$. All simulations make use of a time-step at least one order of magnitude smaller than the Kolmogorov scale. As statistical convergence was checked in the simulations, it is assumed that the different time-steps and time-integration intervals do not have a significant role in the difference between solutions. From the heuristic reasoning above, it can be concluded that deviations of the present solution at $Re_D = 3000$ with respect to Cimarelli et al. [27] and Chiarini and Quadrio [24] are mostly due to the different spatial discretisation.

Spatial discretisation depends upon grid spacings in the three directions and the specific features of the spatial schemes employed. The spectral element method is high order accurate in space, features good resolution characteristics and is less dissipative and dispersive with respect to the second order Finite Volume and Finite Difference approaches. In addition to this aspect, a marked difference in the number of degrees of freedom per time level employed by the present simulation and the simulation in Cimarelli et al. [27] exists (178 million degrees of freedom and 15, respectively, see table 3.1). Hence, the present simulation at $Re_D = 3000$ is to be regarded as better resolved in space with respect to the simulation in Cimarelli et al. [27]. The comparison between spatial resolution of the present simulation and the simulation

Table 3.1. Details of the mesh characteristics and mean flow configuration at $Re_D = 3000$, 8000 and 14000. Data from previous DNS simulations are also included for comparison. In the first column n_x, n_y and n_z are the number of grid points or degrees of freedom along the three directions in the region above the rectangular cylinder; x_r is the reattachment length; (x_c, y_c) are the coordinates of the vortex center; x_s is the coordinate of the start of the secondary vortex; and x_e indicates the coordinates of the end of the secondary vortex and the wake vortex.

	Present			Cimarelli et al. [27]	Chiarini and Quadrio [24]
Re_D	3000	8000	14000	3000	3000
$L_x \times L_y \times L_z$	$80 \times 31 \times 5$	$80 \times 31 \times 5$	$80 \times 31 \times 5$	$112 \times 50 \times 5$	$62.5 \times 42 \times 5$
$n_x \times n_y \times n_z$	$351 \times 197 \times 316$	$806 \times 428 \times 701$	$981 \times 568 \times 701$	$128 \times 122 \times 144$	$892 \times 363 \times 150$
Spatial DoF	177 819 705	1 948 812 600	3 084 343 500	$\sim 15\,000\,000$	250 948 800
Primary vortex					
x_r	4.17	4.25	4.39	3.65	3.955
(x_c, y_c)	$(2.67, 0.33)$	$(2.04, 0.32)$	$(2.17, 0.33)$	$(2.04, 0.35)$	$(2.36, 0.33)$
Secondary vortex					
x_s	1.14	0.11	0.06	0.4	0.63
x_e	1.93	1.03	0.72	1.4	1.59
x_r	0.79	0.92	0.66	1.0	0.96
(x_c, y_c)	$(1.57, 0.037)$	$(0.38, 0.050)$	$(0.26, 0.052)$	–	$(1.2, 0.041)$
Wake vortex					
x_e	5.88	5.91	5.80	6.2	5.975
(x_c, y_c)	$(5.38, -0.25)$	$(5.34, -0.24)$	$(5.30, -0.26)$	$(5.5, -0.27)$	$(5.415, -0.25)$

by Chiarini and Quadrio [24] is instead more difficult. This is due to the observation that the mesh density is similar, despite a different distribution along the directions, but the resolution characteristics and the overall quality of the spatial representation might be better in the present simulation, which employs a high order, spectral element method. Furthermore, when judging the quality of the discretisation it should be considered that as the immersed boundary method in conjunction with a structured mesh is employed in Chiarini and Quadrio [24], not all the computational points participate to the spatial accuracy in the regions of high gradients and a number of them are idle in the solid region. Accordingly, it might be reasonably inferred that the DNS by Chiarini and Quadrio [24] features intermediate spatial resolution characteristics, between Cimarelli et al. [27] (low resolution) and the present DNS (high spatial resolution). Additional care should be taken in the comparison between the present simulation at $Re_d = 3000$ and the simulation by Chiarini and Quadrio [24] given the considerable difference in the period used for statistics collection in the two cases, which corresponds to $290D/U_\infty$ in the present case and $2345D/U_\infty$ in Chiarini and Quadrio [24].

3.3 Results

3.3.1 Instantaneous flow field

An introduction to the main physical features of the separating and reattaching flow around the rectangular cylinder with $c/D = 5$ is provided by analysing the dominant vortical structures populating the instantaneous fields for different flow conditions [28, 24]. The detection of the vortical structures is performed using the λ_2-definition of vortex by Jeong and Hussain [59], based on negative regions of the second largest eigenvalue λ_2 of the tensor $S_{ik}S_{kj} + \Omega_{ik}\Omega_{kj}$, where

$$S_{ij} \equiv \frac{1}{2}\left(\frac{\partial U_i}{\partial x_j} + \frac{\partial U_j}{\partial x_i}\right) \quad \text{and} \quad \Omega_{ij} \equiv \frac{1}{2}\left(\frac{\partial U_i}{\partial x_j} - \frac{\partial U_j}{\partial x_i}\right) \tag{3.1}$$

are the symmetric and antisymmetric parts of the velocity gradient tensor. This represents a well-established and validated technique to educe fully three-dimensional vortical structures in both free- and wall-bounded turbulent shear flows [60].

Flow at $\boldsymbol{Re}_D = 3000$

Figure 3.2 shows three-dimensional visualizations of the isosurfaces of $\lambda_2 = -2$ around the rectangular cylinder at $Re_D = 3000$. The sharp corner at the leading edge triggers the flow separation and a separated shear layer develops along the sides of the bluff body. This separation is dictated by the bluff body geometry (fixed point of separation) and does not occur as a result of viscous effects in an adverse pressure gradient (viscous separation). At the early stage of the separation bubble, a laminar free shear layer occurs. This is associated

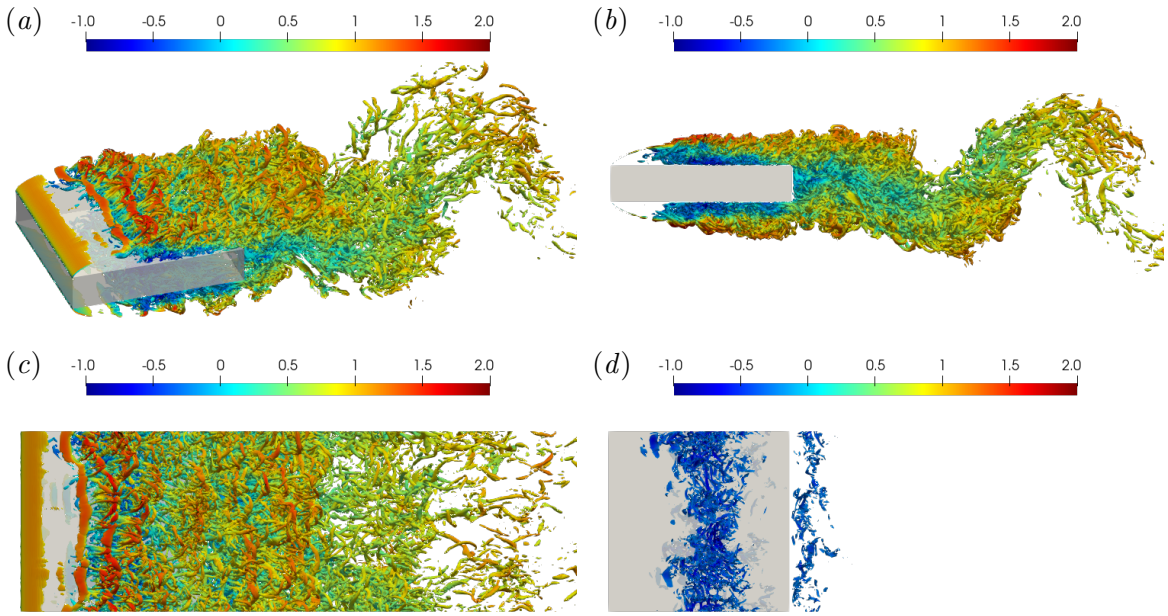

Figure 3.2. Instantaneous three-dimensional views of the flow case at $Re_D = 3000$. Isosurfaces of $\lambda_2 = -2$ coloured with streamwise velocity. (a) General view , (b) side view and (c) top view. (d) Isosurfaces of $\lambda_2 = -2$ with negative streamwise velocity, $U < -0.2$, to highlight the vortical structures in the reverse flow region.

with the generation of two-dimensional spanwise vortices, see the coherent sheet of vortical motions in panels of figure 3.2. In a second stage, the shear layer becomes unstable due to the onset of Kelvin-Helmholtz instability mechanisms and large-scale spanwise rolls are shed downstream of the leading edge. Along the shear layer transitional processes take place. The initial spanwise structures undergo deformation because of the growing perturbations of the flow field, note the corrugations of the spanwise vortex cores in figure 3.2(c). This distortion process leads to the appearance of streamwise vorticity and subsequent transformation into three-dimensional vortical structures with hairpin-like shape [66, 55, 127]. These vortices are stretched while they are conveyed downstream towards the wake, until they eventually break up to small scale turbulent motions. From the instantaneous reattachment line on the wall, two boundary layers develops. One is directed upstream towards the leading edge, see the structures coloured with negative values of the streamwise velocity in figures 3.2(b,d), and the other is directed downstream towards the trailing edge. In the wake, vortical motions shed from the leading-edge shear layer and the trailing edge are involved in large-scale oscillatory motions resembling the Kármán vortex street, typical of separated flow over bluff bodies, see figure 3.2(b).

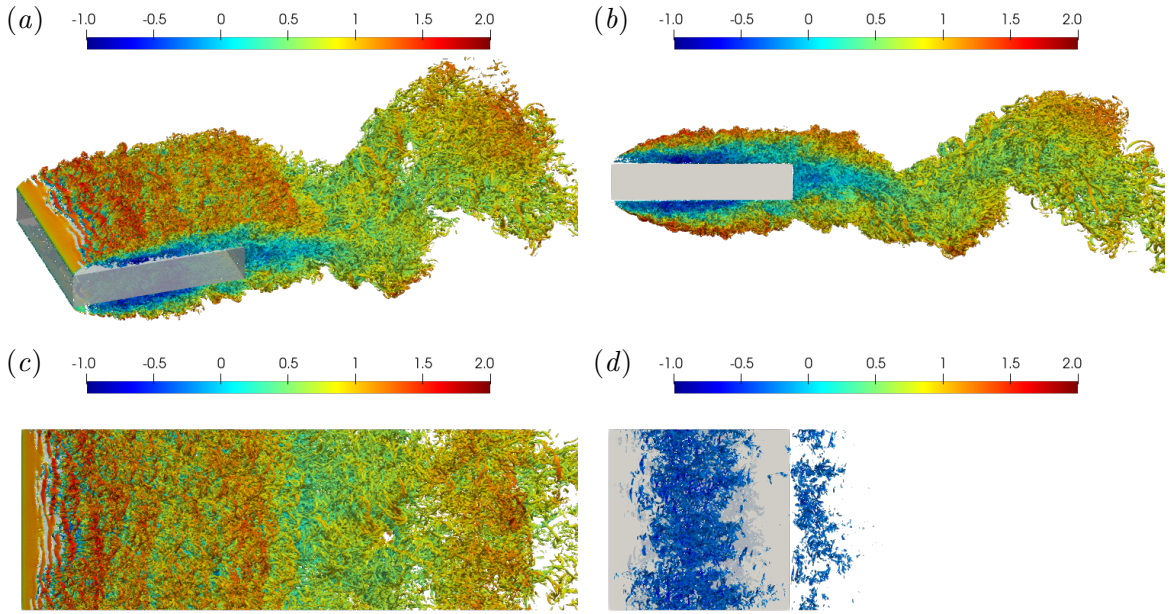

Figure 3.3. Instantaneous three-dimensional views of the flow case at $Re_D = 8000$. Isosurfaces of $\lambda_2 = -4$ coloured with streamwise velocity. (a) General view , (b) side view and (c) top view. (d) Isosurfaces of $\lambda_2 = -4$ with negative streamwise velocity, $U < -0.2$, in the top view.

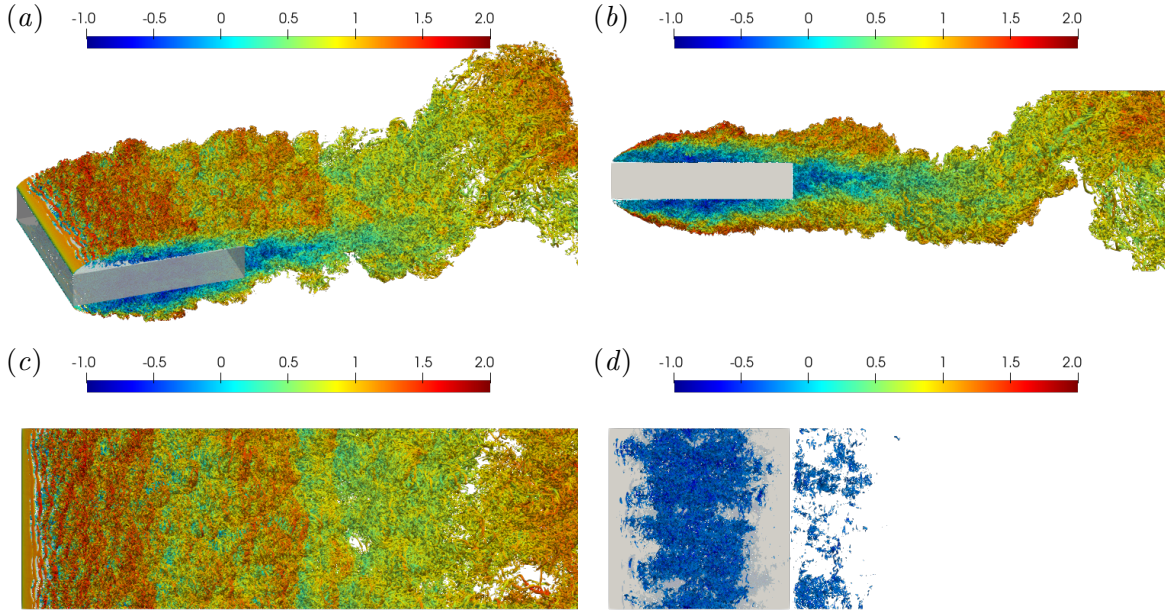

Figure 3.4. Instantaneous three-dimensional views of the flow case at $Re_D = 14000$. Isosurfaces of $\lambda_2 = -5$ coloured with streamwise velocity. (a) General view , (b) side view and (c) top view. (d) Isosurfaces of $\lambda_2 = -5$ with negative streamwise velocity, $U < -0.2$, in the top view.

Table 3.2. Summary of the mean global quantities evaluated for each of the flow cases considered, St is the vortex shedding Strouhal number.

Re_D	$\langle c_\mathrm{d} \rangle$	$\langle c_\mathrm{l} \rangle$	$c_{\mathrm{l,\ rms}}$	St
3000	0.950	−0.049	0.329	0.125
8000	0.995	−0.005	0.472	0.112
14000	1.038	−0.024	0.630	0.111

Flow at $Re_D = 8000$ and 14000

The main mechanisms driving the separation, reattachment and development of the flow remain almost unaltered for increasing Reynolds numbers, but significant differences can be identified as regards the characteristics of turbulent motions generated. Instantaneous flow realizations for the cases at $Re_D = 8000$ and 14000 are shown in figures 3.3 and 3.4, respectively. Vortical structures are defined by the isosurfaces of $\lambda_2 = -4$ at $Re_D = 8000$ and $\lambda_2 = -5$ at $Re_D = 14000$. The entire transitional process, from the leading-edge detachment of spanwise rolls to the evolution of hairpin-like vortices, takes place earlier and sooner than for the low-Reynolds-number case, which means that fully turbulent three-dimensional structures are achieved at lower distances from the separation point. In addition, the spanwise structures shed at the very first part of the shear layer become thinner as the Reynolds number increases. Further downstream, the flow around the rectangular cylinder is filled by turbulent structures spacing a wider range of scales, with the smaller scale which decreases with the Reynolds number.

3.3.2 Integral quantities and time scales of the flow

The statistical description of the flow starts with the analysis of the main integral quantities and the evaluation of the time scale characteristic of the unsteady processes occurring. For the BARC flow configuration, the integral quantities of interest are the drag and lift coefficients, c_d and c_l, which are the dimensionless force coefficients defined as follows [4],

$$c_\mathrm{d} \equiv \frac{F'_x}{\frac{1}{2}\rho U_\infty D} \quad \text{and} \quad c_\mathrm{l} \equiv \frac{F'_y}{\frac{1}{2}\rho U_\infty D}, \tag{3.2}$$

where F'_x and F'_y are the horizontal and vertical components of the aerodynamic force on the body per unit span. From the point of view of wind engineering applications, these coefficients are useful in the design phase for the prediction of aerodynamic loads on buildings and structures which resemble the rectangular shape here analysed.

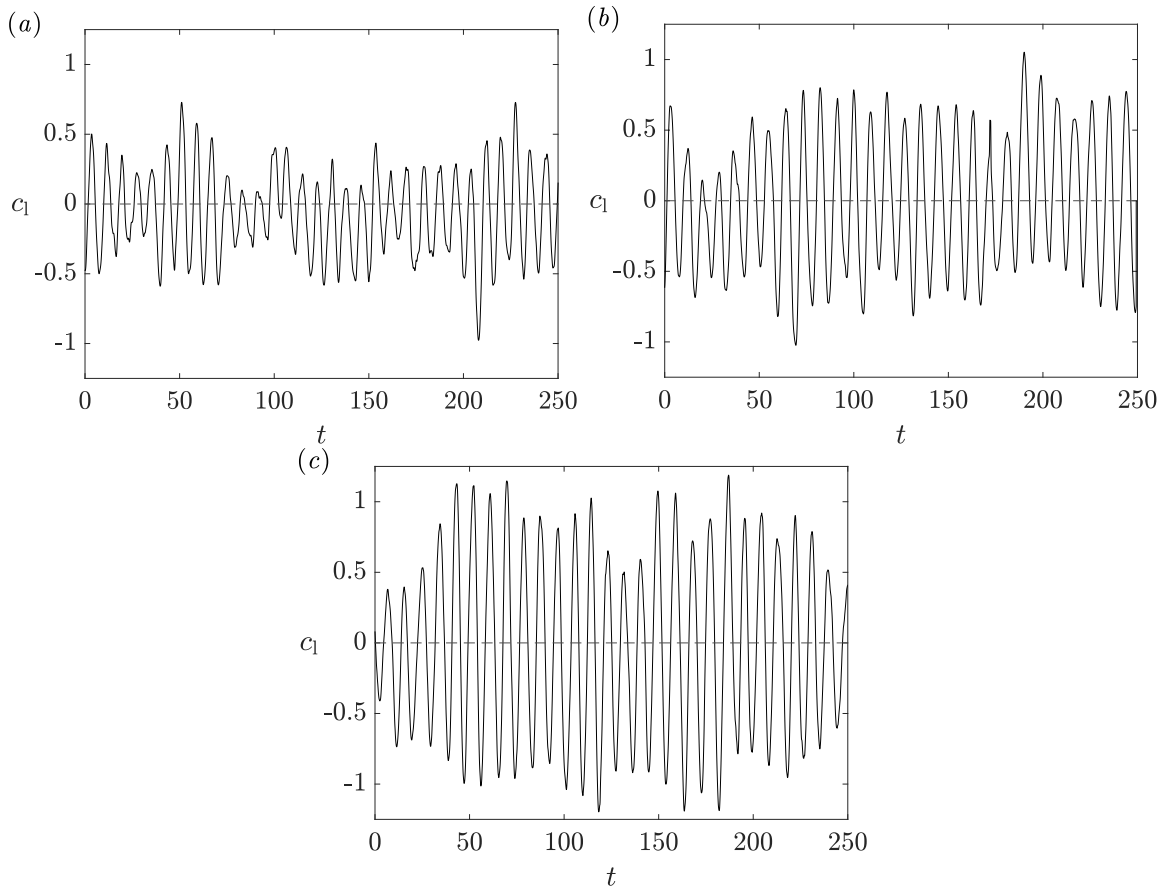

Figure 3.5. Lift coefficient as a function of time in the three flow cases simulated at $Re = 3000$ (a), 8000 (b) and 14000 (c).

Flow at $Re_D = 3000$

For bluff bodies the main source of aerodynamic drag is pressure, whereas the contribution given by shear stress is limited. The average drag coefficients $\langle c_\mathrm{d} \rangle$ computed for the flow case at $Re_D = 3000$ and for higher Reynolds numbers are listed in table 3.2. There is good agreement between the value measured here, $\langle c_\mathrm{d} \rangle = 0.950$, at $Re_D = 3000$ and the DNS data by Cimarelli et al. [27] and Chiarini and Quadrio [24] at the same Reynolds number, which provide $\langle c_\mathrm{d} \rangle = 0.96$ and 0.944, respectively.

The lift coefficient fluctuates in time around a mean value $\langle c_\mathrm{l} \rangle$ that is ideally equal to zero because of symmetry of the flow. However, the effective $\langle c_\mathrm{l} \rangle$ is usually found to slightly deviate from zero depending on the temporal window used for taking statistical averages. Here, the percent deviation from $\langle c_\mathrm{l} \rangle = 0$ is 5% for the flow case at $Re_D = 3000$ and less than 2.5% for the others. In figure 3.5 the temporal evolution of the lift coefficient for the three different cases is shown and in table 3.2 the root-mean-square values of lift fluctuations $c_{\mathrm{l,\,rms}}$ are reported. This latter parameter is known to be particularly sensitive to

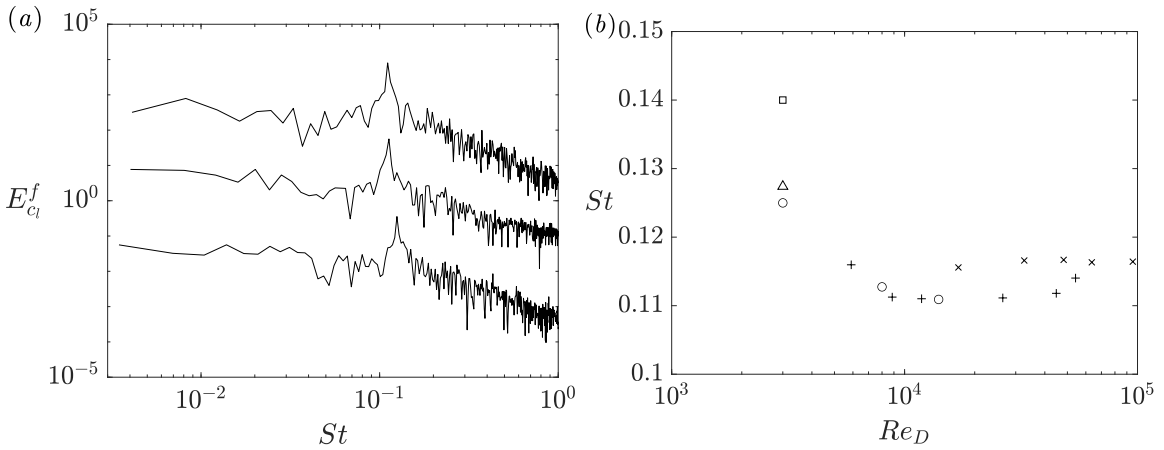

Figure 3.6. (a) Frequency spectra of the lift coefficient as a function of the Strouhal number for the different flow cases. The spectra are offset in the vertical direction with increments of two decades for visual clarity and arranged in ascending order of Re_D. (b) Variation of the vortex shedding Strouhal number with the Reynolds number: ◯, present data; □, DNS data from Cimarelli et al. [27]; △, DNS data from Chiarini and Quadrio [24]; +, WT data from Schewe [109]; and ×, WT data from Moore et al. [91].

the set-up of the simulation (numerical method, turbulence modelling, temporal and spatial discretisations), as evidenced by the large spread in the numerical predictions in the literature [19]. The reason lies in the difficulty of representing unequivocally the complex dynamics of the recirculating regions of the flow, especially when using numerical tools affected by turbulence modelling. Such problems should not affect the present DNS data, which provide $c_{\mathrm{l,\ rms}} = 0.329$. In the work by Chiarini and Quadrio [24], where a longer time integration is performed, $c_{\mathrm{l,\ rms}} = 0.289$ is obtained.

The time scales of the unsteady processes occurring in the flow are studied by evaluating the frequency spectra of the lift coefficient and cross-stream fluctuating velocity in different regions of the flow field. The frequency spectrum for the generic time signal $\beta(t)$ is obtained as

$$E^f_\beta(St) = \hat{\beta}\hat{\beta}^*, \tag{3.3}$$

where the hat symbol indicates the Fourier transform, the superscript * here denotes the complex conjugate and $St = fD/U_\infty$ is the dimensionless frequency, corresponding to the Strouhal number. The frequency spectra of the lift coefficient $E^f_{c_\mathrm{l}}$ are shown in figure 3.6(a) for the different values of Reynolds number simulated. A well-defined peak is observed in the low-frequency range. This peak is associated with the shedding of large-scale vortices from the main separation bubble [27] and is obtained for a dimensionless frequency of $St = 0.125$ for the flow case at $Re = 3000$. Vortex shedding frequencies for the rectangular cylinder generally fall in the range $0.105 < St < 0.132$ in wind tunnel experiments [96, 109, 94] and $0.087 < St < 0.16$ in numerical simulations [6, 83, 126]. The DNSs studies by Cimarelli et al.

Table 3.3. Probe positions (x, y) for the frequency and wavenumber spectra.

	Re_D		
Probe	3000	8000	14000
1	$(0.49, 0.32)$	$(0.30, 0.24)$	$(0.30, 0.25)$
2	$(0.91, 0.43)$	$(0.50, 0.33)$	$(0.50, 0.32)$
3	$(1.50, 0.53)$	$(0.90, 0.44)$	$(0.90, 0.42)$
4	$(3.95, 0.40)$	$(3.80, 0.40)$	$(3.80, 0.40)$
5	$(3.00, 0.08)$	$(3.00, 0.08)$	$(3.00, 0.06)$
6	$(1.50, 0.12)$	$(0.90, 0.15)$	$(0.90, 0.15)$
7	$(6.00, -0.20)$	$(6.00, -0.20)$	$(6.00, -0.20)$

[27] and Chiarini and Quadrio [24] provide $St = 0.14$ and 0.127, respectively. Figure 3.6(b) shows the present results together with those from previous DNSs and other works at different Reynolds number. The Strouhal numbers obtained are compatible with data in the literature and correspond to a mean period of lift oscillations of $8\,D/U_\infty$.

A secondary peak has been also observed by Cimarelli et al. [28] in connection to a very large-scale low-frequency unsteadiness existing on the top of the regular vortex shedding and associated with self-sustaining mechanisms of turbulence. They detect an additional local maximum in the spectrum of c_l at $St \approx 0.042$, which is one-third of the vortex-shedding frequency. In the spectra of figure 3.6(a), a secondary low-frequency peak is not detected. One could argue that this absence is due to the time interval of the simulation, which might be not long enough to catch many occurrences of the low-frequency event. However, the results by Chiarini and Quadrio [24] show that, even by using a much longer integration time, a low-frequency peak is still not visible.

The dominant time scales of the unsteady motions taking place along the leading-edge shear layer and in the wake are also analysed. To this aim, the frequency spectra of the vertical component of fluctuating velocity E_v^f are evaluated at three points along the shear layer in figure 3.7(a) and in the wake in figure 3.7(b). The coordinates in the x–y plane of the probes used in the present work are given in table 3.3. The same information about time scales can also be obtained from the frequency spectra of the streamwise velocity, which are not reported here for conciseness. The spectra evaluated along the shear layer exhibit a definite peak for a frequency that lies in the interval $0.91 < St < 1.17$. These peaks are associated with the time scales of the velocity fluctuations amplified in the transitional process throughout the shear layer. While moving downstream along the shear layer, the dominant frequency steadily decreases and a broad banded peak rises up. A similar behaviour is also found by Cimarelli et al. [27] and Chiarini and Quadrio [24], but for slightly different frequency intervals. For example, in the former work $0.9 < St < 1.8$ and in the latter $1.21 < St < 1.44$. Near the leading-edge, a second peak is recognised at lower frequencies, for $St = 0.123$. The Strouhal number of this peak matches the time scale of the vortex

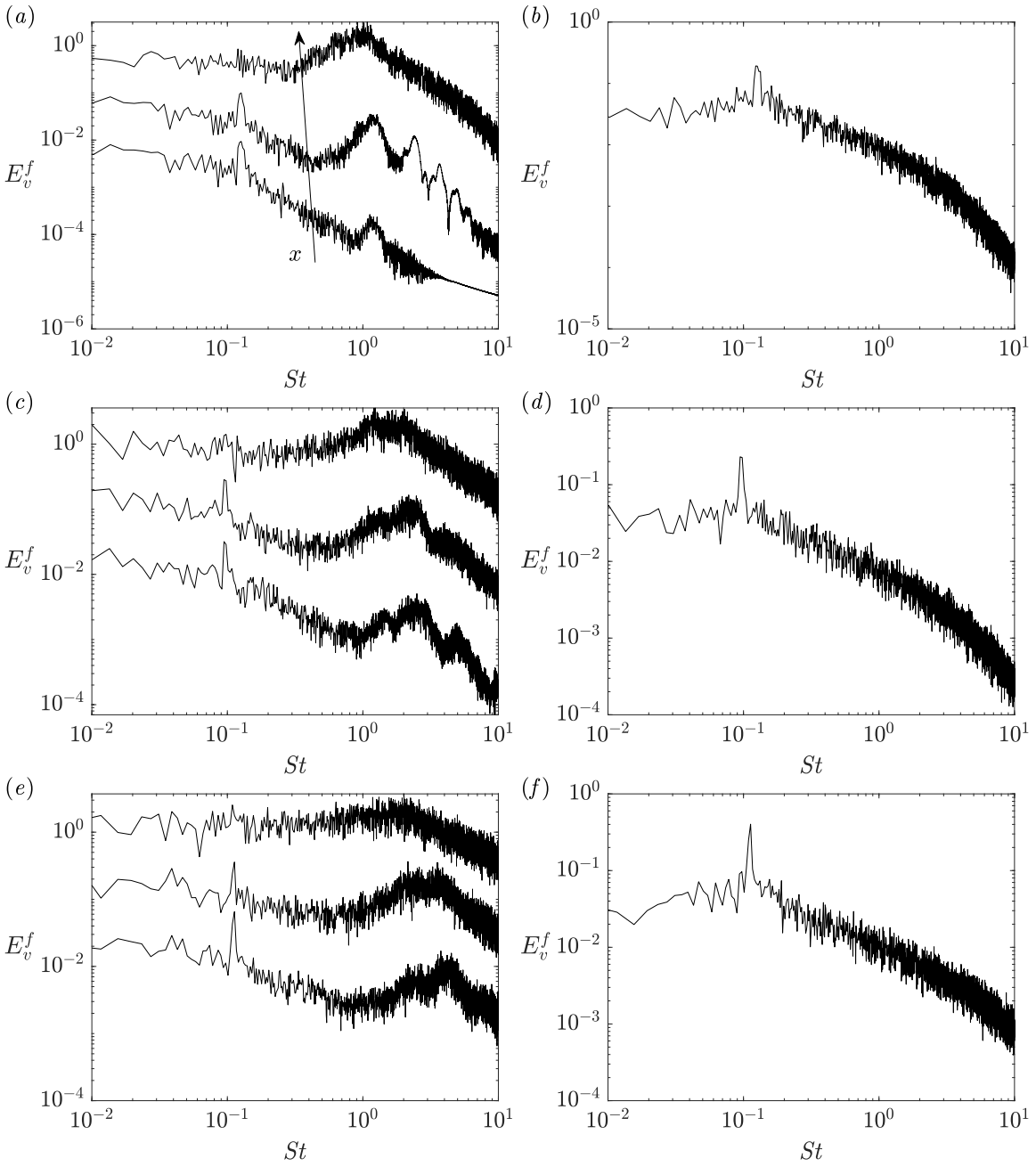

Figure 3.7. Frequency spectra of the vertical velocity obtained along the leading-edge shear layer at probes from 1 to 3 (left column) and in the wake at probe 7 (right column). The top panels report results for the flow case at $Re_D = 3000$, middle panels for the flow case at $Re_D = 8000$ and bottom panels for the flow case at $Re_D = 14000$. Spectra in the left column are offset in the vertical direction by increments of one decade for clarity and the arrow in panel (a) indicates the evolution for increasing streamwise distance x. Probe locations are displayed in figure 3.8(a) and is reported in table 3.3 for each of the flow cases simulated.

shedding from the main recirculating region, $St = 0.125$, thus suggesting that the vortex shedding affects the shear layer instability [55, 28]. The same frequency is identified also when evaluating the time scale of the large-scale oscillatory motions occurring in the wake of the cylinder. As shown in figure 3.7(b), the spectrum obtained in the wake has a single peak at $St = 0.123$.

Two primary modes of the unsteady motions are thus identified: a low-frequency mode associated with the detachment of large-scale vortices from the main separation region and in the wake, and a high-frequency mode dominating the instability mechanisms along the leading-edge shear layer and depending on space.

Flow at $Re_D = 8000$ and 14000

The same parameters discussed above are examined for the flow cases at $Re = 8000$ and 14000 to investigate the Reynolds number dependency. The mean drag coefficient increases with the Reynolds number up to $\langle c_\mathrm{d} \rangle \approx 1.04$, see values in table 3.2. The low-pressure levels near the base of the cylinder decreases steadily because of the formation of recirculating regions in the wake of increasing strength. Although direct comparisons are not available in the literature for the cases at higher Reynolds number, the values obtained for $\langle c_\mathrm{d} \rangle$ in most of the simulations and wind tunnel experiments within the benchmark activity are very close to 1 [19]. For example, Schewe [109] finds $\langle c_\mathrm{d} \rangle = 1.03$ at $Re_D = 2 \times 10^4$, and values ranging between 0.94 and 1.05 for $2 \times 10^4 < Re_D < 2 \times 10^6$.

The time history of the lift coefficient shows oscillations of wider amplitude with increasing Reynolds number. This is expressed quantitatively by the growth of $c_{\mathrm{l,\,rms}}$ values in table 3.2, indicative of the instantaneous imbalance between the two pressure regions induced by the separation bubbles which alternately shrink and enlarge on the top and bottom sides of the rectangle. However, at this stage of the work it is not clear whether the main source of this imbalance relies in different extensions of the low-pressure regions on the two sides (between enlarged and contracted configurations), or in variations of the pressure levels induced by the separated and reattached regions.

The period of lift oscillations is found to be slightly affected by the Reynolds number. As displayed in figure 3.6(b), the Strouhal number associated to the shedding of large-scale vortices slowly approaches $St = 0.11$ as the Reynolds number increases. In this regard, the wind tunnel (WT) tests by Schewe [109] and Moore et al. [91] point out a flattening in the variation of the Strouhal number for $Re_D > 6000$ at a value close to 0.11.

The frequency spectra E_v^f evaluated at the leading-edge shear layer and in the wake for the cases at higher Reynolds number are shown in figures 3.7(c,d,e,f). The low-frequency mode keeps almost constant at $St \approx 0.112$, whereas the high-frequency mode shifts towards smaller time scales with increasing Reynolds number. The high-frequency peaks are found for $1.4 < St < 2.9$ at $Re_D = 8000$ and for $2.0 < St < 4.4$ at $Re_D = 14000$. This behaviour

is consistent with the trend measured by Moore et al. [91], who found that the shear layer frequency normalized by the primary vortex shedding frequency scales with the Reynolds number as $St \sim Re_D^n$, where n is found to be slightly larger than 0.5 as for circular [12, 103] and square cylinders [76].

3.3.3 Mean flow topology and turbulent kinetic energy

The topology of the mean flow is firstly described with reference to the flow case at $Re_D = 3000$. Comparisons with the DNS data by Cimarelli et al. [27] and Chiarini and Quadrio [24] are also made, focusing on the different flow field representations provided by the use different numerical approaches and meshes. Then, results for higher Reynolds numbers are presented evidencing the main departures from the flow case at $Re_D = 3000$.

Flow at $\boldsymbol{Re}_D = 3000$

The flow around a rectangular cylinder with $c/D = 5$ is characterised by a variety of interacting phenomena that form a system of remarkable complexity. As shown by the streamlines of the mean velocity field in figure 3.8(a), the flow exhibits a large-scale separation at the leading-edge corner and a reattachment at the rectangle side. A region of intense flow recirculation, hereafter called primary vortex, is thus formed on average. The primary vortex is stretched along the streamwise direction and extends up to the reattachment point of the mean flow at $x_r = 4.17$. Its centre of rotation, here defined as the point within the recirculating region where the mean velocity vanishes, $\langle U \rangle = \langle V \rangle = 0$, is found at $(x_c^{pv}, y_c^{pv}) = (2.67, 0.33)$. As shown by the mean pressure field in figure 3.9, the primary vortex is accompanied by a large zone of low pressure level, with a minimum of $p_{\min} = -0.496$ in $(x_p^{pv}, y_p^{pv}) = (2.46, 0.5)$, thus staggered with respect to the centre of rotation of the main vortex. It appears from table 3.1 that a downstream shift of the primary vortex is observed by increasing the resolution levels with respect to the solution in Cimarelli et al. [27]. A larger extension of the primary vortex is also found in the DNS study by Chiarini and Quadrio [24], which uses a finer resolution than Cimarelli et al. [27]. In their work, the centre of rotation of the primary vortex and the reattachment point are located at $(x_c^{pv}, y_c^{pv}) = (2.36, 0.33)$ and $x_r = 3.96$, respectively. Interestingly, the thickness of the primary vortex appears to be almost independent of the numerical method being the height of the centre of rotation very similar in the three solutions considered. This phenomenon can be ascribed to the independence between mean vertical component of the velocity, free-stream turbulence level [26] and also Reynolds number (see § 3.3.8), which is related to the presence of negative turbulence production phenomena in the leading-edge shear layer. It is suggested that these negative production phenomena are also responsible of the insensitivity of the mean vertical velocity solution on the spatial resolution employed. The constancy of the primary vortex height together with the reduction of its streamwise dimension leads to a different mean streamline velocity pattern for the

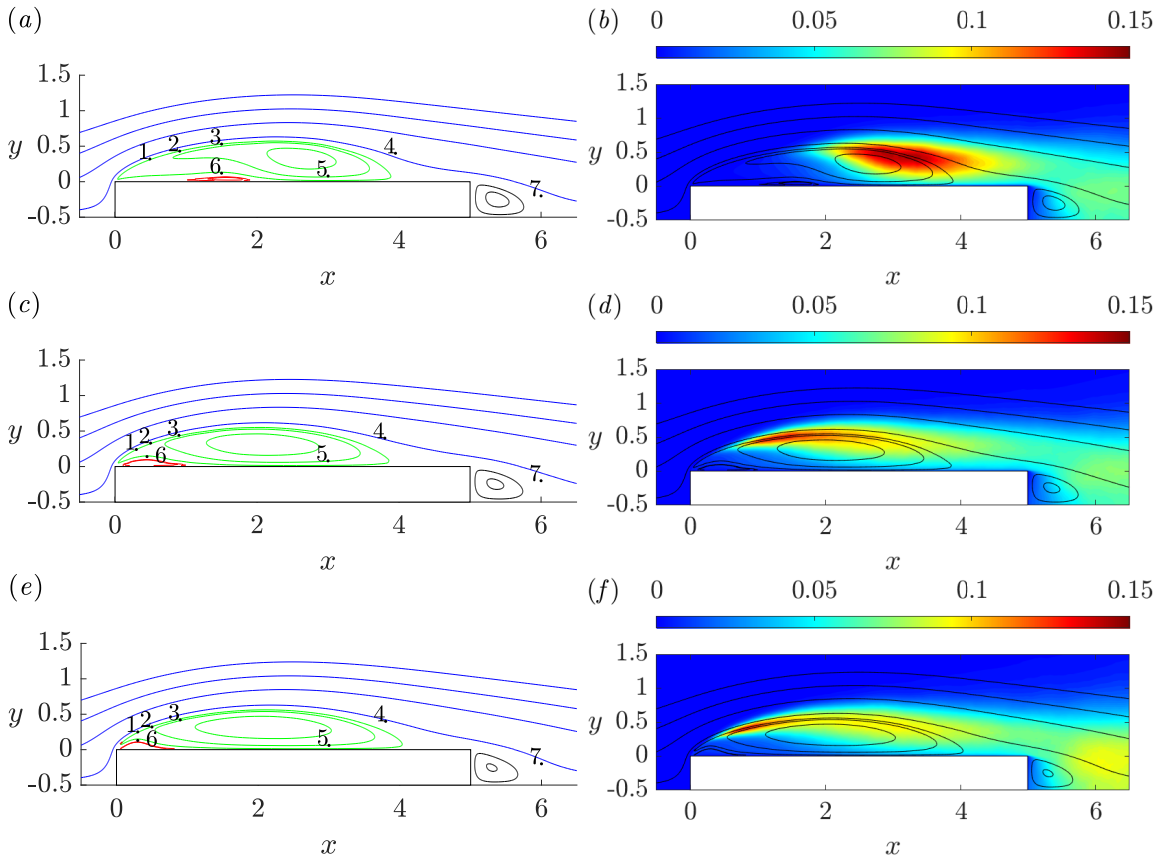

Figure 3.8. Mean flow fields for the flow cases at $Re_D = 3000$ (top panels), 8000 (middle panels) and 14000 (bottom panels). The left panels report the isocontours of the stream function. The green lines show the primary vortex, the red lines the secondary vortex and the black lines the wake vortex. The points with labels denote the locations used for the evaluation of frequency and wavenumber spectra in § 3.3.2 and 3.3.6. The right panels display turbulent kinetic energy field superimposed to mean velocity paths.

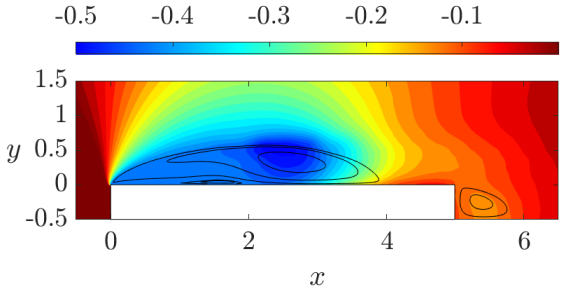

Figure 3.9. Mean pressure field at $Re_D = 3000$.

downstream portion of the primary vortex. Indeed, the mean streamline paths exhibit a higher curvature for the less resolved case, see figure 4 in [27], while they appear flatter in the present, highly-resolved simulation.

Upstream of the reattaching point and close to the wall, a boundary layer develops in the direction of the reverse flow induced by the primary vortex. This reverse boundary layer is subjected to an adverse pressure gradient, see §3.3.4, and eventually separates forming a second smaller counter-rotating separation bubble, hereafter called secondary vortex. The same downstream behaviour with increasing spatial resolution is also observed for the secondary vortex that will be discussed more in depth in the analysis of the friction coefficient.

A third recirculating zone takes place in the wake region of the rectangle owing to the flow separation at the trailing edge. This wake vortex develops from the trailing edge up to $x = 5.87$, and its centre of rotation is located at $(x_c^{wv}, y_c^{wv}) = (5.38, -0.25)$. As for the primary vortex, a low-pressure region is observed in conjunction with the wake vortex. However, in this case, both the extent and the intensity of the low-pressure region are smaller, $p_{wv} = -0.126$.

As shown by the map of turbulent kinetic energy $\langle k \rangle$ in figure 3.8(b), transitional mechanisms take place along the shear layer formed by separation at the leading-edge, thus leading to a fully turbulent flow field in the wake region of the primary vortex. Here, the highest turbulence levels are reached. The peak is found at $(x_k, y_k) = (3.09, 0.45)$ and its value is $k_{\max} = 0.145$. A second weaker region of turbulence intensity is identified in the wake of the rectangle. This region is associated with the vortices detaching from the trailing-edge [27] and gives a local maximum of 0.073 at $(x, y) = (6.27, -0.066)$, which is half the value $k_{\max}$. The process of transition from the initially laminar leading-edge shear layer to the fully turbulent conditions of the primary vortex wake is found to be anticipated in the less resolved case [27]. As a matter of fact, the point of transition to turbulence, identified as the location on the shear layer where the turbulent kinetic energy reaches the 10% of its maximum value, is found at $x_{tr} = 0.65$ [27] and $x_{tr} = 1.38$ for the present simulation. Moreover, in the less resolved case [27] the peak of turbulent kinetic energy is located at $(x_k, y_k) = (2.55, 0.39)$. Interestingly, this more rapid flow transition in the under-resolved case is not accompanied by an increase of the intensity of the turbulence fluctuations that are instead smaller, $k_{max} = 0.123$ [27]. Similar tendencies may also be recognised by comparison with the results in Chiarini and Quadrio [24], where the turbulent kinetic energy reaches a maximum value of $k_{max} = 0.135$ at $(x_k, y_k) = (2.70, 0.46)$.

Flow at $Re_D = 8000$ and 14000

In the flow cases at higher Reynolds number the general picture of the mean flow field around the rectangular cylinder, i.e. the occurrence of three main recirculating regions, remains

unchanged. However, significant variations are identified with regards to the characteristics of the separation bubbles and the turbulence levels within the recirculating regions. These are visible in the middle panels of figure 3.8 for the flow case at $Re_D = 8000$ and in the bottom panels of the same figure for $Re_D = 14000$, while details about the size and the positions of the recirculating vortices are summarized in table 3.1. As the Reynolds number increases, the primary vortex exhibits a wider extension along the streamwise direction. For the flow case at $Re_D = 8000$, the mean reattachment point is at $x_r = 4.25$ and the centre of rotation is found at $(x_c^{pv}, y_c^{pv}) = (2.04, 0.32)$. At $Re_D = 14000$, $x_r = 4.39$ and $(x_c^{pv}, y_c^{pv}) = (2.17, 0.33)$. On the other hand, the vertical length of the primary vortex appears to be almost insensitive to the Reynolds number, being the height of the centre of rotation and of the most external streamlines of the primary vortex essentially unaltered. As will be shown in §3.3.8, this phenomenon is again ascribed to the presence in the shear layer of a region of intense negative production of vertical fluctuations, and thus source of the mean vertical velocity, which is found to increase in magnitude with the Reynolds number.

The secondary vortex moves upstream with increasing Reynolds number. The main displacement towards the leading edge is observed when the Reynolds number is increased from $Re_D = 3000$ to 8000. When Re_D is raised up to 14000, the secondary vortex is additionally pushed towards $x = 0$ by the primary recirculating motion. By comparison between the different distributions of turbulent kinetic energy in the near-wall region, it emerges that turbulent fluctuations in the attached reverse boundary layer are more intense for the cases at $Re_D = 8000$ and 14000 than $Re_D = 3000$. The higher energy content increases the capability of the reverse flow to resist the adverse pressure gradient, and hence the reverse flow, on average, separates at more upstream distances.

With regards to the wake vortex, the centre of rotation nearly keeps the same position in the x–y plane but its longitudinal length is slowly reduced by increasing the Reynolds number, see table 3.1. In the wake, the local minimum of pressure is observed to decreases from $p_{wv} = -0.142$ to -0.163. This lowering of the base pressure is at the origin of the growth in the mean drag coefficient discussed in §3.3.2.

The Reynolds number strongly affects the transitional mechanisms of the leading-edge shear layer, see the progression in the right panels of figure 3.8. Turbulent fluctuations increase more quickly with the Reynolds number and a fully turbulent flow field is obtained at shorter streamwise distances from the leading edge. Accordingly, the maximum value of turbulent kinetic energy is observed in the first region of the shear layer, rather than in the vortex shedding region. In detail, a maximum value of $k_{\max} = 0.129$ is reached at $(x_k, y_k) = (1.31, 0.50)$ for the flow case at $Re_D = 8000$, while $k_{\max} = 0.130$ is found in $(0.78, 0.40)$ at $Re_D = 14000$. Interestingly, the peak values for the cases at higher Reynolds number are smaller than for $Re_D = 3000$.

In the experimental investigation by Moore et al. [91], the distributions of the maximum values of the turbulent kinetic energy as a function of the distance from the leading-edge x

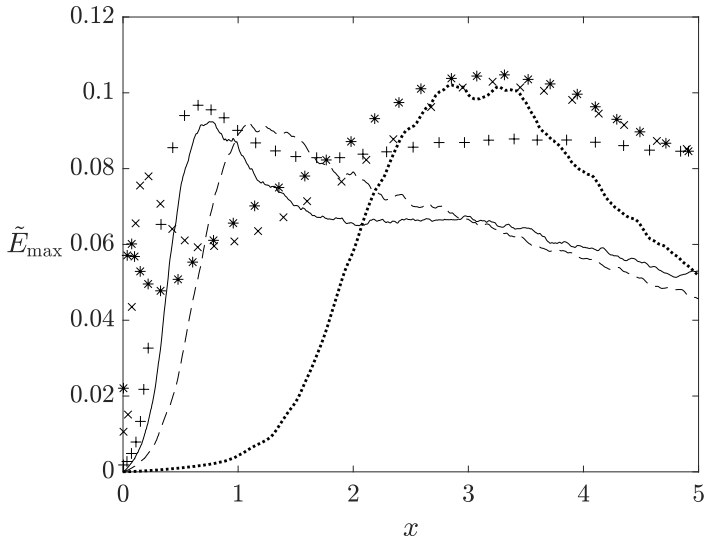

Figure 3.10. Downstream evolution of two-dimensional turbulent kinetic energy $\tilde{E}_{\max}$ for different values of the Reynolds number. Symbols are used to represent wind-tunnel data from Moore et al. [91]: $\cdots\cdots$, $Re_D = 3000$; - - - -, $Re_D = 8000$; ——, $Re_D = 14000$; $+$, $Re_D = 13400$; $\times$, $Re_D = 50600$; and $*$, $Re_D = 118000$.

are reported for three different Reynolds numbers, ranging from 13400 to 118000. Based on these plots, Moore et al. [91] report that the maximum value measured near the leading-edge decreases as the Reynolds number increases. The same kind of plot is reproduced in figure 3.10 using the results taken from the present numerical simulations and also including data from Moore et al. [91]. To obtain a better comparison, the same quantity used by the authors, i.e. the maximum value of the two-dimensional turbulent kinetic energy $\tilde{E}_{\max} = \frac{1}{2}(\langle uu \rangle + \langle vv \rangle)$ above the cylinder side, is considered here. Despite the two sets of curves, numerical and experimental, converge towards different values at the trailing-edge, good agreement is found where $\tilde{E}_{\max}$ reaches a maximum and the magnitude of these peaks, especially for $Re_D \sim 14000$. In addition, the following considerations can be made as regards the evolution of turbulence intensity for increasing Reynolds numbers. Starting from a low Reynolds number ($Re_D \sim 3000$), the transitional process of the shear layer culminates in the wake region of the primary vortex ($x > 3$), where fully turbulent flow is achieved. As the Reynolds number grows, turbulent fluctuations arise more quickly along the shear layer and the peak of intensity is reached at upstream distance. Downstream the region of maximum turbulence intensity, fluctuations are weaker. By further increasing the Reynolds number ($Re_D > 50000$), the initial rise of turbulent kinetic energy becomes steeper, but the level of intensity of the peak decreases. In these conditions, it appears that the shedding of vortices gives rise to an additional region of strong turbulence intensity in the wake region of the primary vortex, as already observed for the flow case at lower Reynolds number [65, 105].

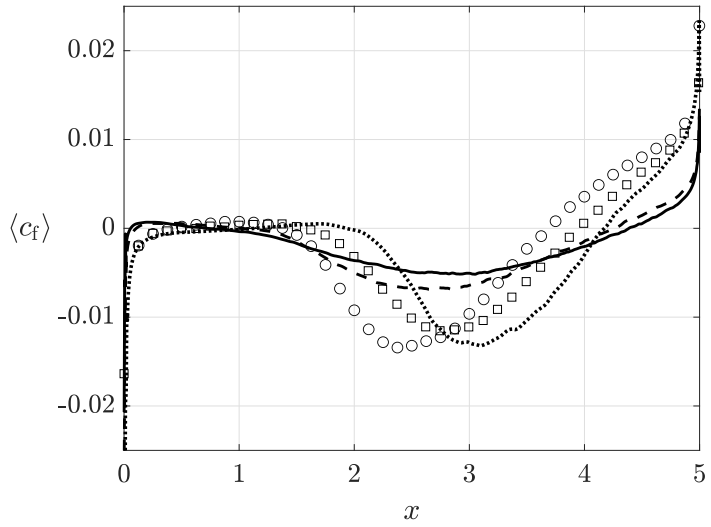

Figure 3.11. Downstream evolution of the average skin friction coefficient at the side wall of the rectangle for increasing values of the Reynolds number: ·····, $Re_D = 3000$; - - - -, $Re_D = 8000$; and ——, $Re_D = 14000$. Markers represent the results from previous DNS studies at $Re_D = 3000$: ◯, Cimarelli et al. [27]; and □, Chiarini and Quadrio [24].

Finally, the Reynolds number also promotes the mechanism of amplification of turbulence fluctuations exerted by the trailing-edge shear-layer, as shown by the higher levels of $\langle k \rangle$ in the wake regions of figures 3.8(*d*,*f*).

3.3.4 Friction and pressure stresses

For practical applications like those of civil engineering, the evaluation of the wind loads is one of the most crucial aspects when studying the integrity and stability of a building. Numerical simulations used in design phase are required to provide fast, yet accurate predictions of statistical quantities related to aerodynamics forces. For this reason, the friction and pressure stresses acting on the cylinder sides and their dependence on the Reynolds number are analysed here. The distributions of the shear and pressure stresses are expressed by the dimensionless skin friction and pressure coefficients, c_f and c_p, defined as

$$c_\mathrm{f} \equiv \frac{\tau_w}{\frac{1}{2}\rho U_\infty} \quad \text{and} \quad c_\mathrm{p} \equiv \frac{p - p_\infty}{\frac{1}{2}\rho U_\infty}, \tag{3.4}$$

where τ_w is the shear-stress at the wall and p_∞ is the freestream pressure, which is equal to zero in the present simulations.

Flow at $\boldsymbol{Re}_D = 3000$

Figure 3.11 shows the development of $\langle c_\mathrm{f} \rangle$ along the cylinder side for different flow conditions. Data from the simulations by [27] and Chiarini and Quadrio [24] are also included for

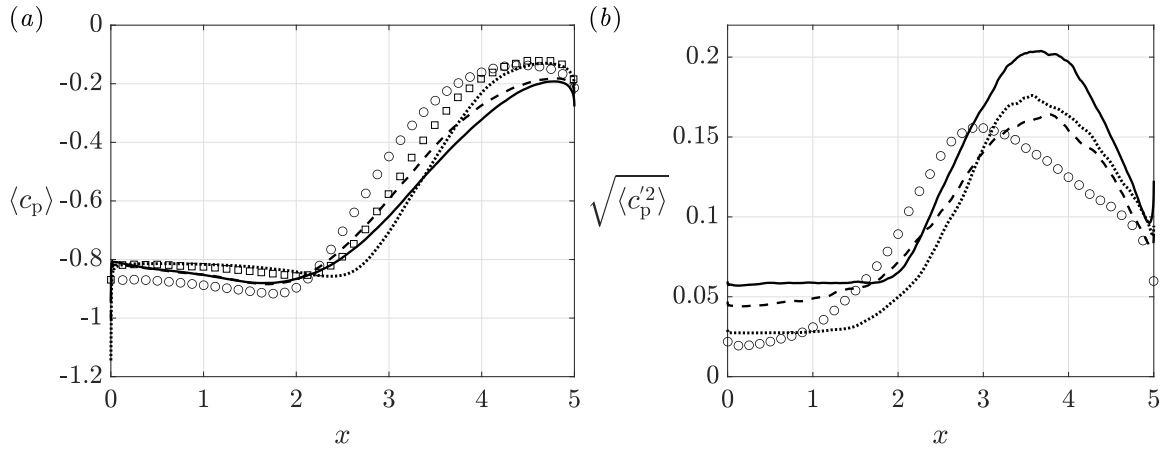

Figure 3.12. Pressure coefficient (a) and standard deviation of the pressure coefficient (b) at the side wall of the rectangle for increasing values of the Reynolds number: ·····, $Re_D = 3000$; - - - -, $Re_D = 8000$; and ——, $Re_D = 14000$. Markers represent the results from previous DNS studies at $Re_D = 3000$: ◯, Cimarelli et al. [27]; and □, Chiarini and Quadrio [24].

comparison and to assess the influence of a different spatial resolution in the flow case at $Re_D = 3000$. The mean skin friction coefficient is negative at the leading edge of the body and steeply increases up to a positive plateau in the region of the forward boundary layer formed by the secondary vortex. It becomes negative in the region of the primary vortex and changes again sign at the reattachment point position. In the most downstream part, a forward boundary layer forms, up to the definitive separation at the trailing edge.

Comparison of present results to those by Cimarelli et al. [27] suggests that the accurate spatial representation has an important role in the accuracy of first-order statistics. The secondary vortex region ranges $1.14 < x < 1.93$ in the present simulation with a high spatial discretisation and $0.42 < x < 1.38$ in Cimarelli et al. [27]. More downstream, the skin friction becomes negative and reaches a minimum. The magnitude of this minimum is only slightly affected by the different spatial representation but its location is not, $x_{\min} = 3.09$ and 2.43 for the present simulation and Cimarelli et al. [27], respectively. An upstream shift of the average reattachment point is also observed, which can again be ascribed to a suboptimal spatial discretisation, i.e. $x_r = 4.17$ and 3.69 for the present simulation and Cimarelli et al. [27], respectively.

Results by Chiarini and Quadrio [24] are in between the two simulations discussed above. In the work by Chiarini and Quadrio [24], the positive plateau of $\langle c_f \rangle$ corresponding to the secondary recirculation region is observed for $0.63 < x < 1.59$. In addition, the negative peak in the central region of the cylinder side is located at $x = 2.82$ and takes a value of -0.012, while in the present case the negative peak reaches -0.013.

The pressure coefficient distribution on the side of the body $\langle c_p \rangle$ is depicted in figure 3.12(a) for the present simulations and those by Cimarelli et al. [27] and Chiarini and Quadrio [24]. It

exhibits an initial steep increase before a smooth decrease. In accordance with the streamwise shift of the flow dynamics depending on the spatial representation, the region of weak decrease ends with a minimum located at $x = 2.38$ and 1.81 and for the present case and in Cimarelli et al. [27], respectively. This minimum is found to be correlated to the low-pressure levels associated with the primary vortex core. Further downstream, pressure increases and $\langle c_\mathrm{p} \rangle$ reaches a maximum just before the trailing-edge separation. Despite the very slight difference in the magnitude, the two maxima are measured at different streamwise positions, $x = 4.70$ and 4.43 for the present case and Cimarelli et al. [27]. The spatial distribution of the pressure coefficient is also presented in Chiarini and Quadrio [24]. Over the first half of the body, results almost match the present simulation. The steep increase over the downstream half of the body is instead shifted upstream. The maximum of $\langle c_\mathrm{p} \rangle = -0.124$ occurs at $x = 4.62$, while in the present case a value of -0.130 is reached.

Besides pressures, also the accurate prediction of pressure fluctuations is very important in wind engineering applications. Pressure fluctuations display a similar sensitivity of the solution to the numerical method as observed for the averaged quantities, see the figure 3.12(b). In detail, the standard deviation of the pressure coefficient has a maximum intensity of 0.176 at $x = 3.58$ in the present case and of 0.16 at $x = 2.96$ in Cimarelli et al. [27]. It appears that spatial resolution is also able to affect the intensity of fluctuations.

Flow at $Re_D = 8000$ and 14000

The initial rise of $\langle c_\mathrm{f} \rangle$ becomes steeper with the Reynolds number. For this reason, the forward boundary layer associated with the secondary vortex occurs just downstream of the leading-edge for the flow cases at higher Reynolds number. The reattachment of the reverse flow is now forced by the laminar leading-edge separation. In particular, the secondary vortex develops in the range $0.11 < x < 1.03$ and its centre of rotation is $(x_c^{sv}, y_c^{sv}) = (0.38, 0.050)$ for the flow case at $Re_D = 8000$. By raising the Reynolds number up to 14000, the same vortex covers $0.06 < x < 0.72$ and has centre in $(0.26, 0.052)$. Downstream of the secondary vortex region, the decrease of viscous stresses is smoother. Indeed, the magnitude of the minimum values in the central region of the cylinder reduces with Re_D.

Interestingly, the reattaching point x_r of the mean flow is found to move towards higher distances from the leading edge with the Reynolds number. This downstream trend seems to conflict with results by Mannini et al. [80] and Moore et al. [91] which report a reduction of the separation bubble mean length at Reynolds number values higher than 10^4. The occurrence of this phenomenon can be better understood by analysing the development of the recirculating flow region in the immediate vicinity of the backward-facing step [47, 5, 2], or on the side of a bluff flat plate [97], under different flow regimes. Notice that for these flow cases the Reynolds number is defined by the step height, or half the plate thickness. At Reynolds numbers below 10^3, the flow is laminar both at separation and at reattachment, and

the reattachment length increases with the Reynolds number. After the onset of transition in the separated shear layer, the reattachment length experiences an initial strong decrease with increasing Reynolds number, followed by a sudden mild increment for Reynolds-number values close to $\sim 10^4$, see figure 4 of Armaly et al. [5]. At the highest Reynolds numbers, the flow is turbulent at separation and at reattachment, and the reattachment length slightly depends on the Reynolds number [93, 25]. It is pointed out that in the flow around the rectangular cylinder the free shear layer undergoes a similar transitional process from the laminar condition than the flow cases considered above. In addition, the range of Reynolds number investigated in the present work is comparable with the upper limit of the transition regime described above. It is therefore reasonable to argue that, also for the flow around the rectangular cylinder, a range of the Reynolds number may exist close to $\sim 10^4$ where the reattachment length slightly increases with the Reynolds number. For higher Reynolds numbers, $Re_D \gtrsim 10^4$, the behaviour reported by Mannini et al. [80] and Moore et al. [91] is expected to be recovered, and hence the separation bubble mean length decreases with Re_D.

The effect of the Reynolds number on the average pressure coefficients $\langle c_\mathrm{p} \rangle$ is now analysed. For higher values of the Reynolds number, the pressure coefficient exhibits a much more marked decrease in the first region of the rectangle, thus evidencing the existence of a stronger adverse pressure gradient in the reverse flow. Despite these conditions enhance the flow separation, the reverse boundary layer is observed to separate, on average, at distances more upstream with respect to the flow case at $Re_D = 3000$. Indeed, as revealed by analysis of the one-dimensional spectra of the turbulent kinetic energy in § 3.3.6, the energy content of the turbulent motions in the reverse boundary layer increases with the Reynolds number. This strengthening of turbulent fluctuations makes the reverse flow less prone to separation and leads to the upstream displacement of the secondary bubble.

The minimum points are found at decreasing distances from the leading-edge, in agreement with the upstream shift of the low-pressure region indicative of the primary vortex. For the flow cases at $Re_D = 8000$ and 14000, $\langle c_\mathrm{p} \rangle$ takes the same minimum value of ≈ -0.88 at $x = 1.62$ and 1.60, respectively. In the region downstream, the rate of growth of the pressure coefficient decreases with the Reynolds number, thus lower peaks are reached in the same region upstream of the trailing-edge, i.e. -0.182 and -0.192 in ascending order of Re_D.

Finally, pressure fluctuations on the cylinder side are observed to increase with the Reynolds number and to become more intense in the region upstream of the reattachment point. However, the peak magnitudes of the profiles are not easily sorted by Reynolds number at first glance. Actually, the maximum value of $\sqrt{\langle c_\mathrm{p}'^2 \rangle}$ is observed to decrease down to 0.164 while rising from $Re_D = 3000$ to 8000, and then to increase up to 0.204 at $Re_D = 14000$.

3.3.5 The effect of the spatial discretisation

As shown by the comparison between results at $Re_D = 3000$ in the previous sections, the spatial discretisation appears to considerably influence the flow solution. In this section an analysis is carried out on the spatial discretisation, where the discussion is primarily focused on the flow case at $Re_D = 3000$ and its comparison with the work by Cimarelli et al. [27]. This analysis prompts some remarks that will be applied for the assessment of the mesh resolution of the simulations at higher Reynolds number. Contrarily to other canonical flows, the aerodynamics of bluff bodies with sharp edges is characterised by several strongly inhomogeneous phenomena (sharp corner separation, shear-layer transition, free turbulence, wall turbulence, vortex shedding), each of them requiring a specific resolution level. For this reason, the spatial discretisation issue will be studied separately for two main physical phenomena and regions, i) the forward/reverse boundary layers and ii) the free turbulent flow.

In the following analysis, the spacings $\Delta x, \Delta y, \Delta z$ used for the present simulations are computed as the distance between $N + 1$ uniformly spaced nodes within a specific spectral element. The only exception is given by the wall-normal resolution near the wall, which is expressed as the distance from the wall of the second Gauss-Lobatto-Legendre (GLL) quadrature point and it is denoted by Δy_w [54]. In the Finite Volume method used by Cimarelli et al. [27], the spatial resolution is expressed as the size of the Cartesian hexahedral volumes in the three spatial directions. Also in this case, the only exception is given by the wall-normal resolution near the wall that is computed as the distance from the wall of the central node of the first near-wall volume and it will be again denoted by Δy_w.

Note that in this analysis the phenomenon of the laminar flow separation at the sharp corner is not treated. In the present simulations, the mesh close to the leading-edge corner is designed with the smallest grid spacing of the whole domain. The grid size is selected to resolve the mean gradients of velocity and pressure, and to avoid the occurrence of local spurious oscillations associated to numerical instabilities. The same principle is also adopted in most of the numerical simulations about the BARC flow configuration [83, 26, 126] and bluff bodies with sharp corners [117, 23]. The grid spacings at the leading-edge corner are listed in table 3.4.

The forward and reverse boundary layers

As shown in section 3.3.4, starting from the reattachment point one boundary layer develops upstream and a second downstream. Despite the turbulent character of these two boundary layers, as these ensue the wall impingement of an already turbulent stream, their properties are not directly connected to the classical boundary layer theory. As an example, the variations of the mean skin friction coefficient shown in figure 3.11 are not due to the development of small-scale turbulent fluctuations but are mainly driven by the upstream and downstream

Table 3.4. Details of the spatial discretisations used in the present simulations and in the simulation by Cimarelli et al. [27]. The minimum spacings are obtained close to the leading-edge corner. The overbar indicates a streamwise average along the rectangle length.

	Present			Cimarelli et al. [27]
Re_D	3000	8000	14000	3000
$\Delta x_{\min}, \Delta y_{\min}$	0.0043	0.0029	0.0021	0.0040
$\Delta z_{\min}$	0.016	0.007	0.007	0.034
$\Delta x^+_{\max}, \overline{\Delta x^+}$	4.3, 1.7	3.2, 1.7	4.1, 2.3	34.7, 6.1
$\Delta y^+_{w\,\max}, \overline{\Delta y^+_w}$	0.47, 0.23	0.60, 0.36	0.66, 0.41	0.49, 0.31
$\Delta z^+_{\max}, \overline{\Delta z^+}$	3.9, 1.9	3.4, 2.0	5.1, 3.1	8.5, 5.4
$(\Delta x/\eta)_{\max}$	3.9	3.5	4.2	19.7
$(\Delta y/\eta)_{\max}$	3.3	3.8	4.6	3.2
$(\Delta z/\eta)_{\max}$	3.4	3.7	6.3	4.9

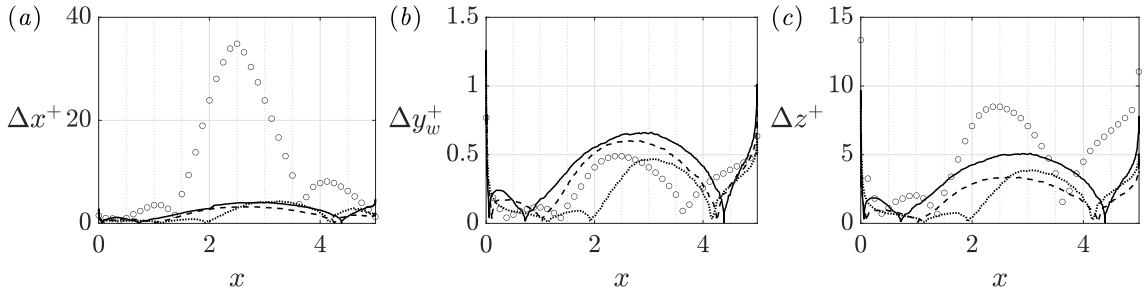

Figure 3.13. Distribution of the streamwise (a), vertical (b) and spanwise (c) grid spacings: ·····, $Re_D = 3000$; - - - -, $Re_D = 8000$; and ——, $Re_D = 14000$. Circle symbols ◯ are used to represent results from Cimarelli et al. [27].

flow accelerations. Indeed, in the reattachment region the friction coefficient is close to zero but, as shown in figure 3.8, this is the region in wall proximity with the highest levels of turbulent kinetic energy. Therefore, care should be taken in the use of friction units to assess the quality of the boundary layer resolution. The near-wall grid spacing in the very upstream part of the rectangular cylinder does not pose strict requirements because the boundary layer is characterized by low turbulence levels there, as visible by the turbulent kinetic energy pattern shown in figure 3.8. In quantitative terms, in the flow case at $Re_D = 14000$, where the reverse boundary layer exhibits the highest fluctuations, $\langle k \rangle$ reaches up to 20% of its maximum value for $x < 2$.

The near-wall resolutions for the present simulations are compared to those by Cimarelli et al. [27] in figure 3.13. The local viscous length scale $\delta_\nu = \nu/u_\tau$ is used to make spacings non-dimensional, non-dimensional quantities are then indicated by the superscript $+$. The behaviour of the near-wall resolution in all the three directions exhibit three peak values corresponding to the peaks of $\langle c_\mathrm{f} \rangle$ at the leading and trailing edges and in the reverse boundary layer region, see figure 3.11. The latter is particularly critical for the resolution

in the streamwise direction since it occurs where the common practice is to keep coarser spacings.

In the simulation at $Re_D = 3000$, grid spacings in the spanwise direction differ by a factor of two with respect to those of Cimarelli et al. [27]. In the streamwise direction the difference is much larger and can be quantified by a factor of seven. The evaluation of near-wall resolution for the two flow cases at higher Reynolds number gives maximum and mean results similar to the case at $Re_D = 3000$. Slightly higher values are computed at $Re_D = 14000$.

The free turbulence

As shown in figure 3.8, the highest turbulence levels are reached in the wake region of the primary vortex at $Re_D = 3000$, while are observed more upstream along the shear layer for higher Reynolds numbers. These turbulent fluctuations are the result of the transitional mechanisms taking place in the leading-edge shear layer and of the flow recirculation of the developed turbulent structures. Both, the transitional and fully turbulent mechanisms take place in regions of the flow that are relatively far from the rectangular cylinder and developing in a free-shear flow. Away from the walls the correct parameter to evaluate the accuracy of the resolution is the Kolmogorov scale η, defined in equation (2.4) for the grid turbulence flow case.

The isocontours of the ratio between the grid spacing in each spatial direction and η are shown in figure 3.14 for the flow case at $Re_D = 3000$. Values for the present work are displayed in the left panels while the right panels display values for Cimarelli et al. [27]. The same quantities have been evaluated for the cases at higher Reynolds number but are not reported here for the sake of brevity. Excluding the near-wall and wake regions, the maximum values of the ratios $(\Delta x/\eta)_{\max}, (\Delta y/\eta)_{\max}, (\Delta z/\eta)_{\max}$ can be found in table 3.4 for each of the flow cases considered. In figure 3.14, ratios are larger in the wake region of the primary vortex where the turbulence fluctuations are more intense and the Kolmogorov scale is smaller. Also in this case, the largest difference between the two simulations is in the streamwise direction. Also for the cases at $Re_D = 8000$ and 14000, the maximum values of the ratios are found close to the region of maximum turbulence intensity. Ratios are always lower than ≈ 4, except for $(\Delta z/\eta)_{\max} = 6.3$ at $Re_D = 14000$.

Discussion

In the above sections, a situation is described where non-negligible differences in the mean flow solutions at $Re_D = 3000$ are found, which are attributed to a suboptimal resolution employed by Cimarelli et al. [27]. The spanwise grid spacing differ by a factor of two while the difference in the streamwise direction is much higher with ratios between grid spacings about seven. The observed lack of resolution in Cimarelli et al. [27] is particularly important in the central and downstream regions of the rectangular cylinder.

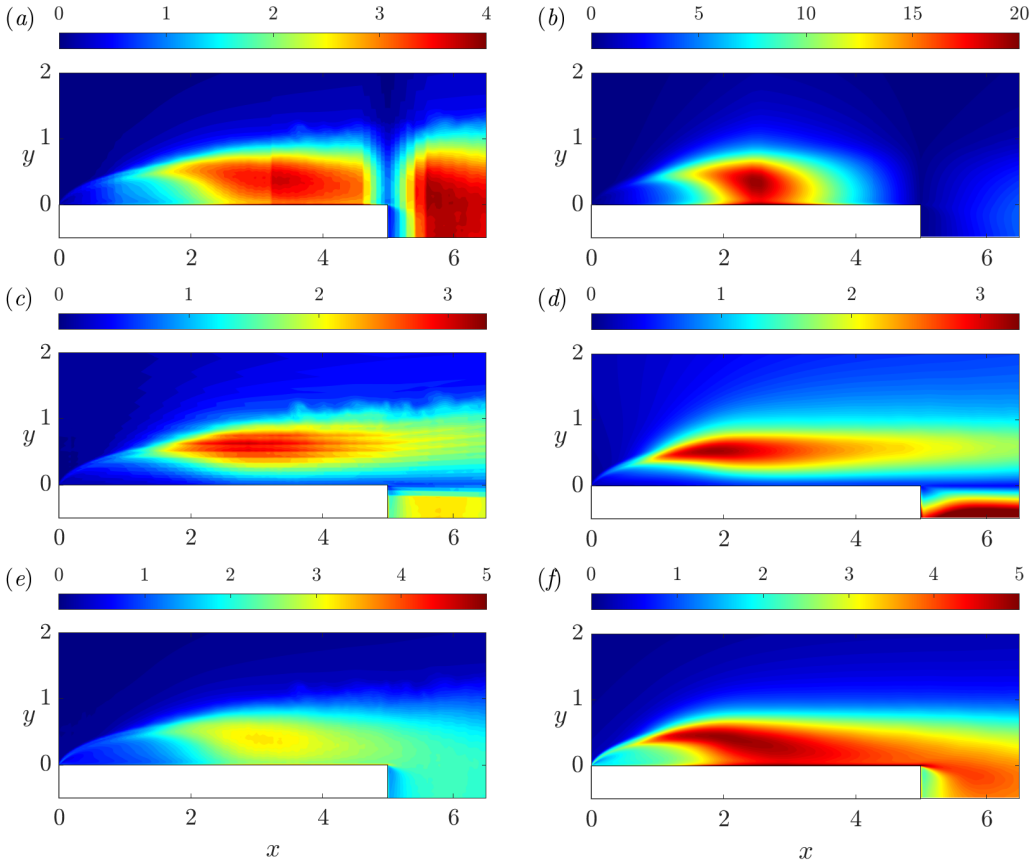

Figure 3.14. Distribution of the streamwise $\Delta x/\eta$ (top panels), vertical $\Delta y/\eta$ (central panels) and spanwise $\Delta z/\eta$ (bottom panels) spatial resolution. The left panels report the results for the present simulation while the right panels show the results for the simulation in Cimarelli et al. [27]. Notice that colour map limits for the representation of grid spacings in the streamwise direction do not match.

To distinguish the effect of resolution in the spanwise and streamwise direction, relevant information is provided in the work by Bruno et al. [17]. In this work a study is performed of the effect of the sole spanwise resolution on the main flow statistics. It is found that by increasing the spanwise resolution level, the recirculating flow dynamics moves significantly upstream and the peak pressure fluctuation $\sqrt{\langle c_{\mathrm{p}}'^2 \rangle}$ decreases. This behaviour is exactly the opposite as compared to what observed here, see §3.3.4. Since in the present case at $Re_D = 3000$ the resolution is increased in both horizontal directions, but more markedly in the streamwise direction, it can be hypothesised that the difference in flow solutions is essentially due to the significant mesh refinement in the streamwise direction. It is hypothesised that the effect of the marked increases in streamwise resolution might be as important as to shadow the expected opposite effect that would be given by a better resolution in the spanwise direction, as shown in Bruno et al. [17].

The circumstance that the main difference in the solutions is given by the different resolution in the streamwise direction is somewhat unexpected. The common practice in boundary layer and channel flows assumes that the requirements for the correct representation of turbulent structures are generally less strict in the mean flow direction. Consistently it is generally thought that the cross-flow directions and especially the inhomogeneous direction, need to be finely discretised. These assumptions are actually accurate in many canonical flows such as turbulent channels, pipes, and boundary layers [88].

In the case of a rectangular cylinder with sharp corners and flow reattachment the streamwise resolution plays a role which is at least as important the cross-flow directions, probably due to the strong curvature of the mean velocity field in the primary vortex. It is reasonable to assume that the advected turbulent structures are also oriented by the mean flow field. As a result, the streamwise direction turns out to become a cross-flow direction in several regions of the flow.

3.3.6 Structures of the flow and two-point statistics

In this section, two-point statistics, such as autocorrelation coefficients of velocity fluctuations and one-dimensional spectra of turbulent kinetic energy, are used to identify the main turbulent structures of the flow and to study the turbulent kinetic energy distribution across the scales of motion. A detailed description of the statistically dominant structures of the flow at $Re_d = 3000$ is reported by Cimarelli et al. [28]. In Cimarelli et al. [28] the characterization of the turbulent structures above the cylinder is functional to the assessment of the self-sustaining mechanisms of the flow, described in the same work by the authors.

For the present flow configuration, the velocity autocorrelation coefficients ρ_{ii} are only for separations along the z-direction, hence

$$\rho_{ii}(x, y, r) = \frac{R_{ii}(x, y, r\boldsymbol{e}_3)}{R_{ii}(x, y, 0)}. \tag{3.5}$$

The one-dimensional spectrum of turbulent kinetic energy is defined as

$$E_{kk}(\kappa_3, x, y) = \frac{1}{2} \langle \hat{u}_i(\kappa_3, x, y) \hat{u}_i^*(\kappa_3, x, y) \rangle \,, \tag{3.6}$$

where the summation convention is applied.

In each of the flow cases examined, correlation coefficients and wavenumber spectra are evaluated at four different points of the x–y plane. These locations are chosen as representative of the physical phenomena taking place in four different regions: the transitional region of the leading-edge shear layer, the primary vortex shedding region, the attached reverse boundary layer, and the separated reverse boundary layer. The point indicative of the transitional region is here identified as the location where turbulent kinetic energy reaches about the 20% of its maximum value and corresponds to point 3 for the flow case at $Re_D = 3000$, point 2 at $Re_D = 8000$, and point 1 at $Re_D = 14000$; see left column panels of figure 3.8 for points visualization and table 3.3 for their spatial coordinates. The other three regions, in the order, are evaluated at points from 4 to 6.

Flow at $Re_D = 3000$

Figure 3.15 shows the spanwise correlations of the three components of velocity fluctuations evaluated in the transitional leading-edge shear layer. The study of the instantaneous pattern of vortical structures in §3.3.1 evidenced the occurrence of large spanwise rolls in the laminar shear layer region. The high levels of correlations found for the streamwise and vertical fluctuations suggest that dominant motions in the transition region are still reminiscent of the two-dimensional spanwise vortices and are spanwise-oriented. Actually, the arising of streamwise and vertical components of the vorticity field, caused by the instability mechanisms in the shear layer, induces the deformation, or corrugation, of the spanwise vortex core [61, 1], well visible in figure 3.2(c). The separation length at which the spanwise fluctuations show a peak of anticorrelation, i.e. $r = 0.43$, may be interpreted as a statistical measure of the spanwise distance between two consecutive crests of the corrugated vortex core.

In the shedding region of the primary vortex, turbulence is developed and spanwise correlations decay quickly, see figure 3.16. The fluctuating velocity field exhibits a zero value of correlation at $r = 0.30$ and 0.48 for the streamwise and the spanwise components, respectively. For further separation distances, a peak of anticorrelation is recognised for ρ_{11} but not for ρ_{33}. The minimum value is computed at $r = 0.48$ for streamwise fluctuations. On the other hand, vertical fluctuations keep slightly positive correlation for $r < 1.5$. The results about ρ_{11} are in good agreement with the spanwise correlation behaviour observed by Cimarelli et al. [27] in the same region of the flow. However, in Cimarelli et al. [27] also vertical and spanwise fluctuations show distinct peaks of anticorrelation and the minimum values occur at $r = 0.5$, 0.45 and 0.9 for the streamwise, vertical and spanwise fluctuations, respectively. Cimarelli et al. [27] associate the negative peaks in the spanwise correlations with

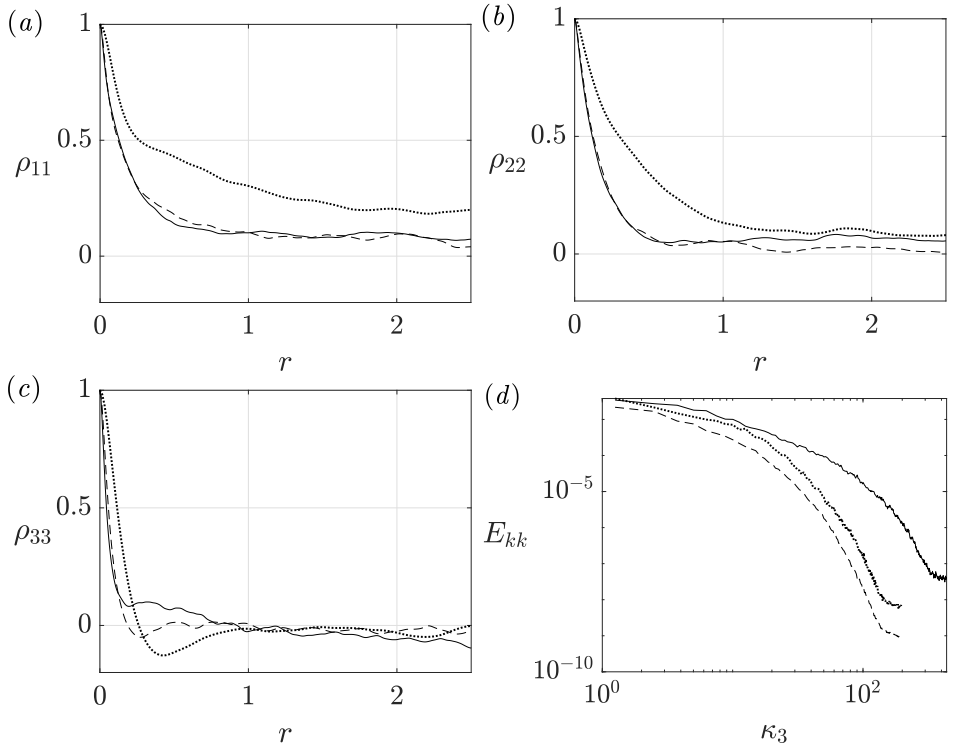

Figure 3.15. Autocorrelation functions of the streamwise (a), vertical (b) and spanwise (c) components of velocity fluctuations evaluated in the transitional region of the leading-edge shear layer at points 3, 2, and 1 for the flow cases at $Re_D = 3000$, $Re_D = 8000$, and $Re_D = 14000$ respectively: $\cdots\cdots$, $Re_D = 3000$; - - - -, $Re_D = 8000$; and ——, $Re_D = 14000$. (d) One-dimensional spectra of the turbulent kinetic energy evaluated at the same points.

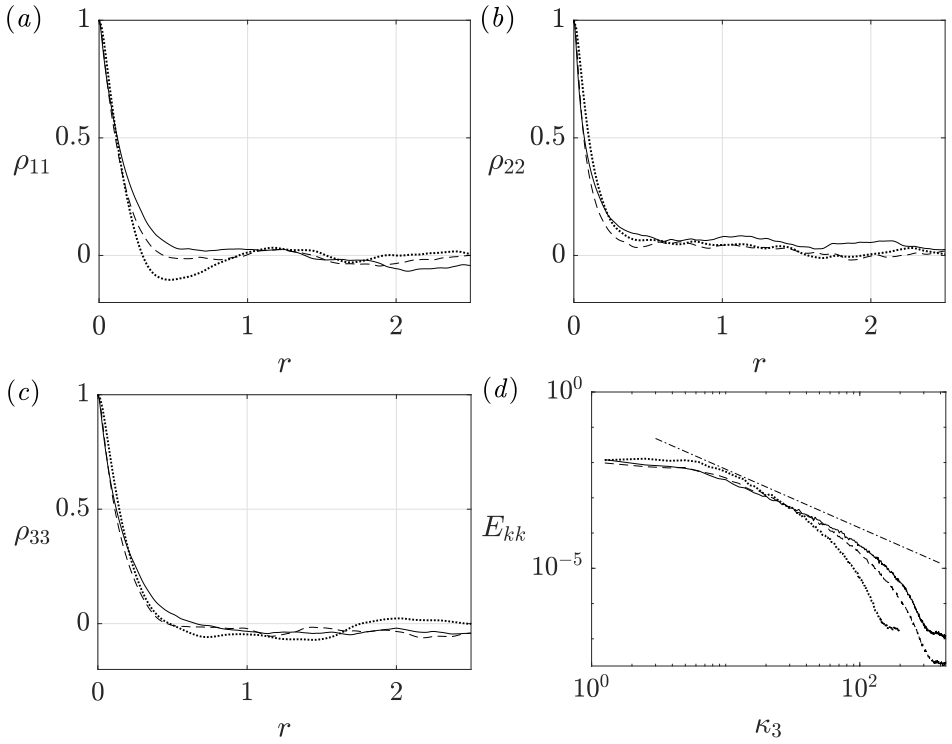

Figure 3.16. Autocorrelation functions of the streamwise (a), vertical (b) and spanwise (c) components of velocity fluctuations evaluated in the shedding region of the primary vortex at point 4: ·····, $Re_D = 3000$; - - - -, $Re_D = 8000$; and ——, $Re_D = 14000$. (d) One-dimensional spectra of the turbulent kinetic energy evaluated at point 4. The dot-dashed line with slope $-5/3$ highlights the power-law scaling exhibited by the spectra for different flow conditions.

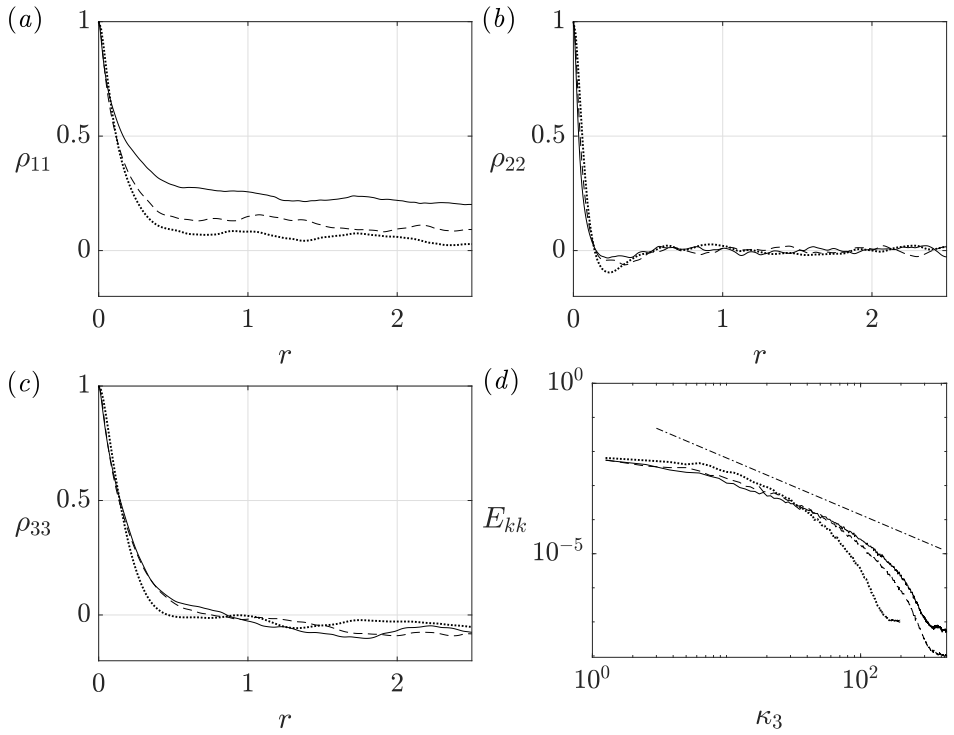

Figure 3.17. Autocorrelation functions of the streamwise (a), vertical (b) and spanwise (c) components of velocity fluctuations evaluated in the attached reverse boundary layer at point 5: ·····, $Re_D = 3000$; - - - -, $Re_D = 8000$; and ——, $Re_D = 14000$. (d) One-dimensional spectra of the turbulent kinetic energy evaluated at point 5.

the presence of streamwise vortices and streamwise velocity streaks resulting from motions induced by the hairpin vortices, following the analysis by Kim et al. [63]. In particular, the negative peak of ρ_{11} is a measure of the mean spanwise spacing between high and low streamwise velocity streaks, the negative peak of ρ_{22} is indicative of the statistical diameter of the streamwise vortices, and the negative peak of ρ_{33} provides a measure of the mean spacing between counter-rotating vortex pairs. In the present work, the absence of well-defined anticorrelation points for the vertical and spanwise fluctuations may indicate that the large structures are not as intense as the smaller-scale structures [116], and hence the streamwise vortices are shadowed by the small-scale structures of the turbulent flow.

The evolution of the spanwise correlation coefficients in the attached reverse boundary layer is reported in figure 3.17. The correlation coefficient ρ_{11} keeps positive also for large spanwise separation distances. This means that in the near-wall region of the reverse flow there is no signature of the alternating patterns of low- and high-velocity streamwise streaks observed in the shedding region above. On the other hand, the correlation of the vertical velocity decays rapidly and shows a negative minimum at $r = 0.24$. The spanwise fluctuations show a longer correlation length; ρ_{33} becomes approximately null for separation distances larger than $r \approx 0.50$.

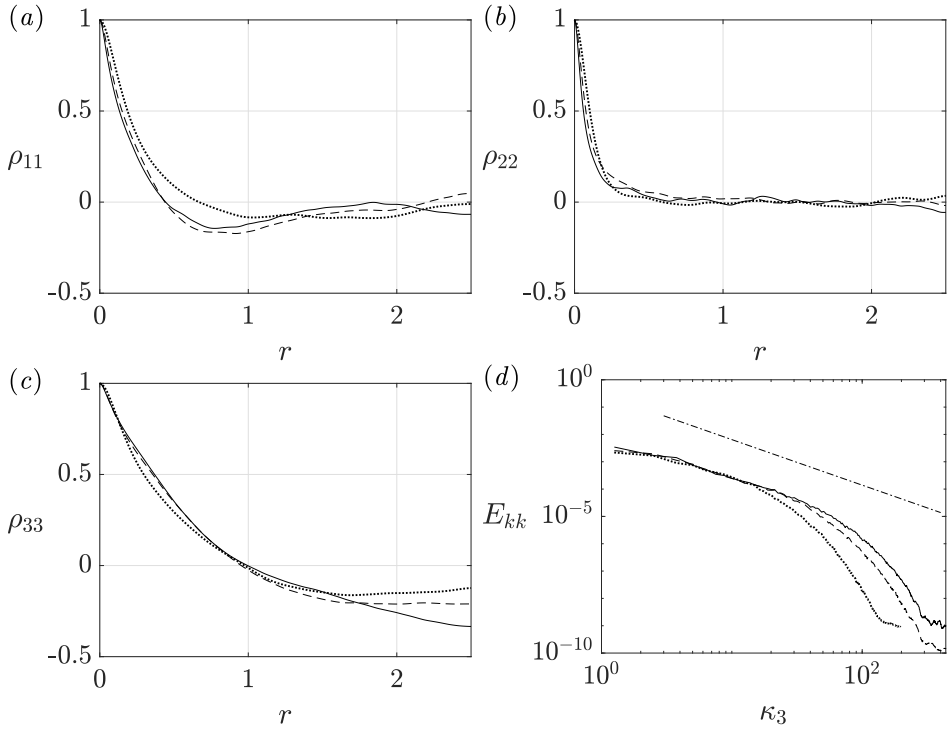

Figure 3.18. Autocorrelation functions of the streamwise (a), vertical (b) and spanwise (c) components of velocity fluctuations evaluated in the detached reverse boundary layer at point 6: $\cdots\cdots$, $Re_D = 3000$; - - - -, $Re_D = 8000$; and ——, $Re_D = 14000$. (d) One-dimensional spectra of the turbulent kinetic energy evaluated at point 6.

Spanwise correlations of the fluctuating velocity field are finally analysed for the detached reverse boundary layer in figure 3.18. In this region, all the components of velocity fluctuations take a zero-correlation value for relatively larger separation lengths with respect to previous points. In particular, spanwise correlations vanish at $r \approx 0.7$, 0.6 and 1 for streamwise, vertical and spanwise fluctuations respectively. These relatively large correlation lengths should be considered together with the instantaneous flow realization displayed in figure 3.2(d), representing the vortical structures characterized by negative streamwise velocity on the top side of the cylinder. It is noted that vortices reaching the upstream locations ($x < 2$) are elongated in shape and mostly extend along the spanwise direction. Thus, the presence of spanwise-oriented vortical structures in the detached reverse boundary layer is inferred. The same results are also found by Cimarelli et al. [28] by means of three-dimensional spatial correlation functions evaluated in the same region of the flow and for the same Reynolds number.

The energy contributions provided by the different scales of motions in the main turbulent regions of the flow are investigated by means of one-dimensional turbulent kinetic energy spectra E_{kk}. In the primary vortex shedding region turbulence has been developed and the maximum values of turbulence intensity are obtained, as shown by the high levels reached by the turbulent kinetic energy spectrum in figure 3.16(d). However, the spectrum evaluated in this region does not exhibit a clear $-5/3$ power-law behaviour with the wavenumber, thus highlighting that at the present Reynolds number, i.e. $Re_D = 3000$, a distinct separation between large energy-containing scales and small dissipative scales in the free-turbulence is absent. The characteristics of the turbulent kinetic energy spectrum in the attached reverse boundary layer, shown in figure 3.17(d), are similar to the ones observed in the vortex shedding region, although a slightly lower energy content is measured. In the separated reverse flow, the fluctuating velocity field undergoes a significant loss of turbulent kinetic energy over the whole range of resolved wavenumbers.

Flow at $\boldsymbol{Re}_D = 8000$ and 14000

The effects of the Reynolds number on the statistical dominant structures of the flow and on the energy content in the wavenumber space are now examined. The spanwise correlation coefficients in the transitional region of the leading-edge shear layer for the flow cases at $Re_D = 8000$ and 14000 are shown in figure 3.15 with dashed and solid lines, respectively. The strong positive autocorrelation of the streamwise and vertical fluctuations observed at $Re_D = 3000$ is significantly reduced with the Reynolds number. With regards to ρ_{33}, it shows higher decay rates and anticorrelation peaks decreasing in magnitude. For the flow case at $Re_D = 8000$, the minimum value is computed at $r \approx 0.25$, while at $Re_D = 14000$ correlation does not generate any negative peak. These distributions of spanwise correlations, together with previous analysis of the instantaneous flow fields in §3.3.1, suggest that the

spanwise structures generated by means of Kelvin-Helmholtz instability mechanism undergo stronger deformations with the Reynolds number. The growing perturbations of the shear layer progressively enhance the spanwise undulation of the vortex cores, until they break up into vortical structures with smaller size and irregular distribution.

In the wake region of the primary vortex, the negative correlation peak displayed by the streamwise fluctuations vanishes by raising the Reynolds number, as shown in figure 3.16(a). Beside the higher decay rates, no relevant differences are observed in the behaviour of ρ_{22} and ρ_{33} with increasing Reynolds number. In summary, the fluctuating velocity components exhibit poor autocorrelation along the spanwise direction and the streaky pattern observed for the case at $Re_D = 3000$ is not distinguishable for higher Reynolds numbers. This could be ascribed to the enrichment of the flow with structures of smaller scale and higher energy which tend to disrupt the development of the large scale vortical motions, see figures 3.3 and 3.4.

The effects of the Reynolds number on the spanwise correlations of the fluctuating velocity field in the attached reverse boundary layer is shown in figure 3.17. Interestingly, the positive spanwise correlation of the streamwise fluctuations is observed to increase with Re_D. The anticorrelation peak of ρ_{22} becomes lower in magnitude and ρ_{33} shows a higher decay rate for small separation r.

The situation in the detached reverse boundary layer is displayed in figure 3.18. Correlation coefficients of streamwise fluctuations decay more quickly with the Reynolds number and show peaks of anticorrelation; peaks are found at $r \approx 0.90$ and $r \approx 0.75$ for the flow cases at $Re_D = 8000$ and 14000, respectively. Correlation coefficients of spanwise fluctuations vanish for almost the same separation length and exhibit longer tails with the Reynolds number. This scenario suggests that spanwise structures still exist in the region of separated reverse flow for Reynolds numbers up to 14000, although they appear further distorted, as indicated by the rising of negative autocorrelation peaks for the streamwise fluctuations. Spanwise-oriented structures with decreasing size and length can also be identified in the instantaneous vortical patterns displayed in figures 3.3(d) and 3.4(d).

Variations in the distribution of turbulent kinetic energy in the wavenumber space are then studied. The one-dimensional spectra evaluated at the leading-edge shear layer confirm the anticipation of the transitional process along the shear layer with increasing Reynolds number. Not only turbulent fluctuations arise at lower distances from the leading-edge, but also the transfer of turbulent kinetic energy to the small-scale motions enhances with Re_D. In the shedding region and at $Re_D = 3000$, the turbulent kinetic energy is mostly spread over the wavenumber range $\kappa_3 < 20$, corresponding to the turbulent motions with wavelength $\ell = 2\pi/\kappa_3 > 0.3$. Spectra computed at $Re_D = 8000$ and 14000 are characterized by slightly lower intensity in the range $\kappa_3 < 20$ but decay more slowly for higher wavenumbers, thus retaining larger energy content at the smaller scales. These spectra exhibit a clear $-5/3$ decay throughout an appreciable wavenumber range, that corresponds to more than one

decade for the case at $Re_D = 14000$, see figure 3.16(d). This suggests that an inertial range becomes clearly observable in the shedding region starting from Reynolds numbers greater than $\sim 10^4$. The $-5/3$ power-law behaviour is also recognised in the one-dimensional spectra computed in the attached reverse boundary layer, shown in figure 3.17(d), although here lower energy levels are reached. The energy levels reached in the detached reverse boundary layer increase with the Reynolds number, as shown in figure 3.18(d). This growth of turbulent kinetic energy encompasses all the turbulent scales and underpins the separation resistance of the reverse boundary layer, as discussed in §3.3.4.

Finally, it is pointed out that the spectra obtained decay over several orders of magnitude and show negligible energy content at the highest wavenumbers. This supports the adequacy of the present spanwise discretisations.

3.3.7 Turbulent kinetic energy budgets

The spatial distribution of turbulent kinetic energy in the flow for increasing values of the Reynolds number was assessed in §3.3.3. The aim of the present section is to study how turbulent kinetic energy is produced, transported, and dissipated around the rectangular cylinder for different flow conditions. Terms of turbulent kinetic energy budget for the present flow configuration have been recently documented in several works [29, 91, 105, 24]. Chiarini and Quadrio [24] presented and discussed in detail the budget equations for the tensor of the Reynolds stresses, whose trace is two times the turbulent kinetic energy. The production of $\langle k \rangle$ in the leading-edge shear layer is addressed in the studies by Moore et al. [91] and Rocchio et al. [105], in the latter the authors also verify the effects of upstream-edge rounding. Cimarelli et al. [29] reported the existence of negative production phenomena in the shear layer, i.e. a reversal of flow energy from the mean field to the fluctuating field.

The transport equation of $\langle k \rangle$ was introduced in §2.3.11 with reference to grid turbulence case. For the nominally two-dimensional flow around the rectangle, the full budget equation (2.30) is rewritten in the following form, which is suitable for the analysis,

$$\frac{\partial \phi_j^k}{\partial x_j} = \mathcal{P}^k - \langle \widetilde{\epsilon} \rangle^k, \tag{3.7}$$

where ϕ_j^k are the fluxes of turbulent kinetic energy in the x and y directions and are defined as

$$\phi_j^k = \langle U_j \rangle \langle k \rangle + \langle u_j p \rangle + \frac{1}{2} \langle u_i u_i u_j \rangle - \frac{1}{Re_D} \frac{\partial \langle k \rangle}{\partial x_j}, \tag{3.8}$$

The four terms which appear in the definition of ϕ_j^k represent, in the order, the contributions given by the mean, pressure, turbulent and diffusive transports.

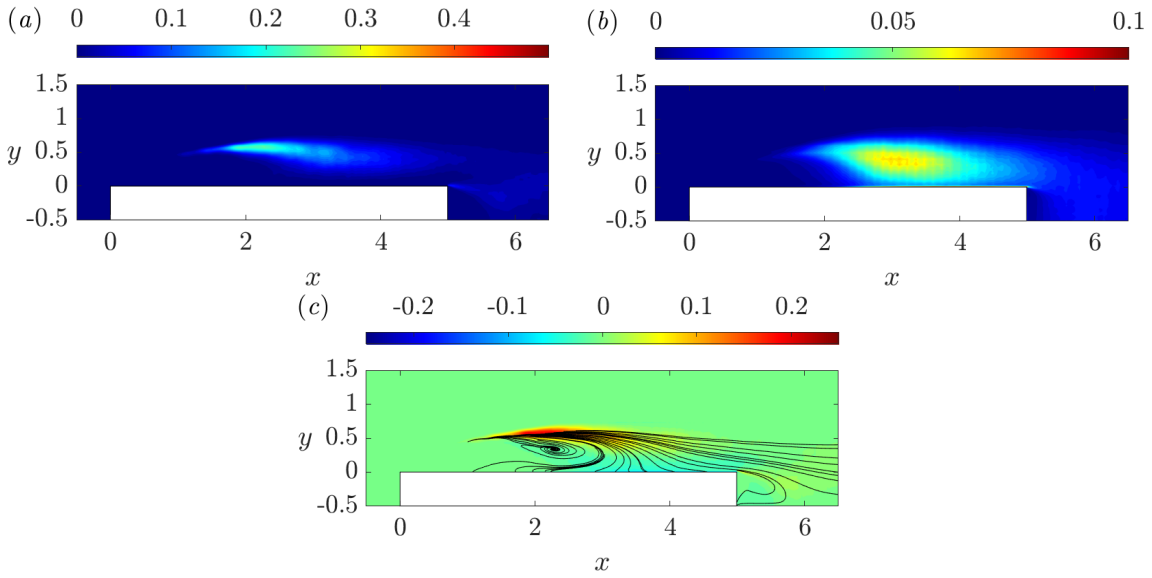

Figure 3.19. Production (a) and dissipation terms (b) of the turbulent kinetic energy budget at $Re = 3000$. (c) Distribution of $\mathcal{P}^k - \langle\widetilde{\epsilon}\rangle^k$ superimposed with field lines of energy flux $\boldsymbol{\phi}^k$.

Flow at $\boldsymbol{Re}_D = 3000$

Figure 3.19 shows the distribution of $\mathcal{P}^k$ and $\langle\widetilde{\epsilon}\rangle^k$, i.e. the production and the dissipation terms of turbulent kinetic energy, around the cylinder for $Re_D = 3000$. A positive value of $\mathcal{P}^k$ means that energy is drained from the mean velocity field to feed velocity fluctuations. The production of turbulent kinetic energy occurs along the leading-edge shear layer, in the region where instabilities are amplified under the action of high mean shears and transitional process takes place. The region of maximum $\mathcal{P}^k$ is positioned slightly upstream with respect to the area where high turbulence levels are obtained, in particular a peak of $\mathcal{P}^k_{\max} = 0.23$ is found at $(x, y) = (2.27, 0.588)$. In the wake of the primary vortex, the production keeps positive but shows lower values. A second region of turbulence production arises downstream of the cylinder, due to the action of mean velocity gradients in the trailing-edge shear layer on turbulent fluctuations generated in the boundary layer upstream.

Unlike Cimarelli et al. [29], there is no negative production region in the leading-edge shear layer, as revealed by figure 3.20, where distribution of the negative values of $\mathcal{P}^k$ is shown. Such absence is also observed by Chiarini and Quadrio [24] and is explained by evaluating the different contributions to the production terms of the normal Reynolds stresses $\langle uu\rangle$ and $\langle vv\rangle$. It is shown that in the first region of the shear layer, for $x < 1$, the dominant contribution is given by $-2\langle uu\rangle\frac{\partial U}{\partial x}$, which is responsible for the production of $\langle uu\rangle$ and is positive. The same holds true in the present simulation. Negative production of turbulence is found in the near-wall reattachment region. Here the turbulent motions impinge on the wall conveyed by the recirculating flow and part of the turbulent kinetic energy is redistributed to the mean flow, thus creating the reverse and forward boundary layers.

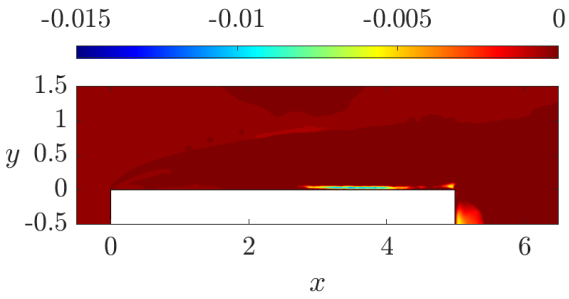

Figure 3.20. Isocontours of negative values of $\mathcal{P}^k$ around the cylinder at $Re = 3000$, to highlight the negative turbulent production regions existing in the flow.

The dissipation term $\langle\widetilde{\epsilon}\rangle^k$ is reported in figure 3.19(b). Large values of dissipation are observed along the shear layer, where turbulent fluctuations arise, and mainly in the core of the primary vortex. High dissipation values are also observed very close to the cylinder wall for $x > 2$, while in the region upstream viscous effects become less intense.

Figure 3.19(c) shows the mean path taken by the fluxes of turbulent kinetic energy distributed in the flow by means of turbulent, pressure, diffusive and convective processes. The lines of the vector flux $\boldsymbol{\phi}^k$ originate from a point located in the shear layer at $(x, y) \approx (1.00, 0.45)$ and develop in the flow forming different patterns. In a first branch, the excess of production of $\langle k\rangle$ (positive values of $\mathcal{P}^k - \langle\widetilde{\epsilon}\rangle^k$) is advected downstream towards the wake. In a second branch, $\langle k\rangle$ is conveyed towards the cylinder wall, where is dissipated by viscous actions. Interestingly, the lines of energy fluxes reach the most upstream part of the primary vortex, also revealing the reverse flow separation. The last fraction of the excess of $\langle k\rangle$ falls within the recirculating region of the primary vortex and is dissipated while involved in spiralling motions ending at the point $(x, y) \approx (2.28, 0.34)$, i.e. slightly upstream than the centre of rotation of the separation bubble.

Flow at $Re_D = 8000$ and 14000

Figures 3.21 and 3.22 show the terms of equation (3.7) for the flow cases at $Re_D = 8000$ and 14000, respectively. In accordance with the upstream shift of the transitional mechanisms with increasing Reynolds number, the region of maximum production of turbulent kinetic energy moves progressively towards the leading edge and becomes narrower. Given the higher mean velocity gradients in the shear layer, turbulence production is more intense and reaches a peak of $\mathcal{P}^k_{\max} = 0.52$ at $Re_D = 8000$, and $\mathcal{P}^k_{\max} = 0.83$ at $Re_D = 14000$. Also dissipation increases in magnitude with the Reynolds number, see figures 3.21(b) and 3.22(b). In these cases, the region of maximum dissipation is located more upstream and more detached from the wall.

The patterns followed by the energy fluxes, shown in figures 3.21(c) and 3.22(c), are similar with those reported for the case at lower Reynolds number, with the main difference

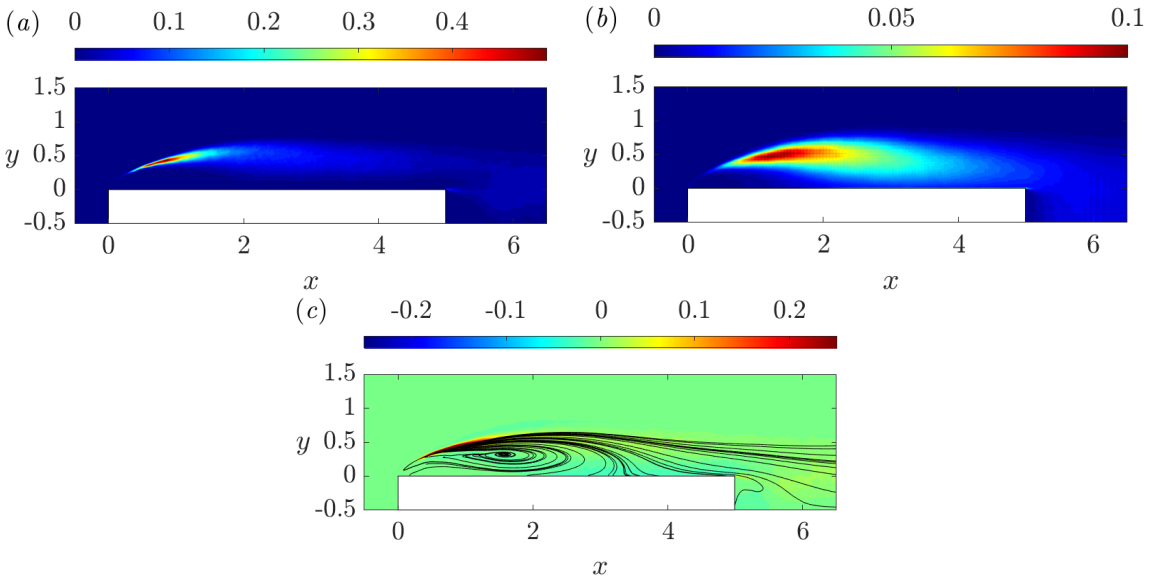

Figure 3.21. Production (a) and dissipation terms (b) of the turbulent kinetic energy budget at $Re = 8000$. (c) Distribution of $\mathcal{P}^k - \langle\tilde{\epsilon}\rangle^k$ superimposed with field lines of energy flux $\boldsymbol{\phi}^k$.

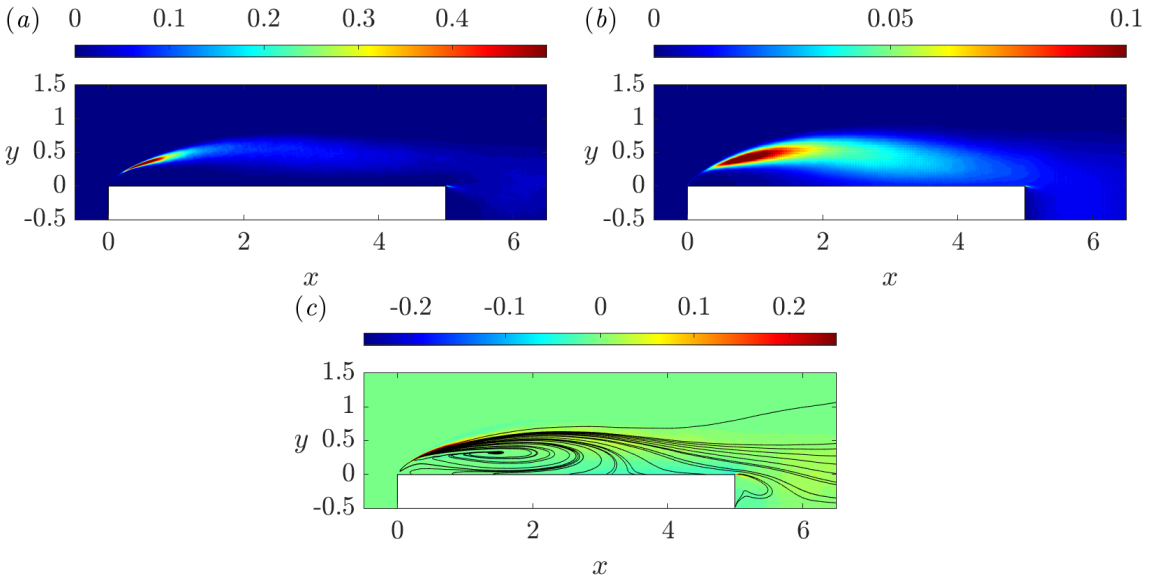

Figure 3.22. Production (a) and dissipation terms (b) of the turbulent kinetic energy budget at $Re = 14000$. (c) Distribution of $\mathcal{P}^k - \langle\tilde{\epsilon}\rangle^k$ superimposed with field lines of energy flux $\boldsymbol{\phi}^k$.

being the primary vortex recirculating region. In this case, the spirals formed by the lines entering the recirculating region have wider streamwise extent and get closer to the wall. The point where lines vanish is displaced more upstream, for example at $Re_D = 14000$ the point is located at $(1.5, 0.32)$, in accordance with the different topologies of the recirculating vortices. Part of the energy is still carried by the reverse flow near the wall and dissipated close to the leading-edge. The excess of production of $\langle k \rangle$, i.e. $\mathcal{P}^k - \langle \widetilde{\epsilon} \rangle^k$, increases with the Reynolds number, which means that a higher quantity of energy is being transported in the flow. In the transport of $\langle k \rangle$, the leading role is played by the mean contribution, which conveys most of the energy produced in the shear layer towards the sink near the wall and in the wake. The core of the primary separation bubble corresponds to a region of weak activity in terms of production and transport of $\langle k \rangle$. As a matter of fact, negative values of $\mathcal{P}^k - \langle \widetilde{\epsilon} \rangle^k$ in the core region are one order of magnitude smaller than the mean value computed along the wall, where the lowest levels are observed. This holds true at all the Reynolds numbers examined.

3.3.8 Reynolds-stresses budgets

In the previous sections the turbulent kinetic energy and the terms of its transport equation have been presented for increasing values of the Reynolds number. In this section, the separate contributions of normal and tangential Reynolds stresses are considered by examining budgets for the non-zero components of the Reynolds-stress tensor. Besides providing further elucidation of the physics of the turbulent energy, the interest in the budget equations of Reynolds stresses for the present flow configurations is due to their application in formulating Reynolds-averaged turbulence models designed specifically for separating and reattaching flows. As far as the author knows, the full Reynolds-stress equations for the flow around the rectangular cylinder with $c/D = 5$ have been only treated in the DNS study by Chiarini and Quadrio [24] for a single value of the Reynolds number, corresponding to $Re_D = 3000$. In the present work, a preliminary investigation on the Reynolds-stress budgets and their dependence on the Reynolds number is performed.

The transport equation for the component $\langle u_i u_j \rangle$ of the Reynolds-stress tensor in statistically steady conditions is written as

$$\frac{\partial \phi_{k,ij}}{\partial x_k} = \mathcal{P}_{ij} + \Pi_{ij} - \langle \widetilde{\epsilon} \rangle_{ij}. \tag{3.9}$$

In equation (3.9), the mean, pressure, turbulent and diffusive transport terms are considered as divergences of vector flux and grouped in the left-hand side term, thus $\phi_{k,ij}$ is

$$\phi_{k,ij} = \langle U_k \rangle \langle u_i u_j \rangle + \langle p u_k \rangle \left(\delta_{i,k} + \delta_{j,k} \right) + \langle u_i u_j u_k \rangle - \frac{1}{Re_D} \frac{\partial \langle u_i u_j \rangle}{\partial x_k}, \tag{3.10}$$

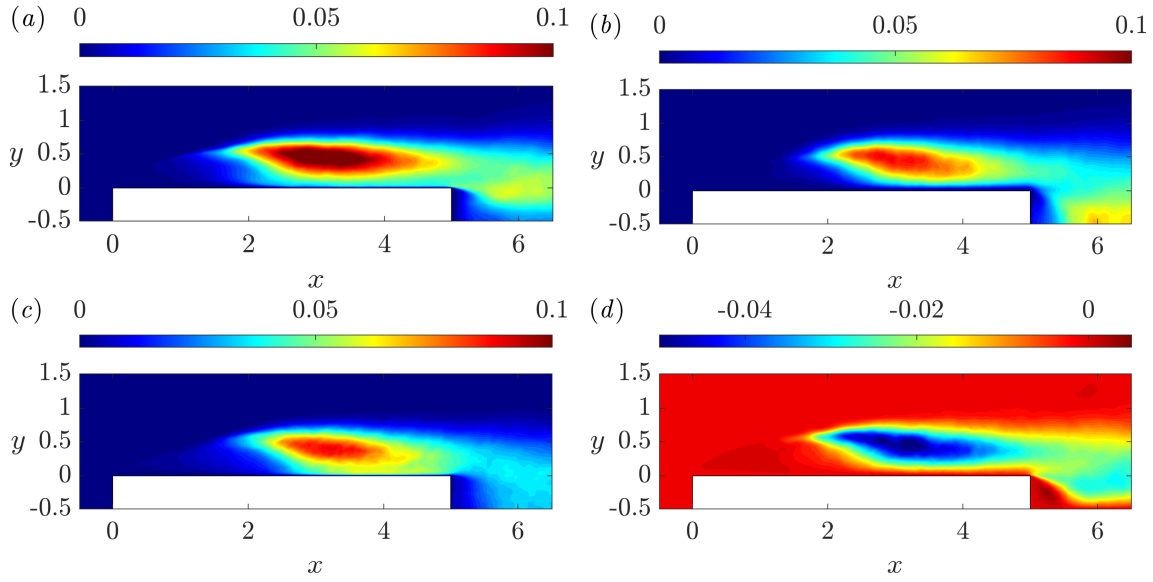

Figure 3.23. Distribution of the Reynolds stresses $\langle uu \rangle$ (a), $\langle vv \rangle$ (b), $\langle ww \rangle$ (c), and $\langle uv \rangle$ (d) around the rectangular cylinder at $Re = 3000$.

where $\delta_{i,j}$ is Kronecker's delta. The different terms in the right-hand side of equation (3.9) are the production $\mathcal{P}_{ij}$, the pressure-strain Π_{ij} and the pseudo-dissipation tensors $\langle \widetilde{\epsilon} \rangle_{ij}$, defined as

$$\mathcal{P}_{ij} = -\langle u_i u_k \rangle \frac{\partial \langle U_j \rangle}{\partial x_k} - \langle u_j u_k \rangle \frac{\partial \langle U_i \rangle}{\partial x_k}, \tag{3.11}$$

$$\Pi_{ij} = \left\langle p \frac{\partial u_i}{\partial x_j} \right\rangle + \left\langle p \frac{\partial u_j}{\partial x_i} \right\rangle, \tag{3.12}$$

$$\langle \widetilde{\epsilon} \rangle_{ij} = \frac{1}{Re_D} \left\langle \frac{\partial u_i}{\partial x_k} \frac{\partial u_j}{\partial x_k} \right\rangle. \tag{3.13}$$

The production, the pressure-strain and the pseudo-dissipation tensors can be added together to obtain a single source term $\psi_{ij} = \mathcal{P}_{ij} + \Pi_{ij} - \langle \widetilde{\epsilon} \rangle_{ij}$ expressing the excess of generation of $\langle u_i u_j \rangle$ in the flow [24]. It is recalled that each of the terms of the transport equation for the turbulent kinetic energy can be obtained by computing half the trace of the respective tensor.

Flow at $Re_D = 3000$

In the statistically two-dimensional flow around the rectangle, the only non-zero components of the Reynolds-stress tensor are the normal stresses $\langle uu \rangle$, $\langle vv \rangle$ and $\langle ww \rangle$, and the shear stress $\langle uv \rangle$, while the other tangential components vanish because of flow symmetries. The spatial evolutions of the four terms are displayed in figure 3.23. Their main characteristics have been already described by Cimarelli et al. [27], and later by Chiarini and Quadrio [24]. Fluctuations of the three velocity components become relevant for $x > 2$ and exhibit an area of maximum intensity above the cylinder. The intensity of the streamwise fluctuations is higher than

the other components and reaches a maximum value of 0.116 at $(x, y) = (3.12, 0.47)$. The distribution of $\langle uu \rangle$ is stretched along the streamwise direction and takes small values near the wall. In the wake, $\langle uu \rangle$ undergoes significant amplification throughout the trailing-edge shear layer and a further region of intense fluctuations is generated. Vertical fluctuations are characterized by smaller levels of intensity in the primary vortex region and show a peak of 0.090 at $(x, y) = (3.00, 0.48)$, hence at the same height from the wall but slightly upstream than the streamwise component. A second region of activity for the vertical component is found on the symmetry axis of the wake, as a result of the periodic shedding of large-scale vortices in the separated wake. The peak of the spanwise fluctuations is 0.090 and is located at $(x, y) = (3.36, 0.39)$. With respect to the other components, spanwise fluctuations are also spread in the near-wall region. A possible explanation of this distribution has been provided by Cimarelli et al. [27]. Actually, due to the strong curvature of the mean velocity field in the primary vortex, turbulent motions are conveyed towards the wall and horizontal fluctuations are generated in the wall impingement process. On the other part, wall-normal fluctuations vanish because of the wall impermeability constraint. The shear stress $\langle uv \rangle$ provides a relevant contribution to the production of turbulent kinetic energy, see its definition in equation (2.35). As shown in figure 3.23(d), $\langle uv \rangle$ is mostly negative on the top side of the cylinder and gives the lower values in the primary vortex region and in the wake. The minimum value, i.e. where streamwise and vertical fluctuations yield the highest correlation, is -0.052 and is found at $(x, y) = (3.01, 0.50)$, within the primary vortex. The only slightly positive regions of $\langle uv \rangle$ are observed in the upstream part of the primary vortex and in the wake vortex.

While qualitative agreement is found between the present distributions of the Reynolds stresses and those by Cimarelli et al. [27] and Chiarini and Quadrio [24], quantitative differences exist because of different representations of the mean flow field provided by each work, already discussed in § 3.3.5. For example, in Cimarelli et al. [27] the peaks of $\langle uu \rangle$, $\langle vv \rangle$, and $\langle ww \rangle$ are located at $(2.57, 0.44)$, $(2.96, 0.31)$, and $(2.96, 0.28)$ respectively; the corresponding maximum values are 0.118, 0.065 and 0.074. In Chiarini and Quadrio [24] peaks of the normal Reynolds stresses are found at $(2.71, 0.47)$, $(2.55, 0.51)$ and $(2.74, 0.45)$, while the minimum of $\langle uv \rangle$ occurs at $(2.69, 0.47)$. In comparison with data by Chiarini and Quadrio [24], maximum points in the present work are characterized by nearly the same vertical distance from the wall but are displaced slightly downstream. The main departures are observed for the spanwise fluctuations. These gaps further increase when the comparison is made with results by Cimarelli et al. [27].

The terms of the production tensor are plotted in figure 3.24. Note that P_{33} is zero given that $\langle W \rangle = 0$ and so do its spatial derivatives. With reference to the map of $\mathcal{P}_{11}$ in figure 3.24(a), the leading-edge shear layer and the shedding region of the main recirculating bubble are found to be the site of production mechanisms for the streamwise turbulent fluctuations at expanse of the mean flow. In the near-wall region, for $x > 2.7$, $\mathcal{P}_{11}$ exhibits

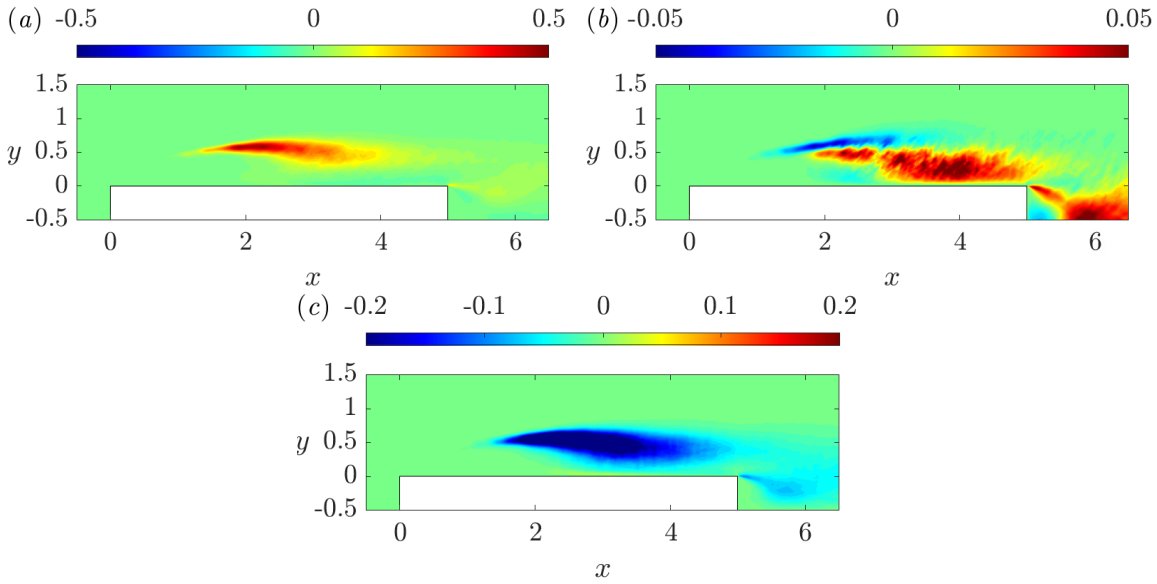

Figure 3.24. Distribution of the production tensor $\mathcal{P}_{ij}$ at $Re = 3000$. Production terms of $\langle uu \rangle$ (a), $\langle vv \rangle$ (b) and $\langle uv \rangle$ (c).

slightly negative values, thus indicating that a reversal of flow energy takes place to feed the streamwise mean velocity field. Streamwise fluctuations are also generated throughout the trailing-edge shear layer, while negative production is observed along the symmetry plane for $x > 5.4$. The production and draining mechanisms for the vertical fluctuations are less intense and show a different behaviour than the streamwise counterpart. The leading-edge shear layer acts as a sink for the vertical fluctuations to sustain the mean flow, while the shedding region of the primary vortex energy is characterized by positive production. Slightly negative values of $\mathcal{P}_{22}$ are also found in the near-wall region, for $x < 2.7$, and in the wake within the wake vortex. The large-scale shedding of vortices in the separated wake is associated with a region of intense production of $\langle vv \rangle$. The shear-stress production $\mathcal{P}_{12}$ is negative all around the cylinder, except in the near-wall region below the centre of the main recirculating region. The evaluation of the shear-stress components $\mathcal{P}_{12}$, Π_{12} and $\langle \widetilde{\epsilon} \rangle_{12}$ in terms of source and sink is not trivial and depends on the sign of $\langle uv \rangle$. Where $\langle uv \rangle$ is found to be negative, $\mathcal{P}_{12} < 0$ corresponds to a gain in $-\langle uv \rangle$ and thus to an increase in the magnitude of the shear stress. On the other hand, $\langle uv \rangle < 0$ in conjunction with $\mathcal{P}_{12} > 0$ corresponds to a sink of the shear stress. Based on these statements, in the great part of the domain a production of $-\langle uv \rangle$ takes place.

As pointed out by Cimarelli et al. [29], the nature of $\mathcal{P}_{11}$ and $\mathcal{P}_{22}$ is driven by different mechanisms which can be better understood by considering the separate contributions to the production terms

$$\mathcal{P}_{11} = -2\langle uu \rangle \frac{\partial \langle U \rangle}{\partial x} - 2\langle uv \rangle \frac{\partial \langle U \rangle}{\partial y}, \tag{3.14}$$

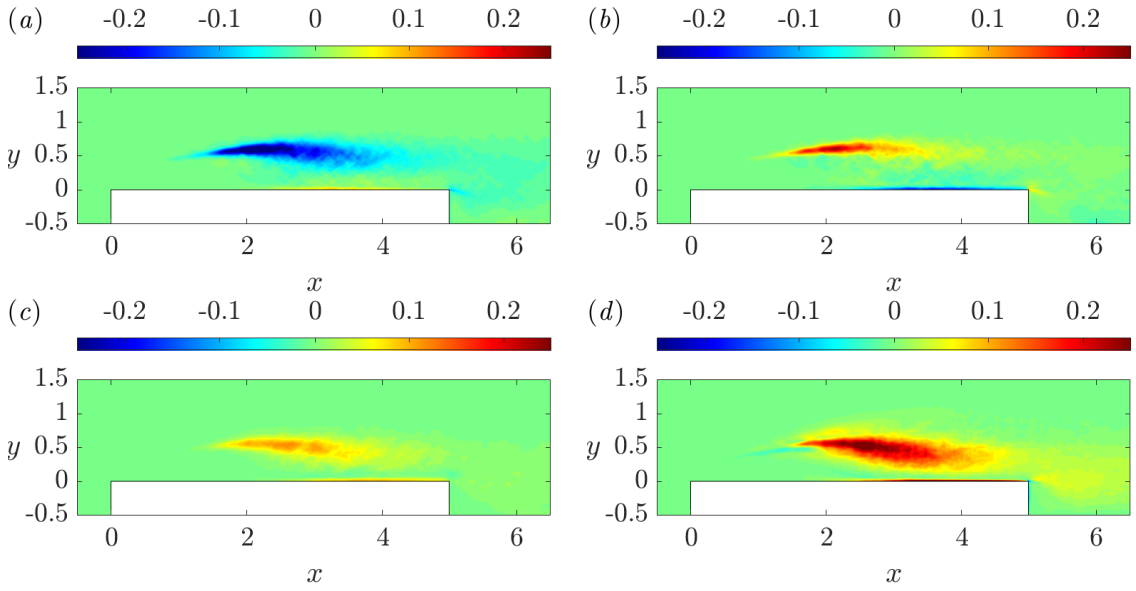

Figure 3.25. Distribution of the pressure-strain tensor Π_{ij} at $Re = 3000$. Pressure-strain terms of $\langle uu \rangle$ (a), $\langle vv \rangle$ (b), $\langle ww \rangle$ (c) and $\langle uv \rangle$ (d).

$$\mathcal{P}_{22} = -2\langle vv \rangle \frac{\partial \langle V \rangle}{\partial y} - 2\langle uv \rangle \frac{\partial \langle V \rangle}{\partial x}. \tag{3.15}$$

The first term on the right-hand side of the above equations is the contribution given by the product of stretching/compression of the mean flow with the normal Reynolds stresses, the second term is the contribution by the product of the mean shear with the Reynolds shear stress. By inspection of different contributions, in the leading-edge shear layer the production of $\langle uu \rangle$ is found to be driven by a compression of the mean flow, $\partial \langle U \rangle / \partial x < 0$, while the sink of $\langle vv \rangle$ is mainly due to a stretching of the mean flow, $\partial \langle V \rangle / \partial y > 0$. Indeed, according to the mean continuity equation $\partial \langle U \rangle / \partial x = -\partial \langle V \rangle / \partial y$, and hence stretching of the streamwise component occurs with compression of the vertical component, and vice versa. On the other hand, in the core of the main recirculating region the positive production of $\langle uu \rangle$ is driven by the mean vertical shear, $\partial \langle U \rangle / \partial y$, which is negatively correlated with the Reynolds shear stress, i.e. $\partial \langle U \rangle / \partial y > 0$ and $\langle uv \rangle < 0$ [24]. In the same region, the main driver found for the production of $\langle vv \rangle$ is the compression of the mean flow, $\partial \langle V \rangle / \partial y < 0$.

In the Reynolds-stress equations, the main effect of the fluctuating pressure is to redistribute energy among the components of the Reynolds stress tensor to reduce the anisotropy in the turbulent flow field. The redistributive effect of the fluctuating pressure is expressed by the pressure-strain tensor Π_{ij}, whose components are shown in figure 3.25 for the flow case at $Re_D = 3000$. It is recalled that the trace of the pressure-strain tensor is zero because of the incompressibility constraint, i.e. $\Pi_{11} + \Pi_{22} + \Pi_{33} = 0$, and Π_{ij} acts as a sink of energy for the deviatoric components of the Reynolds-stress tensor $(i \neq j)$. In most of the regions around the cylinder, negative values of Π_{11} occur together with positive values of Π_{22} and

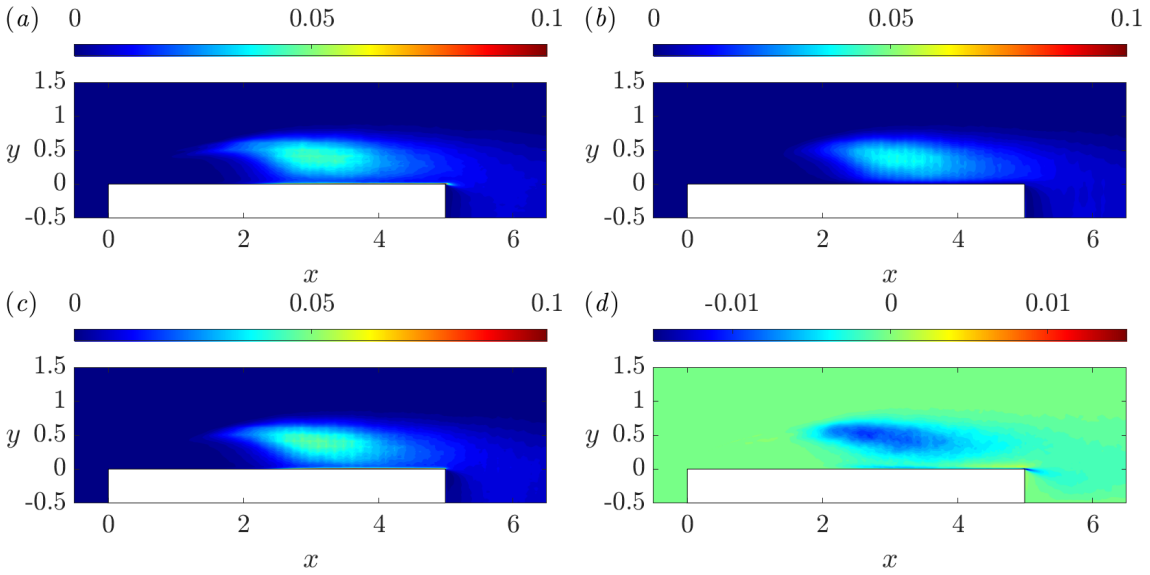

Figure 3.26. Distribution of the dissipation tensor $\langle\widetilde{\epsilon}\rangle_{ij}$ at $Re = 3000$. Dissipation terms of $\langle uu\rangle$ (a), $\langle vv\rangle$ (b), $\langle ww\rangle$ (c) and $\langle uv\rangle$ (d).

Π_{33}, thus indicating that energy is extracted from $\langle uu\rangle$ and transferred to $\langle vv\rangle$ and $\langle ww\rangle$. This redistribution of energy is significant in the leading-edge shear layer and in the core of the shedding region of the primary vortex. Along the shear layer $\Pi_{22} > \Pi_{33}$, which means that most of the energy provided by $\langle uu\rangle$ is gained by $\langle vv\rangle$. Contrarily, in the core of the primary vortex $\Pi_{22} < \Pi_{33}$ and energy is mainly given to $\langle ww\rangle$. In the region close to the wall, Π_{22} is negative while both Π_{11} and Π_{33} are positive. Owing to the impermeability constraint of the wall the vertical fluctuations are damped while the tangential fluctuations, $\langle uu\rangle$ and $\langle ww\rangle$, are amplified. This kind of event has been shown to be an important property of the turbulent flow in the vicinity of the walls and is known in the literature as splatting effect [87, 100]. In this region, energy is mainly redistributed to the spanwise fluctuations, i.e. $\Pi_{33} > \Pi_{11}$. The pressure-strain term Π_{12} is found to be a sink for $-\langle uv\rangle$ everywhere. The results on the pressure-strain terms agree with those reported by [24].

Figure 3.26 shows the non-zero components of the dissipation tensor $\langle\widetilde{\epsilon}\rangle_{ij}$. With regards to normal components, high values of dissipation are obtained along the shear layer and mostly in the shedding region of the primary vortex. For the streamwise and spanwise fluctuations, a further region of activity of viscous phenomena is identified in the proximity of the wall. As reported by Chiarini and Quadrio [24], also in the present work $\langle\widetilde{\epsilon}\rangle_{11}$ and $\langle\widetilde{\epsilon}\rangle_{33}$ exhibit larger values than $\langle\widetilde{\epsilon}\rangle_{22}$. The dissipation term of $\langle uv\rangle$ is mainly negative above the cylinder and its magnitude is negligible with respect to the other sink/source terms of the shear stress budget.

In closing the description of the terms of the Reynolds-stress transport equations at $Re_D = 3000$, figure 3.27 illustrates how the excess of each of the Reynolds stresses, represented

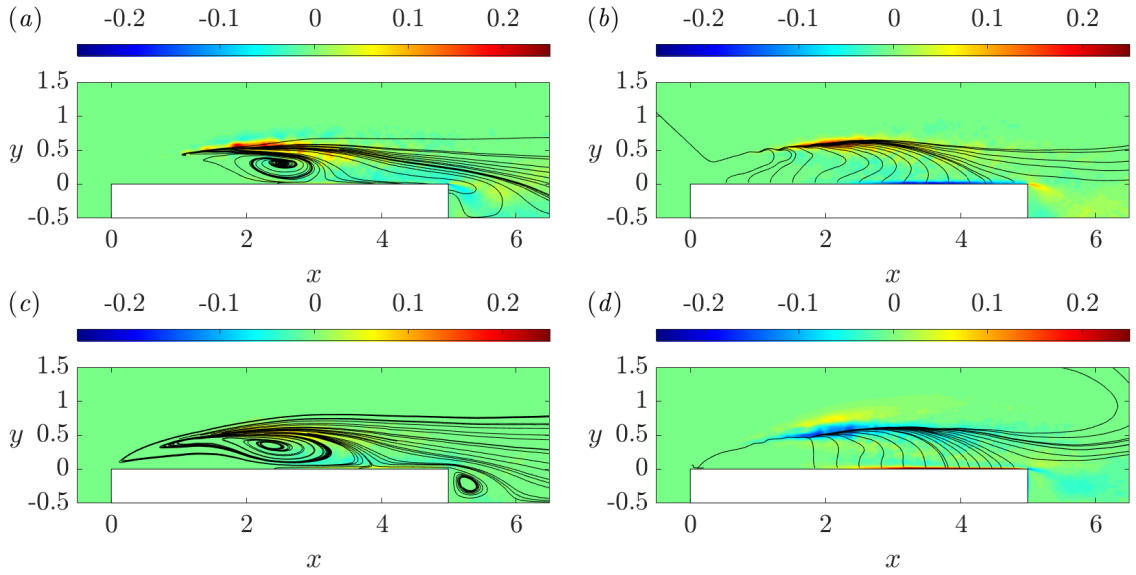

Figure 3.27. Cumulative source terms $\psi_{ij} = P_{ij} + \Pi_{ij} - \langle\widetilde{\epsilon}\rangle_{ij}$ superimposed with lines of the vector flux $\boldsymbol{\phi}_{ij}$ at $Re = 3000$. Source terms of $\langle uu\rangle$ (a), $\langle vv\rangle$ (b), $\langle ww\rangle$ (c) and $\langle uv\rangle$ (d).

by ψ_{ij}, is redistributed in the flow by means of transport mechanisms, following the patterns represented by the lines of the flux vector $\boldsymbol{\phi}_{ij}$. The excess of production of the normal Reynolds stresses and of $-\langle uv\rangle$ mainly occur along the leading-edge shear layer and in the shedding region of the primary recirculation bubble. The excess of $\langle uu\rangle$ is in the great part conveyed downstream towards the wake. The lines deviated downwards by the mean flow field do not cease directly on the wall, indicating that streamwise fluctuations are transported downstream through the forward boundary layer, where are gradually dissipated. Part of the lines originating from the shear layer is captured in the recirculating region induced by the main separation bubble and give rise to spiralling trajectories, similar to those evidenced for the fluxes of $\langle k\rangle$ in figure 3.19. Lines vanish at $(x, y) \approx (2.53, 0.30)$, thus slightly downstream than for $\langle k\rangle$. In Chiarini and Quadrio [24] this same point is found at $(x, y) \approx (2.1, 0.30)$. The excess of $\langle vv\rangle$ is partly transported downstream towards the wake and partly carried towards the wall. The region close to the wall is a sink of vertical turbulent fluctuations because of the large negative values of Π_{22} resulting from the turbulent flow impinging on the solid surface. The energy paths followed by the excess of $\langle ww\rangle$ resemble those for $\langle uu\rangle$, but the spiralling motions in the primary vortex have larger streamwise extents and reveal the reverse flow separation region [24]. Lines end at $(x, y) \approx (2.36, 0.33)$, while in Chiarini and Quadrio [24] $(x, y) \approx (2.06, 0.33)$ is reported. Besides the streamwise displacement, both the points are found upstream of the centre of rotation of the respective primary vortex. In the wake, spirals are also originated by the lines falling within the recirculating region of the wake vortex. Finally, the redistribution of the excess of the shear stress ψ_{12} is evaluated recalling that in the regions where $\langle uv\rangle$ is negative, $\psi_{12} < 0$ is a source of $-\langle uv\rangle$ while $\psi_{12} > 0$ is a

sink. The fluxes of $-\langle uv \rangle$ depart from the source regions located in the leading-edge shear layer and in the shedding region. Part of the energy is carried downstream towards the wake and another part is conveyed towards the cylinder wall, which acts as a sink for $-\langle uv \rangle$.

Flow at $Re_D = 8000$ and 14000

Before analysing the effects of the Reynolds number on the budget terms, variations in the distribution of the Reynolds stresses are examined. The components of the Reynolds-stress tensor are reported in figure 3.28 for the flow cases at $Re_D = 8000$ and 14000. Owing to the anticipation of the transitional process along the leading-edge shear layer, the regions of higher activity of the fluctuating velocity field are shifted upstream and stretched along the streamwise direction with increasing Reynolds number. The maximum value of $\langle uu \rangle$ is almost unaltered ($\langle uu \rangle_{\max} \approx 0.12$) and is found at $x = 1.38$ and $x = 0.79$ for the flow cases at $Re_D = 8000$ and 14000, respectively. Interestingly, for the other Reynolds stresses the intensity levels above the cylinder slightly decrease with the Reynolds number, even if the maximum values are almost equal ($\langle vv \rangle_{\max} \approx 0.07$ and $\langle ww \rangle_{\max} \approx 0.08$). However, as noted for $\tilde{E}_{\max}$ in figure 3.10, a mild rise of turbulent fluctuations is observed in the shedding region of the primary vortex by increasing the Reynolds number from 8000 to 14000. In the wake, the Reynolds stresses exhibit in general larger values in magnitude than for $Re_D = 3000$. This could suggest a strengthening of the large-scale shedding motion in the wake. In this region the highest values are reached by the vertical fluctuations, with a maximum value of $\langle vv \rangle_{\max} \approx 0.10$ close to the symmetry plane at $Re_D = 14000$.

The regions of positive values for the shear stress $\langle uv \rangle$ are limited to small areas in close proximity of the leading-edge and within the wake vortex, otherwise it is negative.

Production terms $\mathcal{P}_{ij}$ are reported in figure 3.29 for the flow cases at higher Reynolds numbers. By increasing the Reynolds number, the production of $\langle uu \rangle$ and the draining of $\langle vv \rangle$ along the leading-edge shear layer are enhanced. The fact that in the shear layer a major content of energy is removed from the vertical fluctuating field to sustain the mean field is argued to be at the basis of weak sensitivity on the Reynolds number exhibited by the thickness of the separation region. Indeed, as shown in §3.3.3, the main vortices in the separated region exhibit almost invariant vertical characteristics under different flow conditions. In the core of the shedding region, the production of both streamwise and vertical fluctuations is reduced while increasing the Reynolds number up to $Re_D = 14000$. In the wake, the vortex shedding instability is associated with mechanisms of production of $\langle vv \rangle$, which increases with the Reynolds number.

The influence of the Reynolds number on the different terms of the pressure-strain tensor is shown in figure 3.30. The growth of the Reynolds number leads to relevant variations in the magnitude of the energy redistribution process. In the shear layer a higher energy content is extracted from $\langle uu \rangle$ and provided to $\langle vv \rangle$ and $\langle ww \rangle$ than for $Re_D = 3000$. On

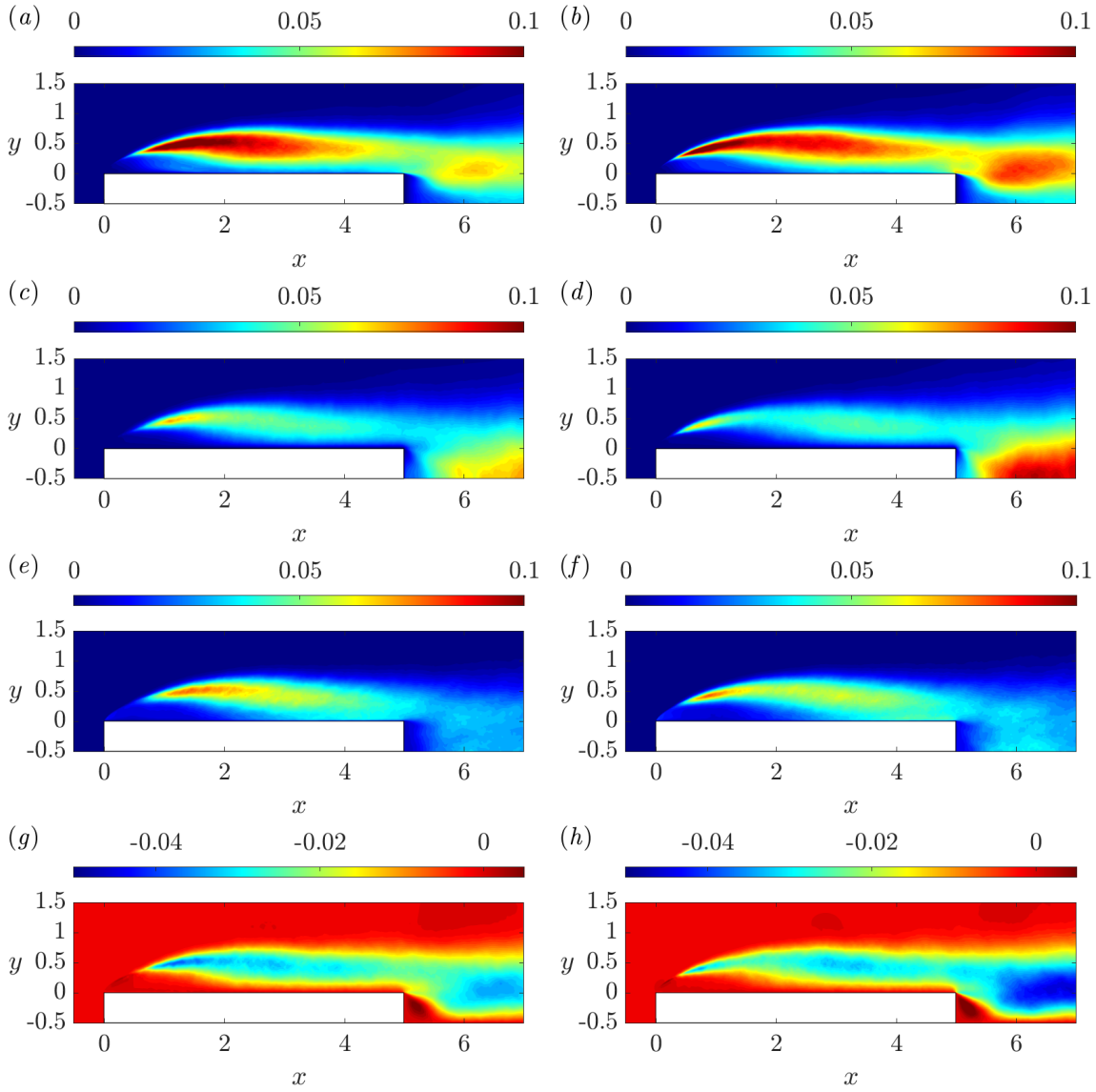

Figure 3.28. Distribution of the Reynolds stresses $\langle u_i u_j \rangle$ for the flow cases at $Re_D = 8000$ (left column) and $Re_D = 14000$ (right column). From top to bottom panels, streamwise (a,b), vertical (c,d), spanwise (e,f) and shear stresses (g,h), i.e. $\langle uu \rangle$, $\langle vv \rangle$, $\langle ww \rangle$, and $\langle uv \rangle$, respectively.

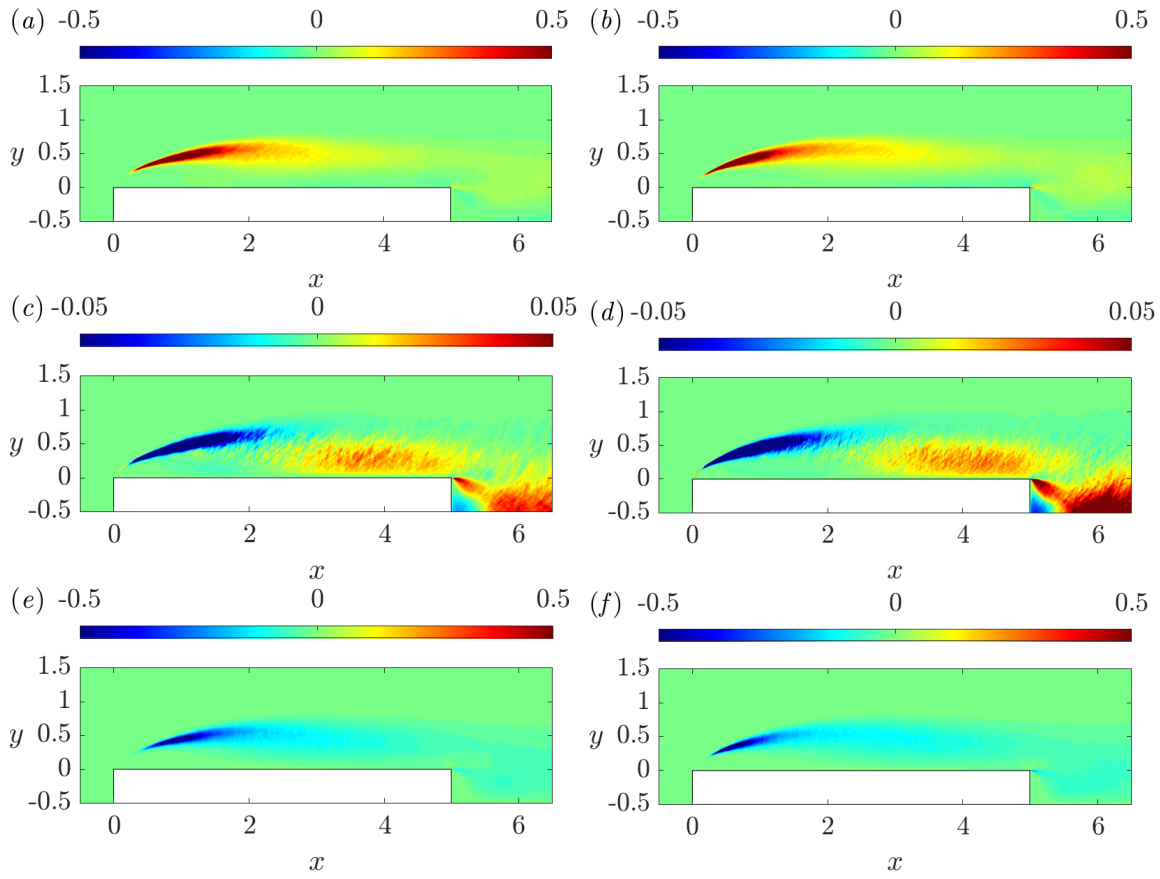

Figure 3.29. Production tensor $\mathcal{P}_{ij}$ for the flow cases at $Re_D = 8000$ (left column) and $Re_D = 14000$ (right column). From top to bottom panels, $\mathcal{P}_{11}$ (a,b), $\mathcal{P}_{22}$ (c,d) and $\mathcal{P}_{12}$ (e,f).

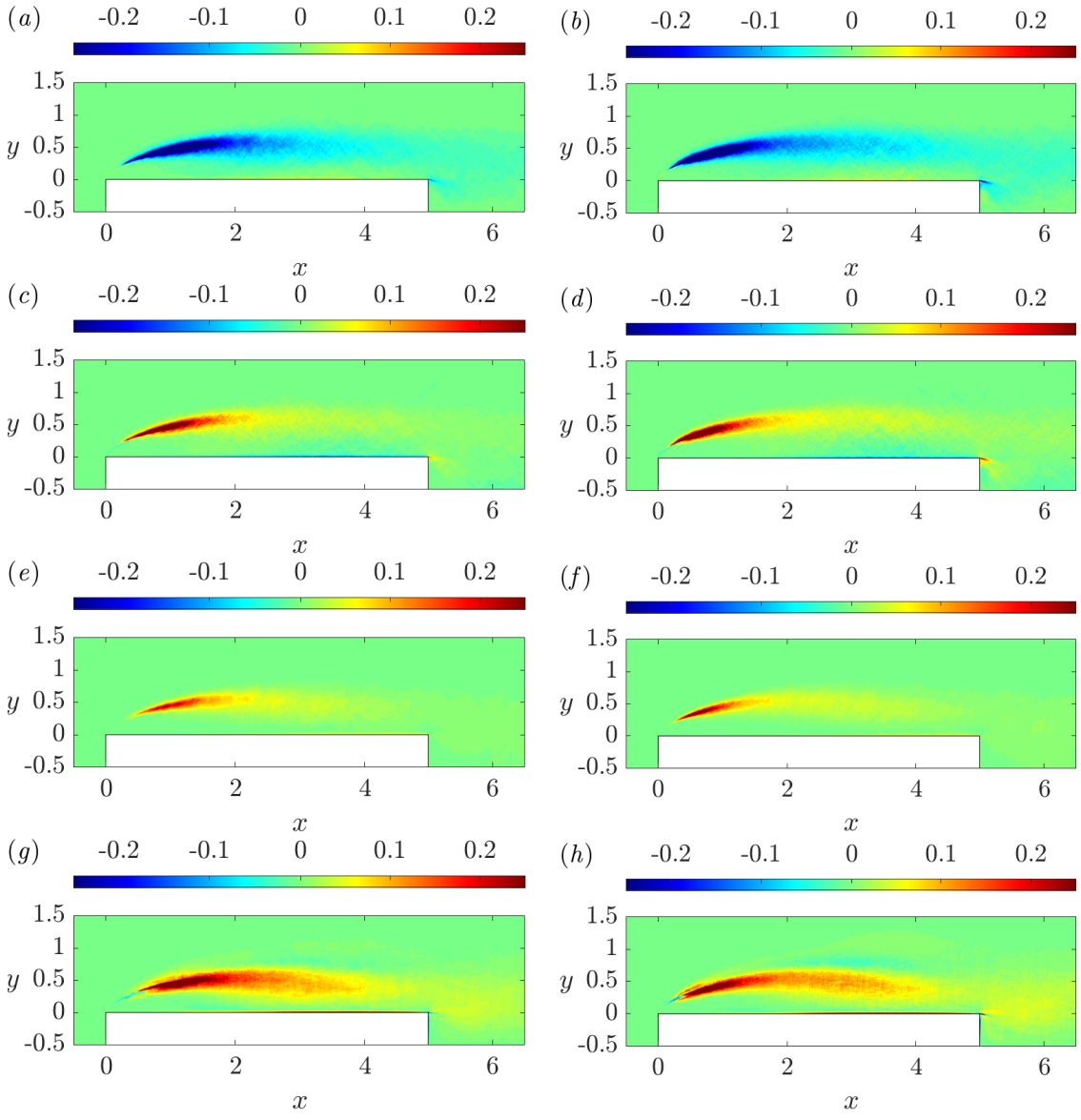

Figure 3.30. Pressure-strain tensor Π_{ij} for the flow cases at $Re_D = 8000$ (left column) and $Re_D = 14000$ (right column). From top to bottom panels, Π_{11} (a,b), Π_{22} (c,d), Π_{33} (e,f) and Π_{12} (g,h).

the other hand, in the vicinity of the wall the energy contribution drained from $\langle vv \rangle$ and redistributed to $\langle uu \rangle$ and $\langle ww \rangle$ is smaller. Actually, the high pressure-strain terms found close to the wall at $Re_D = 3000$ are related with the strong deceleration experienced by the fluid which impinges on the wall, as expressed by the curvature of the mean streamline paths. For the cases at higher Reynolds number, instead, the mean velocity patterns become flatter and the splatting effect produces less intense tangential velocity fluctuations.

Figure 3.31 shows the dissipation of the Reynolds stresses at $Re_D = 8000$ and 14000. As the Reynolds number increases, the region of maximum dissipation exhibits larger values in magnitude and moves further upstream along the leading-edge shear layer. This holds true for the dissipation term each of the Reynolds stresses.

Finally, the excesses of production of the Reynolds stresses ψ_{ij} together with lines of the vector flux are reported in figure 3.32. Source and sink regions along the leading-edge shear layer increases in magnitude with the Reynolds number. In accordance with the anticipation of the transitional processes shown at higher Reynolds numbers, the field lines of $\langle uu \rangle$ originate from a point located further upstream along the shear layer, i.e. $(x, y) \approx (0.25, 0.19)$ at $Re_D = 8000$ and $(0.15, 0.14)$ at $Re_D = 14000$. In addition, in the core of the primary vortex, the lines of $\langle uu \rangle$ form spiralling patterns that are more stretched along the longitudinal direction than for $Re_D = 3000$. Vertical fluctuations are mainly conveyed towards the wall. The marked curvature observed in the lines of $\langle vv \rangle$ within the primary recirculating region suggests that the transport mechanisms of vertical fluctuations are more affected by the streamwise velocity field than for $Re_D = 3000$. In the region close to the wall ψ_{22} acts as a sink term for vertical fluctuations but shows lower values in magnitude than for $Re_D = 3000$. This behaviour is essentially due to the pressure-strain term Π_{22} and its evolution with Re_D. The field lines of $\langle ww \rangle$ are mainly affected by the mean transport and highlight the upstream shift of the secondary vortex observed for increasing Reynolds number. The lines of $\langle uv \rangle$ cover larger streamwise distances before deflecting towards the wall than in the case at $Re_D = 3000$. In addition, starting from $Re_D = 8000$, lines also originate from a singularity point located slightly downstream than the centre of rotation of the main recirculating region, i.e. $(x, y) \approx (1.83, 0.28)$ at $Re_D = 8000$ and $(1.95, 0.29)$ at $Re_D = 14000$. At this stage of the work, the nature of this phenomenon has not been clarified yet and requires further investigation.

3.4 Conclusions

3.4.1 Influence of the spatial resolution

As highlighted by the BARC initiative, the flow around rectangular cylinders of chord-to-thickness ratio $c/D = 5$ is a complex case to tackle for numerical methods. The reason is the high sensitivity of the solution to boundary conditions, numerical method, and turbulence

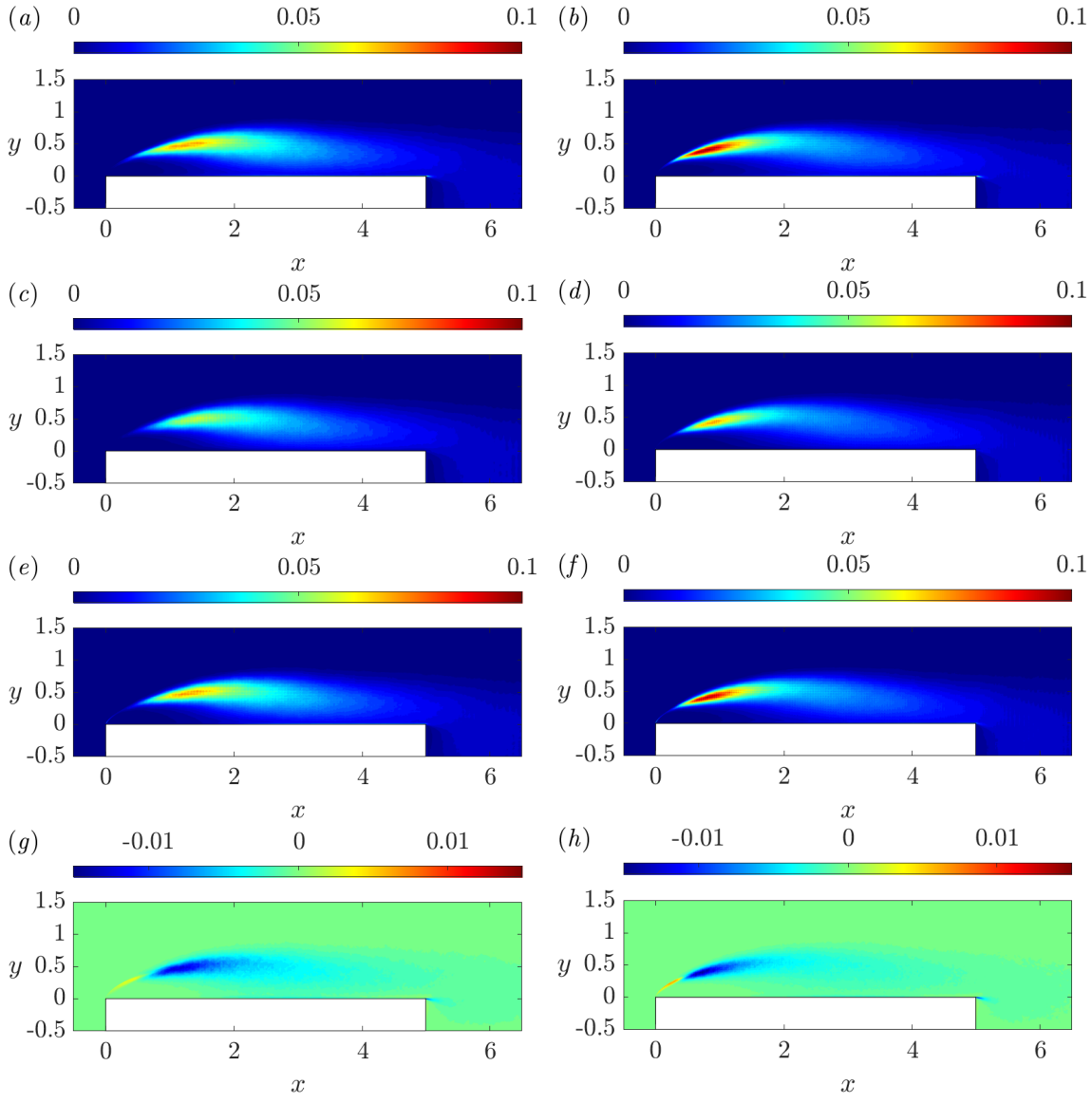

Figure 3.31. Dissipation tensor $\langle\widetilde{\epsilon}\rangle_{ij}$ for the flow cases at $Re_D = 8000$ (left column) and $Re_D = 14000$ (right column). From top to bottom panels, $\langle\widetilde{\epsilon}\rangle_{11}$ (a,b), $\langle\widetilde{\epsilon}\rangle_{22}$ (c,d), $\langle\widetilde{\epsilon}\rangle_{33}$ (e,f) and $\langle\widetilde{\epsilon}\rangle_{12}$ (g,h).

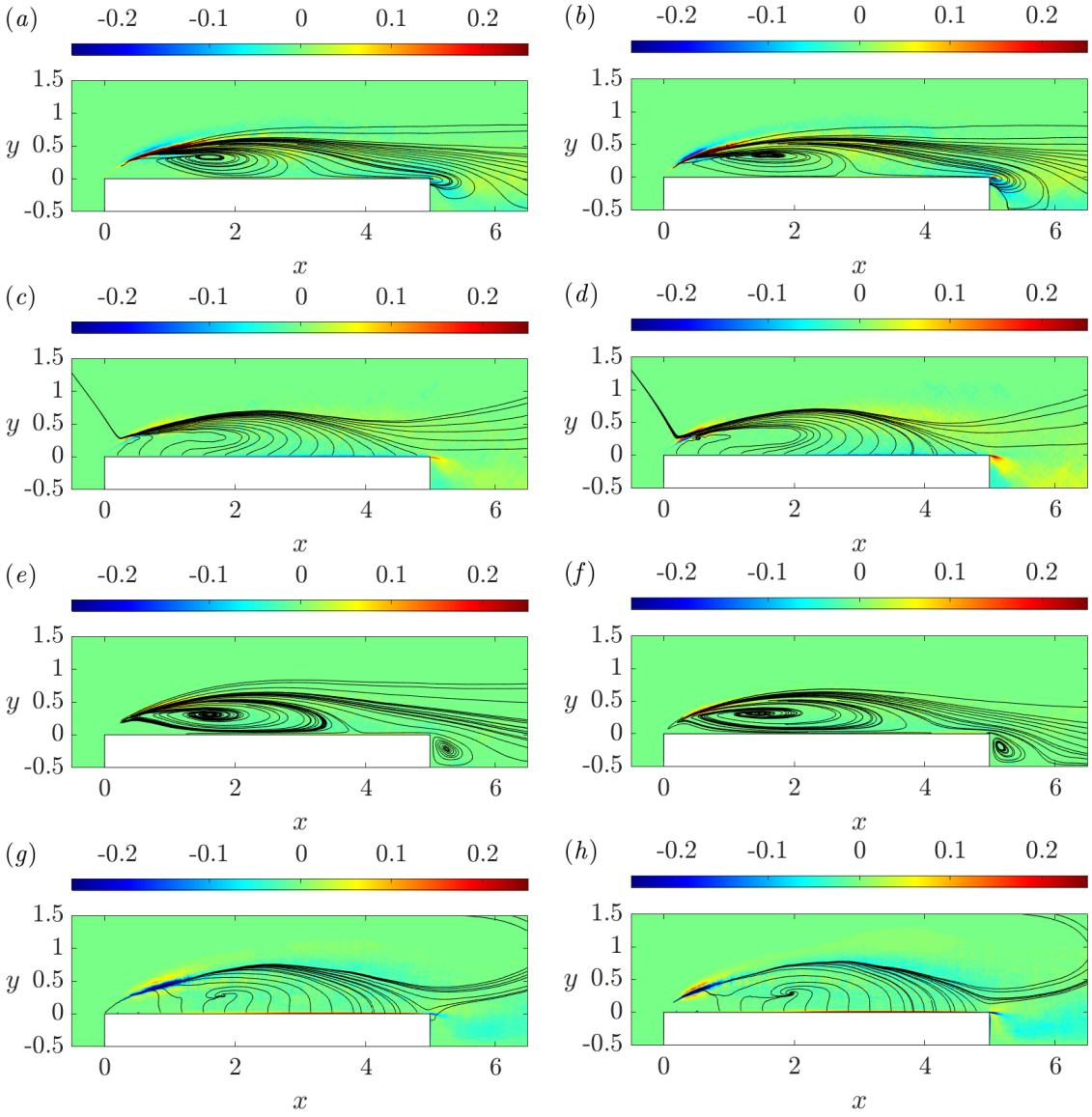

Figure 3.32. Cumulative source terms $\psi_{ij} = \mathcal{P}_{ij} + \Pi_{ij} - \langle\widetilde{\epsilon}\rangle_{ij}$ superimposed with lines of the vector flux $\boldsymbol{\phi}_{ij}$ for the flow cases at $Re_D = 8000$ (left column) and $Re_D = 14000$ (right column). From top to bottom panels, ψ_{11} (a,b), ψ_{22} (c,d), ψ_{33} (e,f) and ψ_{12} (g,h).

closure. In the present work, the flow solution of well resolved DNS at $Re_D = 3000$ is presented and compared to two previous simulations of the same flow case and at the same Reynolds number [27, 24]. Despite these three simulations differ in several numerical aspects such as domain size, temporal resolution, time-integration period, accuracy of the numerical schemes, and spatial resolution, a heuristic analysis suggests that the main differences between the flow solutions can be ascribed to the different spatial resolution employed.

An outcome of this work is that the DNS results of the aerodynamics of the BARC rectangular cylinder is very sensitive to the level of spatial resolution and that the simulations at $Re_D = 3000$ display marked differences, despite all the three simulations were conceived for providing results beyond numerical convergence. It appears that by decreasing the resolution level, the recirculating flow dynamics moves upstream of a significant amount, but almost retaining its distance from the solid wall. For decreasing resolution also the intensity of pressure and velocity fluctuations decreases. In the present work, the ratio between grid spacings far from the solid walls and the Kolmogorov scale, see figure 3.14, and also the mesh size values expressed in terms of wall units, see figure 3.13, suggest that the simulation should be close to fully resolved. However, given results presented here are currently not supported by simulations conducted by other groups at higher accuracy, the question is still open.

The separating and reattaching flow in rectangular cylinders is characterised by a number of different flow mechanisms that contribute to the overall dynamics and require specific resolution criteria. Directions are identified for grid generation in two important regions of the flow i) the forward/reverse boundary layers and ii) the free turbulent flow.

i Boundary layers. The resolution requirement for the streamwise direction is stricter than in wall-bounded flows, especially in the flow reattachment region. On the contrary, the resolution requirements in the vertical and spanwise directions are almost unaltered with respect to the common practice in wall turbulence. As a result, the suggested grid spacings in wall units are $\Delta x^+_{\max} \approx 4$, $\Delta y^+_{w\,\max} \approx 0.5$ and $\Delta z^+_{\max} \approx 4$.

ii Free turbulence. Due to the high curvature of the mean streamlines at the body sides, the resolution requirement along the streamwise direction should not be relaxed as it is commonly done in more classical planar free-shear flows, therefore grid spacing should be close to isotropic. Recommended grid spacings in the free flow regions where transitional and fully turbulent mechanisms are present is $(\Delta x/\eta)_{\max} = (\Delta y/\eta)_{\max} = (\Delta z/\eta)_{\max} \approx 4$.

The discussion assumes that differences between the flow solutions compared can be entirely ascribed to the different spatial resolution. Other possible effects are disregarded. The above criteria should be considered as a first attempt towards the definition of a set of guidelines for grid generation about bluff bodies involving separation at sharp corners and reattachment. A more rigorous analysis where one single numerical method is used and

the spatial resolution is varied along one single direction at a time is needed to verify these conjectures.

3.4.2 Influence of the Reynolds number

In the present work DNSs of the flow around the rectangular cylinder with $c/D = 5$ are conducted at increasing values of the Reynolds number, from $Re_D = 3000$ to 14000. Within this range the Reynolds number is shown to considerably affect the turbulent characteristics of the separating and reattaching flow. The most evident effect of the Reynolds number is the anticipated transition to turbulence in the leading-edge shear layer. As revealed by the visualizations of vortical structures through λ_2-criterion, the disturbances introduced by instability mechanisms in the first part of the shear layer are amplified with higher strength with the Reynolds number. Accordingly, spanwise rolls of smaller thickness evolve in hairpin-like structures at more upstream distances from the separation line and vortices of smaller scale are formed in the turbulent flow downstream.

The main global statistics of the flow show slight variations as a function of the Reynolds number, except for $c_{\mathrm{l,\,rms}}$ which gradually increases with Re_D. This is explained by a greater imbalance between the low-pressure regions on the opposite sides of the cylinder. The vortex shedding frequency slowly approaches the value $St \approx 0.11$, corresponding to a vortex shedding period of about $9D/U_\infty$, and which is in agreement with values measured at Reynolds numbers up to 10^5 [109, 91]. Frequency spectra evaluated along the leading-edge shear layer show that fluctuations of higher frequencies are excited in the transitional process with increasing Reynolds number. Hence, a larger separation of scales between large-scale shedding unsteadiness and turbulence is attained by increasing Re_D. Moreover, the identification of a secondary peak at lower frequencies suggests that the vortex shedding instability still influences the leading-edge shear layer at $Re_D = 14000$.

The recirculating flow dynamics is affected by variations of the Reynolds number. An increment of the Reynolds number induces the upstream shift of the centres of rotation of the three primary recirculating regions. The main differences are noted between the flow cases at $Re_D = 3000$ and $Re_D = 8000$, and the higher sensitivity to the flow conditions is expressed by the secondary bubble, as visible in figure 3.8. The latter phenomenon is related with turbulent fluctuations of increasing intensity in the reverse boundary layer which makes the separated flow less prone to separation under adverse pressure gradient conditions. The occurrence of negative turbulent production phenomena in the shear layer makes the thickness of the primary bubble almost insensitive to the Reynolds number. From the inspection of the production of $\langle vv \rangle$ under different Re_D values, it is found that an increasing contribution of energy is drained from the vertical fluctuating field to sustain the mean vertical field. By raising the Reynolds number from 3000 to 14000, the reattachment length is observed to increase. This phenomenon, apparently in contrast with predictions by Mannini et al. [80]

and Moore et al. [91], may suggest the existence of a range of Reynolds numbers, occurring after the onset of transition in the separated shear layer, characterized by first a decrease in the reattachment length, then a slow increase, up to $Re_D \sim 10^4$. Similar behaviours have been already documented for the backward-facing step flow [47, 5, 2] and bluff flat plate flow [97] at comparable Reynolds numbers.

The anticipation of transitional processes in the leading-edge shear layer leads to significant variations in the distribution of the turbulent kinetic energy. The regions of highest turbulence intensity move from the wake region of the primary vortex, at $Re_D = 3000$, to upstream locations along the leading-edge shear layer, at higher Reynolds numbers. The maximum value of $\langle k \rangle$ slightly changes with Re_D. As revealed by the analysis of one-dimensional spectra of the turbulent kinetic energy, a clear separation between energy-containing and dissipative fluctuations, accompanied by a well-defined $-5/3$ spectrum, is obtained only for Reynolds number of the order $\sim 10^4$.

The effects of the Reynolds number on the terms of turbulent kinetic energy budgets and Reynolds-stresses budgets have been evaluated. The regions of maximum intensity of these terms are generally shifted towards upstream positions along the leading-edge shear layer as the Reynolds number increases. Along the leading-edge shear layer, the production and dissipation of turbulent kinetic energy increase in magnitude with the Reynolds number. In the near wall region, instead, the dissipation shows the largest values at $Re_D = 3000$. In the flow cases examined the lines of energy fluxes show a similar distribution around the rectangular cylinder, the exception being the core of the primary vortex. There, the lines form spiralling motions which become increasingly stretched along the streamwise direction with the Reynolds number. Furthermore, since the transport mechanisms of turbulent kinetic energy are less intense than in the shear layer and close to the wall, this region is regarded as weakly active. The largest values of the pressure-strain terms close to the wall are found at $Re_D = 3000$, thus suggesting that the splatting effect induced by the flow impinging on the wall decreases with the Reynolds number.

Concluding remarks

In the present work, Direct Numerical Simulation approach is used to obtain high-order accurate, detailed results of two turbulence problems of interest in the research field. The aims include providing further insight on the fundamental physical processes involved and contributing to the development and validation of turbulence models for engineering applications. The flow cases investigated are the turbulence generated by an irregular porous matrix, represented by a realistic open-cell metal foam, and the aerodynamics of rectangular cylinder with chord-to-thickness ratio $c/D = 5$. The former is studied in grid turbulence context and deals with decaying homogeneous isotropic turbulence which is obtained, with a certain degree of approximation, downstream of the metal foam. The interest in this topic lies in the potential description of the sufficiently small-scale fluctuations of any turbulent flow with very high Reynolds number. The analysis is conducted for a single Reynolds number $Re_{d_p} = 4000$, corresponding to a Taylor-scale Reynolds number $Re_\lambda \approx 80$, and for a foam of porosity $\varepsilon = 0.92$, but the effects of a different porosity are also considered in the appendix A. The second flow case has been recently established as a benchmark for the study of separating and reattaching flows under the name of BARC [8] and represents a challenge for numerical predictions based on turbulence modelling techniques. Within this framework, the Reynolds number effects are addressed for the first time at Reynolds number values up to the order $\sim 10^4$ by using a numerical approach free of turbulence models. Three direct simulations of the turbulent flow are performed at $Re_D = 3000$, 8000 and 14000. Through the comparison between the results obtained and data from previous DNS investigations conducted at $Re_D = 3000$ [27, 24], a first attempt is also made in the study of the influence of spatial resolution in the DNS of flows around elongated rectangular cylinders with sharp corners.

The DNSs are performed using two different open-source codes based on high-order discretisation procedures. In particular, *Incompact3d* based on sixth-order finite-difference method is used for the simulation of grid turbulence case, while *Nek5000* based on spectral element method with polynomials of order $N = 7$ is used for the simulations of the BARC configuration. The use of high-order methods combined with a sufficiently fine mesh grid can enable a satisfactory representation of turbulent motions over the range of length scales.

This is deemed important at the Reynolds numbers under consideration, where a significant scale separation starts to emerge; see figures 2.22 and 3.16(d).

The statistical analysis of turbulence generated by the open-cell metal foam reveals that typical characteristics of decaying homogeneous isotropic turbulence are obtained at shorter distances from the foam than for classical and fractal grid turbulence. Closer to the foam ($x < 2$), pressure and turbulent transport of turbulent kinetic energy are non-negligible and provide negative and positive contribution (upstream and downstream transport of energy), respectively. In the same region, Re_λ undergoes a steep decrease whereas the dissipation coefficient C_ϵ increases like Re_λ^{-1}. With respect to Valente and Vassilicos [119], the unusual C_ϵ behaviour is here associated to the close proximity to the foam and the occurrence of significant turbulent transport processes. At larger distances from the porous layer, in the developed region ($x > 8$), the classical grid turbulence situation is recovered, where the mean advection of turbulent kinetic energy equals dissipation. This entails a power-law decay of turbulent quantities and characteristic lengths. The least-square fitted exponents agree with values predicted and measured in classical grid turbulence experiments. In particular, the decay exponent of turbulent kinetic energy is $n_k = 1.14$, while those of integral, Taylor and Kolmogorov scales are close to one-half, thus indicating that the turbulence simulated here differs from Saffman turbulence. Analysis of the scaling exponents of structure functions and the decorrelation length of dissipation suggests that small-scale fluctuations are weakly intermittent at the Reynolds number examined. Results change only quantitatively but not qualitatively for a foam with higher porosity, i.e. $\varepsilon = 0.97$.

The BARC flow configuration shows a significant sensitivity to the Reynolds number in the range between $Re_D = 3000$ and 14000. Perturbations initiated by Kelvin-Helmholtz instabilities are subjected to higher amplification rate with Re_D, thus leading to a more rapid break down to turbulence in the leading-edge shear layer. Accordingly, the peak of turbulent kinetic energy is reached in the wake region of the primary vortex at $Re_D = 3000$ ($x_k = 3.09$) and moves toward upstream positions along the shear layer at higher Re_D (up to $x_k = 0.78$ at $Re_D = 14000$). The Reynolds number slightly affects the vortex shedding frequency, which mildly approaches $St \simeq 0.11$, and enhances the amplitude of lift coefficient oscillations. With regards to mean flow topology, the rotating centres of the three main separation bubbles are shifted upstream, while the reattachment length slightly increases. This latter trend appears in conflict with that reported in the literature about BARC for $Re_D > 10^4$ [80, 91], but resembles the behaviour already observed for the backward-facing step flow and bluff flat plate flow at Reynolds numbers close to those considered here [5, 97]. The larger upstream displacements are observed for the secondary bubble because of the less predisposition to separation shown by the reverse flow with increasing Re_D. Negative production phenomena taking place in the leading-edge shear layer are at the basis of the weak dependence between the mean vertical velocity and the Reynolds number. The BARC flow configuration also shows high sensitivity to the level of spatial resolution. From the comparison with previous

DNS studies [27, 24], by ascribing all the main discrepancies to the different grid spacings, emerges that by lowering the resolution level, especially in the streamwise direction, the recirculating flow dynamics is shifted upstream and turbulent fluctuations are reduced. While a more rigorous analysis is envisaged, where the order of accuracy of the schemes are kept the same while grid spacings are varied alternately along each spatial direction, directions for grid generation in the regions of forward/reverse boundary layers and free turbulence are identified.

In conclusion, the present work provides two sets of highly accurate DNS data representative of two turbulence problems of scientific relevance. These results constitute a valuable base of information that might improve our current understanding of decaying homogeneous isotropic turbulence and separating and reattaching flows, and lead to the development of turbulence models of greater accuracy and wider applicability, both in the RANS and LES context.

The study of the turbulence generated by an open-cell metal foam has been presented at two conferences [36, 37] and published in two international journals [38, 35]. With regards to the investigation on the aerodynamics of the rectangular cylinder with $c/D = 5$, two papers on the flow case at $Re_D = 3000$ have been recently published in an international journal [39, 34].

References

[1] Abdalla, I. E. and Yang, Z. (2004). Numerical study of the instability mechanism in transitional separating-reattaching flow. *International Journal of Heat and Fluid Flow*, 25:593–605.

[2] Adams, E. W. and Johnston, J. P. (1988). Effects of the separating shear layer on the reattachment flow structure part 2: Reattachment length and wall shear stress. *Experiments in Fluids*, 154:493–499.

[3] Alves Portela, F., Papadakis, G., and Vassilicos, J. (2017). The turbulence cascade in the near wake of a square prism. *J. Fluid Mech.*, 825:315–352.

[4] Anderson, J. D. (2011). *Fundamentals of Aerodynamics*. McGraw-Hill, 5th edition.

[5] Armaly, B. F., Durst, F., Pereira, J. C. F., and Schönung, B. (1983). Experimental and theoretical investigation of backward-facing step flow. *J. Fluid Mech.*, 127:473–496.

[6] Arslan, T., Pettersen, B., and Andersson, H. (2011). Calculations of the flow around rectangular shaped floating structures. In *Proceedings of the Thirteenth International Conference on Wind Engineering*, Amsterdam, The Netherlands.

[7] August, A., Ettrich, J., Rölle, M., Schmid, S., Berghoff, M., Selzer, M., and Nestler, B. (2015). Prediction of heat conduction in open-cell foams via the diffuse interface representation of the phase-field method. *International Journal of Heat and Mass Transfer*, 84:800–808.

[8] Bartoli, G., Bruno, L., Cimarelli, A., Mannini, C., Patruno, L., Ricciardelli, F., and Salvetti, M. (2020). Barc overview document. Available at http://www.aniv-iawe.org/barc.

[9] Batchelor, G. K. (1948). Energy decay and self-preserving correlation functions in isotropic turbulence. *Quarterly of Applied Mathematics*, 6:97–116.

[10] Batchelor, G. K. and Townsend, A. A. (1948). Decay of isotropic turbulence in the initial period. *Proceedings of the Royal Society of London. Series A. Mathematical and Physical Sciences*, 193:539–558.

[11] Benzi, R., Ciliberto, S., Tripiccione, R., Baudet, C., Massaioli, F., and Succi, S. (1993). Extended self-similarity in turbulent flows. *Phys. Rev. E*, 48:R29–R32.

[12] Bloor, M. (1964). The transition to turbulence in the wake of a circular cylinder. *J. Fluid Mech.*, 19:290–304.

[13] Bloor, M. S., Gerrard, J. H., and Lighthill, M. J. (1966). Measurements on turbulent vortices in a cylinder wake. *Proceedings of the Royal Society of London. Series A. Mathematical and Physical Sciences*, 294(1438):319–342.

[14] Bonnavion, G. and Cadot, O. (2018). Unstable wake dynamics of rectangular flat-backed bluff bodies with inclination and ground proximity. *J. Fluid Mech.*, 854:196–232.

[15] Boomsma, K., Poulikakos, D., and Ventikos, Y. (2003). Simulations of flow through open cell metal foams using an idealized periodic cell structure. *International Journal of Heat and Fluid Flow*, 24:825–834.

[16] Boratav, O. N. and Pelz, R. B. (1997). Structures and structure functions in the inertial range of turbulence. *Physics of Fluids*, 9:1400–1415.

[17] Bruno, L., Coste, N., and Fransos, D. (2012). Simulated flow around a rectangular 5:1 cylinder: spanwise discretization effects and emerging flow features. *J. Wind Eng. Ind. Aerodyn.*, 104:203–215.

[18] Bruno, L., Fransos, D., Coste, N., and Bosco, A. (2010). 3d flow around a rectangular cylinder: a computational study. *J. Wind Eng. Ind. Aerodyn.*, 98:263–276.

[19] Bruno, L., Salvetti, M., and Ricciardelli, F. (2014). Benchmark on the aerodynamics of a rectangular 5:1 cylinder: An overview after the first four years of activity. *J. Wind Eng. Ind. Aerodyn.*, 126:87–106.

[20] Calmidi, V. V. and Mahajan, R. L. (2000). Forced convection in high porosity metal foams. *Journal of Heat Transfer*, 122:557–565.

[21] Camussi, R., Barbagallo, D., Guj, G., and Stella, F. (1996). Transverse and longitudinal scaling laws in non-homogeneous low re turbulence. *Physics of Fluids*, 8:1181–1191.

[22] Canuto, C., Hussaini, M., Quarteroni, A., and Thomas A., J. (2012). *Spectral Methods in Fluid Dynamics*. Springer Science & Business Media.

[23] Cao, Y., Tamura, T., and Kawai, H. (2020). Spanwise resolution requirements for the simulation of high-reynolds-number flows past a square cylinder. *Computers & Fluids*, 196:104320.

[24] Chiarini, A. and Quadrio, M. (2021). The turbulent flow over the barc rectangular cylinder: a dns study. *Flow, Turbulence and Combustion*.

[25] Chovet, C., Keirsbulck, L., Lippert, M., and Foucaut, J. (2017). Unsteady behaviour of separated and reattaching flows for a backward-facing step configuration at high reynolds numbers. In de Mécanique, A. F., editor, *CFM 2017 - 23ème Congrès Français de Mécanique*.

[26] Cimarelli, A., Franciolini, M., and Crivellini, A. (2020). Numerical experiments in separating and reattaching flows. *Phys. Fluids*, 32:095119.

[27] Cimarelli, A., Leonforte, A., and Angeli, D. (2018a). Direct numerical simulation of the flow around a rectangular cylinder at a moderately high reynolds number. *J. Wind Eng. Ind. Aerodyn.*, 174:38–49.

[28] Cimarelli, A., Leonforte, A., and Angeli, D. (2018b). On the structure of the self-sustaining cycle in separating and reattaching flows. *J. Fluid Mech.*, 857:907–936.

[29] Cimarelli, A., Leonforte, A., De Angelis, E., Crivellini, A., and Angeli, D. (2019a). On negative turbulence production phenomena in the shear layer of separating and reattaching flows. *Physics Letters A*, 383:1019–1026.

[30] Cimarelli, A., Leonforte, A., De Angelis, E., Crivellini, A., and Angeli, D. (2019b). Resolved dynamics and subgrid stresses in separating and reattaching flows. *Phys. Fluids*, 31:095101.

[31] Coleman, G. and Sandberg, R. (2010). A primer on direct numerical simulation of turbulence - methods, procedures and guidelines. Technical report, University of Southampton.

[32] Comte-Bellot, G. and Corrsin, S. (1966). The use of a contraction to improve the isotropy of grid-generated turbulence. *J. Fluid Mech.*, 25:657–682.

[33] Comte-Bellot, G. and Corrsin, S. (1971). Simple eulerian time correlation of full- and narrow-band velocity signals in grid-generated, 'isotropic' turbulence. *J. Fluid Mech.*, 48:273–337.

[34] Corsini, R., Angeli, D., Stalio, E., Chibbaro, S., and Cimarelli, A. (2022). Flow solutions around rectangular cylinders: the question of spatial discretization. *Wind and Structures*, 34:151–159.

[35] Corsini, R., Fregni, A., Spinolo, M., and Stalio, E. (2021). On the turbulent flow past a realistic open-cell metal foam. *J. Fluid Mech.*, 920:A9.

[36] Corsini, R. and Stalio, E. (2019a). Talk: Direct numerical simulation of turbulence past an open cell aluminum foam. *37th UIT Heat Transfer Conference*, 24-26 June, Padova, Italy.

[37] Corsini, R. and Stalio, E. (2019b). Talk: On the turbulent wake behind a high porosity metal foam. *74° Congresso Nazionale ATI*, 11-13 September, Modena, Italy.

[38] Corsini, R. and Stalio, E. (2020). Direct numerical simulation of turbulence in the wake of a metal foam. *Int. Commun. Heat Mass Transf.*, 115:104599.

[39] Crivellini, A., Nigro, A., Colombo, A., Ghidoni, A., Noventa, G., Cimarelli, A., and Corsini, R. (2022). Implicit large eddy simulations of a rectangular 5:1 cylinder with a high-order discontinuous galerkin method. *Wind and Structures*, 34:59–72.

[40] Deville, M., Fischer, P., and Mund, E. (2002). *High-Order Methods for Incompressible Fluid Flow*. Cambridge University Press.

[41] Fischer, P. (1997). An overlapping schwarz method for spectral element solution of the incompressible navier-stokes equations. *J. Comput. Physics*, 133:84–101.

[42] Fischer, P., Lottes, J., and Kerkemeier, S. (2008). Nek5000 webpage. http://nek5000.mcs.anl.gov.

[43] Fischer, P. and Mullen, J. (2001). Filter-based stabilization of spectral element methods. *Comptes Rendus de l'Académie des Sciences - Series I - Mathematics*, 332:265–270.

[44] Frisch, U., Sulem, P., and Nelkin, M. (1978). A simple dynamical model of intermittent fully developed turbulence. *J. Fluid Mech.*, 87:43–164.

[45] Gautier, R., Laizet, S., and Lamballais, E. (2014). A dns study of jet control with microjets using an immersed boundary method. *International Journal of Computational Fluid Dynamics*, 28:393–410.

[46] George, W. K. (1992). The decay of homogeneous isotropic turbulence. *Physics of Fluids A*, 4:1492–1509.

[47] Goldstein, R. J., Eriksen, V. L., Olson, R. M., and Eckert, E. R. G. (1970). Laminar separation, reattachment, and transition of the flow over a downstream-facing step. *Journal of Basic Engineering*, 92:732–739.

[48] Gomes-Fernandes, R., Ganapathisubramani, B., and Vassilicos, J. C. (2012). Particle image velocimetry study of fractal-generated turbulence. *J. Fluid Mech.*, 711:306–336.

[49] Goto, S. and Vassilicos, J. C. (2016). Unsteady turbulence cascades. *Phys. Rev. E*, 94:053108.

[50] Gotoh, T., Fukayama, D., and Nakano, T. (2002). Velocity field statistics in homogeneous steady turbulence obtained using a high-resolution direct numerical simulation. *Physics of Fluids*, 14:1065–1081.

[51] Gottlieb, D. and Orszag, S. (1977). *Numerical Analysis of Spectral Methods: Theory and Applications*. SIAM.

[52] Grossmann, S., Lohse, D., and Reeh, A. (1997). Different intermittency for longitudinal and transversal turbulent fluctuations. *Physics of Fluids*, 9:3817–3825.

[53] Hearst, R. J. and Lavoie, P. (2014). Decay of turbulence generated by a square-fractal-element grid. *J. Fluid Mech.*, 741:567–584.

[54] Hosseini, S., Vinuesa, R., Schlatter, P., Hanifi, A., and Henningson, D. (2016). Direct numerical simulation of the flow around a wing section at moderate reynolds number. *International Journal of Heat and Fluid Flow*, 61:117–128.

[55] Hourigan, K., Thompson, M., and Tan, B. (2001). Self-sustained oscillations in flows around long blunt plates. *Journal of Fluids and Structures*, 15:387–398.

[56] Hurst, D. and Vassilicos, J. C. (2007). Scalings and decay of fractal-generated turbulence. *Physics of Fluids*, 19:035103.

[57] Isaza, J. C., Salazar, R., and Warhaft, Z. (2014). On grid-generated turbulence in the near- and far field regions. *J. Fluid Mech.*, 753:402–426.

[58] Iyer, K. P., Sreenivasan, K. R., and Yeung, P. K. (2017). Reynolds number scaling of velocity increments in isotropic turbulence. *Phys. Rev. E*, 95:021101.

[59] Jeong, J. and Hussain, F. (1995). On the identification of a vortex. *J. Fluid Mech.*, 285:69–94.

[60] Jeong, J., Hussain, F., Schoppa, W., and Kim, J. (1997). Coherent structures near the wall in a turbulent channel flow. *J. Fluid Mech.*, 332:185–214.

[61] Jimenez, J. (1983). A spanwise structure in the plane shear layer. *J. Fluid Mech.*, 132:319–336.

[62] Karniadakis, G. and Sherwin, S. (1999). *Spectral/hp Element Methods for Computational Fluid Dynamics*. Oxford University Press.

[63] Kim, J., Moin, P., and Moser, R. (1987). Turbulence statistics in fully developed channel flow at low reynolds number. *J. Fluid Mech.*, 177:133–166.

[64] Kitamura, T., Nagata, K., Sakai, Y., Sasoh, A., Terashima, O., Saito, H., and Harasaki, T. (2014). On invariants in grid turbulence at moderate reynolds numbers. *J. Fluid Mech.*, 738:378–406.

[65] Kiya, M. and Sasaki, K. (1983). Structure of a turbulent separation bubble. *J. Fluid Mech.*, 137:83–113.

[66] Kiya, M. and Sasaki, K. (1985). Structure of large-scale vortices and unsteady reverse flow in the reattaching zone of a turbulent separation bubble. *J. Fluid Mech.*, 154:463–491.

[67] Kolmogorov, A. N. (1941a). Dissipation of energy in the locally isotropic turbulence. *Dokl. Akad. Nauk SSSR*, 32:16–18.

[68] Kolmogorov, A. N. (1941b). The local structure of turbulence in incompressible viscous fluid for very large reynolds numbers. *Akademiia Nauk SSSR Doklady*, 30:301–305.

[69] Kolmogorov, A. N. (1962). A refinement of previous hypotheses concerning the local structure of turbulence in a viscous incompressible fluid at high reynolds number. *J. Fluid Mech.*, 13:82–85.

[70] Kreiss, H. and Oliger, J. (1972). Comparison of accurate methods for the integration of hyperbolic equations. *International Journal for Numerical Methods in Fluids*, 24:199–215.

[71] Krogstad, P.-Å. and Davidson, P. A. (2010). Is grid turbulence saffman turbulence? *J. Fluid Mech.*, 642:373–394.

[72] Krogstad, P.-A. and Davidson, P. A. (2012). Near-field investigation of turbulence produced by multi-scale grids. *Physics of Fluids*, 24:035103.

[73] Kurian, T. and Fransson, J. H. M. (2009). Grid-generated turbulence revisited. *Fluid Dynamics Research*, 41:021403.

[74] Laizet, S. and Lamballais, E. (2009). High-order compact schemes for incompressible flows: A simple and efficient method with quasi-spectral accuracy. *Journal of Computational Physics*, 228(16):5989–6015.

[75] Laizet, S. and Li, N. (2011). Incompact3d: A powerful tool to tackle turbulence problems with up to $O(10^5)$ computational cores. *International Journal for Numerical Methods in Fluids*, 67:1735–1757.

[76] Lander, D. C., Moore, D. M., Letchford, C. W., and Amitay, M. (2018). Scaling of square-prism shear layers. *J. Fluid Mech.*, 849:1096–1119.

[77] Lavoie, P., Djenidi, L., and Antonia, R. A. (2007). Effects of initial conditions in decaying turbulence generated by passive grids. *J. Fluid Mech.*, 585:395–420.

[78] Lele, S. K. (1992). Compact finite difference schemes with spectral-like resolution. *Journal of Computational Physics*, 103(1):16–42.

[79] Lumley, J. L. and Newman, G. R. (1977). The return to isotropy of homogeneous turbulence. *Journal of Fluid Mechanics*, 82(1):161–178.

[80] Mannini, C., Ante Šoda, A., and Schewe, G. (2010). Unsteady rans modelling of flow past a rectangular cylinder: Investigation of reynolds number effects. *Computers & Fluids*, 39:1609–1624.

[81] Mannini, C., Marra, A., Pigolotti, L., and Bartoli, G. (2018). The effects of free-stream turbulence and angle of attack on the aerodynamics of a cylinder with rectangular 5:1 cross section. *J. Wind Eng. Ind. Aerodyn.*, 161:42–58.

[82] Mariotti, A., Salvetti, M., Omrani, P., and Witteveen, J. (2016). Stochastic analysis of the impact of freestream conditions on the aerodynamics of a rectangular 5:1 cylinder. *Comp. Fluids*, 136:170–192.

[83] Mariotti, A., Siconolfi, L., and Salvetti, M. (2017). Stochastic sensitivity analysis of large-eddy simulation predictions of the flow around a 5:1 rectangular cylinder. *European Journal of Mechanics - B/Fluids*, 62:149–165.

[84] Matsumoto, M. (1996). Aerodynamic damping of prisms. *J. Wind Eng. Ind. Aerodyn.*, 59:159–175.

[85] Mazellier, N. and Vassilicos, J. C. (2010). Turbulence without richardson-kolmogorov cascade. *Physics of Fluids*, 22:075101.

[86] Mohamed, M. S. and Larue, J. C. (1990). The decay power law in grid-generated turbulence. *J. Fluid Mech.*, 219:195–214.

[87] Moin, P. and Kim, J. (1982). Numerical investigation of turbulent channel flow. *J. Fluid Mech.*, 118:341–37.

[88] Moin, P. and Mahesh, K. (1998). Direct numerical simulation: a tool in turbulence research. *Ann. Rev. Fluid Mech.*, 30:539–578.

[89] Monin, A. and Yaglom, A. (1975). *Statistical Fluid Mechanics*. MIT Press.

[90] Moore, D. and Amitay, M. (2021). Production and migration of turbulent kinetic energy in bluff body shear layers. *Int. J. Heat Fluid Flow*, 88:108716.

[91] Moore, D., Letchford, C., and Amitay, M. (2019). Energetic scales in a bluff body shear layer. *J. Fluid Mech.*, 875:543–575.

[92] Mora, D. O., Muñiz Pladellorens, E., Riera Turró, P., Lagauzere, M., and Obligado, M. (2019). Energy cascades in active-grid-generated turbulent flows. *Phys. Rev. Fluids*, 4:104601.

[93] Nadge, P. and Govardhan, R. (2014). High reynolds number flow over a backward-facing step: structure of the mean separation bubble. *Experiments in Fluids*, 55:1657.

[94] Nguyen, D., Hargreaves, D., and Owen, J. (2018). Vortex-induced vibration of a 5:1 rectangular cylinder: A comparison of wind tunnel sectional model tests and computational simulations. *J. Wind Eng. Ind. Aerodyn.*, 175:1–16.

[95] Norberg, C., editor (1998). *LDV-measurements in the near wake of a circular cylinder*. Advances in Understanding of Bluff Body Wakes and Vortex-Induced Vibration.

[96] Okajima, A. (1982). Strouhal numbers of rectangular cylinders. *J. Fluid Mech.*, 123:379–398.

[97] Ota, T., Asano, Y., and Okawa, J. (1981). Reattachment length and transition of the separated flow over blunt flat plates. *Bulletin of JSME*, 24:941–947.

[98] Patera, A. (1984). A spectral element method for fluid dynamics: Laminar flow in a channel expansion. *Journal of Computational Physics*, 54:468–488.

[99] Pearson, B., Krogstad, P.-Å., and Water, van de, W. (2002). Measurements of the turbulent energy dissipation rate. *Physics of Fluids*, 14(3):1288–1290.

[100] Perot, B. and Moin, P. (1995). Shear-free turbulent boundary layers. part 1. physical insights into near-wall turbulence. *J. Fluid Mech.*, 15:199–227.

[101] Piller, M., Boschetto, A., Stalio, E., Schena, G., and Errico, O. (2013). Pore-scale simulation of laminar flow through a sample of aluminum foam. *Journal of Porous Media*, 16:777–793.

[102] Pope, S. B. (2000). *Turbulent Flows*. Cambridge University Press.

[103] Prasad, A. and Williamson, C. H. K. (1997). The instability of the shear layer separating from a bluff body. *J. Fluid Mech.*, 333:375–402.

[104] Ricci, M., Patruno, L., de Miranda, S., and Ubertini, F. (2017). Flow field around a 5:1 rectangular cylinder using les: influence of inflow turbulence conditions, spanwise domain size and their interaction. *Comp. Fluids*, 149:181–193.

[105] Rocchio, B., Mariotti, A., and Salvetti, M. (2020). Flow around a 5:1 rectangular cylinder: Effects of upstream-edge rounding. *J. Wind Eng. Ind. Aerodyn.*, 404:104237.

[106] Roshko, A. (1961). Experiments on the flow past a circular cylinder at very high reynolds number. *J. Fluid Mech.*, 10:345–356.

[107] Rotta, J. (1951). Statistische theorie nichthomogener turbulenz. *Zeitschrift für Physik*, 129(6):547–572.

[108] Saffman, P. G. (1967). The large-scale structure of homogeneous turbulence. *J. Fluid Mech.*, 27:581–593.

[109] Schewe, G. (2013). Reynolds-number-effects in flow around a rectangular cylinder with aspect ratio 1:5. *Journal of Fluids and Structures*, 39:15–26.

[110] Seoud, R. E. and Vassilicos, J. C. (2007). Dissipation and decay of fractal-generated turbulence. *Physics of Fluids*, 19:105108.

[111] She, Z. and Leveque, E. (1994). Universal scaling laws in fully developed turbulence. *Phys. Rev. Lett.*, 72:336–339.

[112] Simmons, L. F. G. and Salter, C. (1934). Experimental investigation and analysis of the velocity variations in turbulent flow. *Proceedings of the Royal Society of London. Series A*, 145:212–234.

[113] Spalart, P. (2000). Strategies for turbulence modelling and simulations. *International Journal of Heat and Fluid Flow*, 21:252–263.

[114] Taylor, G. I. (1935). Statistical theory of turbulence. *Proceedings of the Royal Society of London. Series A, Mathematical and Physical Sciences*, 151:421–444.

[115] Tennekes, H. and Lumley, J. L. (1972). *A first course in turbulence*. MIT press.

[116] Townsend, A. (1956). *The Structure of Turbulent Shear Flow*. Cambridge University Press.

[117] Trias, F., Gorobets, A., and Oliva, A. (2015). Turbulent flow around a square cylinder at reynolds number 22,000: A dns study. *Computers & Fluids*, 123:87–98.

[118] Valente, P. C. and Vassilicos, J. C. (2011). The decay of turbulence generated by a class of multiscale grids. *J. Fluid Mech.*, 687:300–340.

[119] Valente, P. C. and Vassilicos, J. C. (2012). Universal dissipation scaling for nonequilibrium turbulence. *Phys. Rev. Lett.*, 108:214503.

[120] Valente, P. C. and Vassilicos, J. C. (2014). The non-equilibrium region of grid-generated decaying turbulence. *J. Fluid Mech.*, 744:5–37.

[121] Vichnevetsky, R. and Bowles, J. (1982). *Fourier analysis of numerical approximations of hyperbolic equations*. SIAM.

[122] von Kármán, T. and Howarth, L. (1938). On the statistical theory of isotropic turbulence. *Proceedings of the Royal Society of London. Series A, Mathematical and Physical Sciences*, 164:192–215.

[123] Wang, H. and George, W. (2002). The integral scale in homogeneous isotropic turbulence. *J. Fluid Mech.*, 459:429–443.

[124] Wang, Z., Fidkowski, K., Abgrall, R., Bassi, F., Caraeni, D., Cary, A., Deconinck, H., Hartmann, R., Hillewaert, K., Huynh, H., Kroll, N., May, G., Persson, P., van Leer, B., and Visbal, M. (2013). High-order cfd methods: current status and perspective. *International Journal for Numerical Methods in Fluids*, 72:811–845.

[125] Weller, H., Tabor, G., Jasak, H., and Fureby, C. (1998). A tensorial approach to computational continuum mechanics using object-oriented techniques. *Computers in physics*, 12:620–631.

[126] Wu, B., Li, S., Li, K., and Zhang, L. (2020). Numerical and experimental studies on the aerodynamics of a 5:1 rectangular cylinder at angles of attack. *J. Wind Eng. Ind. Aerodyn.*, 199:104097.

[127] Yang, Z. (2012). Numerical study of transition process in a separated boundary layer on a flat plate with two different leading edges. *WSEAS Transactions on Applied and Theoretical Mechanics*, 7:49–58.

[128] Zhang, Z. and Xu, F. (2020). Spanwise length and mesh resolution effects on simulated flow around a 5:1 rectangular cylinder. *J. Wind Eng. Ind. Aerodyn.*, 202:104186.

[129] Zhou, T. and Antonia, R. A. (2000). Reynolds number dependence of the small-scale structure of grid turbulence. *J. Fluid Mech.*, 406:81–107.

Appendix A

A glance at the effect of porosity

The aim of this appendix is to verify the extent to which turbulent flow statistics in the lee of an open-cell metal foam layer are affected by porosity. The results obtained for a foam of porosity $\varepsilon = 0.97$ are compared against the $\varepsilon = 0.92$ case, as investigated in the chapter 3 of the present work. The two foams have equal pore size but different ligament thickness, i.e. the foam with larger porosity is characterised by a thinner ligament, $d'_f < d_f$. The comparison is conducted by means of DNS performed with the same numerical parameters as outlined in § 2.2 except for the computational grid, which consists of $n_x = 2049$ and $n_y = n_z = 512$ grid nodes.

The porous matrix of higher porosity generates a turbulent field where fluctuations are less intense in all the spatial directions. Application of the fitting procedure outlined in section § 2.3.4 on the high-porosity foam provides decay exponents for u^2_{rms} and $\langle k \rangle$ of $n'_u = 1.05$ and $n'_k = 1.08$, respectively. The results obtained on the coarse grid for the $\varepsilon = 0.92$ case yield $n_u = 1.12$ and $n_k = 1.13$; see table 2.2 for comparisons against results on the fine mesh. The power-law decay of the turbulent kinetic energy begins more upstream than in the $\varepsilon = 0.92$ case; see figure A.1.

Inside the developed region, the Kolmogorov and the longitudinal integral length scales evaluated for $\varepsilon = 0.97$ behave according to power laws with growing rates estimated by the exponents $s' = 0.54$ and $q' = 0.47$, respectively (see table 2.3 for notation). The lower-porosity case exhibits decay exponents along the x-direction of $s = 0.56$ and $q = 0.51$ (see table 2.3 for comparisons against results on the fine mesh) but the Kolmogorov and the integral scales are different in magnitude, as displayed by figure A.2(a) and (b). Associated with the smaller kinetic energy content of the flow and a smaller dissipation rate observed at $\varepsilon = 0.97$, the turbulence induced by the higher-porosity foam is characterised by a larger Kolmogorov scale and a smaller integral scale.

Figure A.3 displays the effects of porosity on the terms of the turbulent kinetic energy budget. The transport mechanisms of $\langle k \rangle$ for $\varepsilon = 0.97$ are the same as described in section § 2.3.11 for $\varepsilon = 0.92$ but are characterised by an upstream shift of the transport peaks with

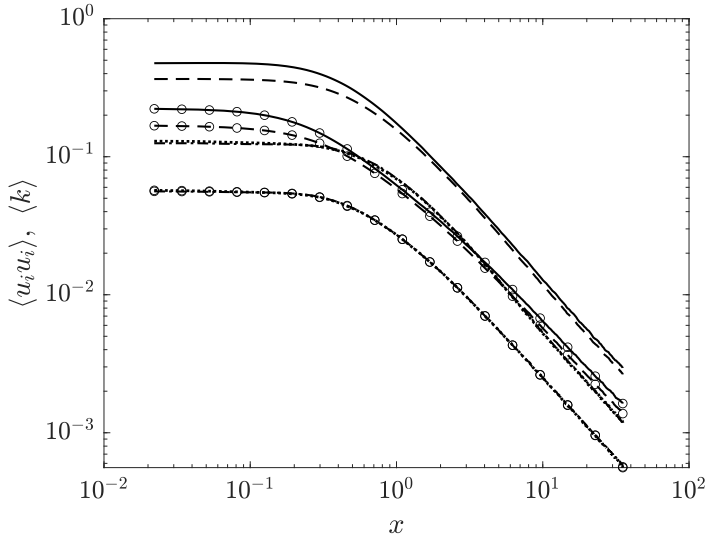

Figure A.1. Streamwise evolution of velocity fluctuations and turbulent kinetic energy for the $\varepsilon = 0.97$ and $\varepsilon = 0.92$ cases on the coarse computational grid: ——, $\langle uu \rangle$; — · —, $\langle vv \rangle$; · · · · · ·, $\langle ww \rangle$; and - - - -, $\langle k \rangle$. The lines with circles ◯ mark the case with higher porosity $\varepsilon = 0.97$.

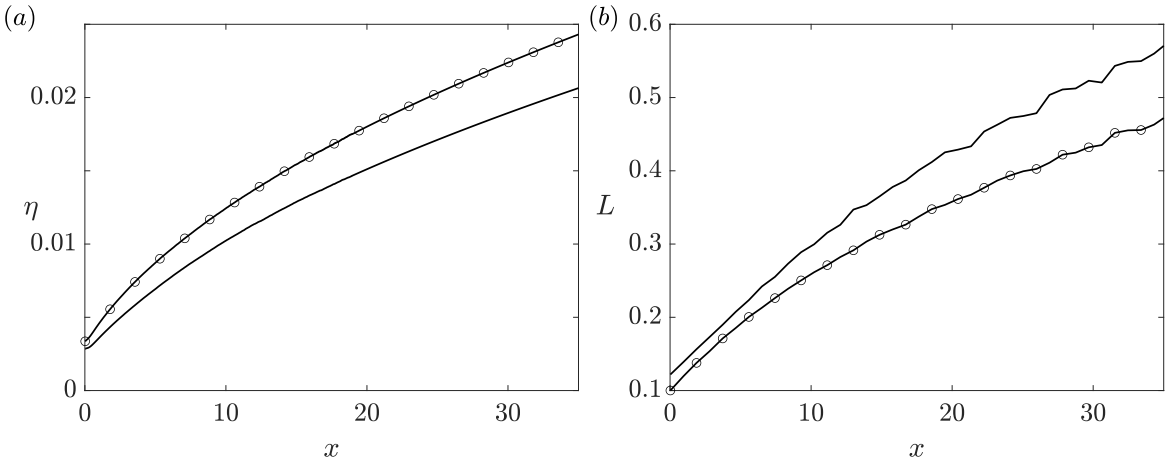

Figure A.2. Comparison between the streamwise distributions of the Kolmogorov scale (a) and the longitudinal integral scale (b) for the $\varepsilon = 0.97$ and $\varepsilon = 0.92$ cases on the coarse computational grid: ——, length scales for $\varepsilon = 0.92$; and —○—, length scales for $\varepsilon = 0.97$.

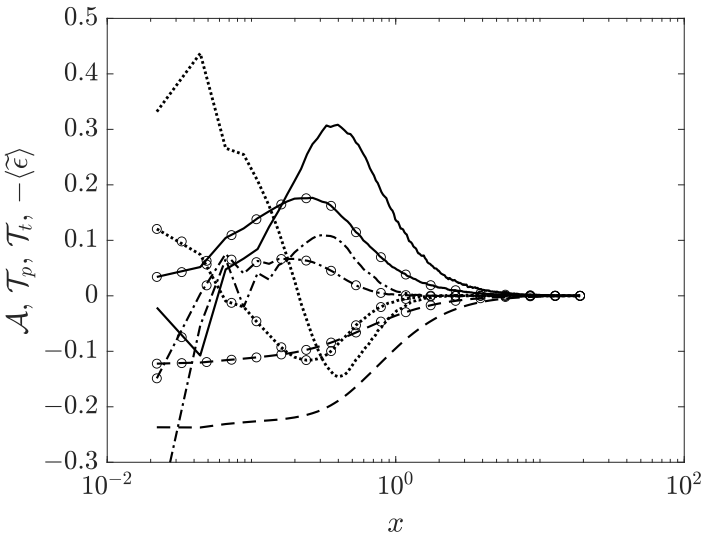

Figure A.3. Comparison between the turbulent kinetic energy budget terms for the $\varepsilon = 0.97$ and $\varepsilon = 0.92$ cases on the coarse computational grid: ——, $\mathcal{A}$; — · —, $\mathcal{T}_p$; · · · · · ·, $\mathcal{T}_t$; and - - - -, $-\langle\widetilde{\epsilon}\rangle$. The lines with circles ◯ mark the case with higher porosity $\varepsilon = 0.97$.

respect to that case. This shift is consistent with the reduction of the vortex formation length associated with a smaller ligament thickness, as indicated by [95] and reported in § 2.3.11.

In summary, while the results obtained for $\varepsilon = 0.92$ show small quantitative differences with respect to $\varepsilon = 0.97$, no significant discrepancies are observed between the two cases. An upstream shift in the peaks of $\langle k\rangle$ transports characterises the higher-porosity case, which in turn implies a reduced vortex formation length and the achievement of power-law decays at shorter distances from the porous matrix. The size of such displacement is apparently very small.